Ablation loading and qudit measurements with barium ions

by

Brendan Bramman

A thesis
presented to the University of Waterloo
in fulfillment of the
thesis requirement for the degree of
Doctor of Philosophy
in
Physics (Quantum Information)

Waterloo, Ontario, Canada, 2023

Examining Committee Membership

The following served on the Examining Committee for this thesis. The decision of the Examining Committee is by majority vote.

External Examiner: Eric Hudson
Professor, Dept. of Physics and Astronomy,
University of California, LA

Supervisor(s): Crystal Senko
Assistant Professor, Dept. of Physics and Astronomy,
University of Waterloo

Internal Member: Kevin Resch
Professor, Dept. of Physics and Astronomy,
University of Waterloo

Internal-External Member: Michal Bajcsy
Associate Professor, Dept. of Electrical and Computer Engineering,
University of Waterloo

Other Member(s): Christine Muschik
Associate Professor, Dept. of Physics and Astronomy,
University of Waterloo

Author's Declaration

This thesis consists of material all of which I authored or co-authored: see Statement of Contributions included in the thesis. This is a true copy of the thesis, including any required final revisions, as accepted by my examiners.

I understand that my thesis may be made electronically available to the public.

Statement of Contributions

I, Brendan Bramman, am the sole author of all chapters. Pei Jiang Low helped contribute to many of the results of Chapter 4. Pei Jiang Low and Yvette De Sereville contributed to data collection for Chapter 3. Nicholas Zutt and Jonathon Qualter contributed to data collection for Chapter 5.

Abstract

Barium is one of the best ions for performing quantum information in a trapped-ion system. Its long-lived metastable $D_{5/2}$ state allows for some interesting quantum operations, including the current best state preparation and measurement fidelity in qubits. This metastable state also opens up the possibility of implementing higher-dimensional qudits instead of qubits. However, installing a barium metal source in a vacuum chamber has shown to be somewhat of a challenge. Here, we present a loading technique which uses a barium chloride source instead, making it much easier to install. Laser ablation with a high-energy pulsed laser is used to generate neutral atoms, and a two-step photoionization technique is used to selectively load different isotopes of barium in our ion trap. The process of laser ablation and the plume of atoms it generates are characterized, informing us on how to best load ions. Loading is achieved, and selectivity of our method is demonstrated, giving us a reliable way to load $^{138}\mathrm{Ba}^{+}$ and $^{137}\mathrm{Ba}^{+}$ ions. The quadrupole transition into the metastable $D_{5/2}$ state is investigated, with all of the individual transitions successfully found and characterized for $^{138}\mathrm{Ba}^{+}$ and $^{137}\mathrm{Ba}^{+}$. Coherent operations are performed on these transitions, allowing us to use them to define a 13-level qudit, on which we perform a state preparation and measurement experiment. The main error source in operations using this transition is identified to be magnetic field noise, and so we present attempts at mitigating this noise. An ac-line noise compensation method is used, which marginally improved the coherence time of the quadrupole transitions, and an additional method of using permanent magnets is proposed for future work. These efforts will help to make trapping barium more reliable, making it an even more attractive option for trapped ion systems. The state preparation and measurement results using the quadrupole transition to the long-lived metastable $D_{5/2}$ state establish barium as an interesting platform for performing high-dimensional qudit quantum computing.

Acknowledgements

I first would like to thank my advisor Crystal Senko for her sound guidance and all that she taught me, and for allowing me space to pick myself back up. Thank you to all of my colleagues in my group, especially Pei Jiang Low and Rich Rademacher, who started this with me and helped me learn to be a physicist. I am very fortunate to have gotten the oppportunity to work under Matt Day, who was a postdoc in our group for much of my time here and was instrumental in helping us to march forward. Yvette De Serrevile was only here for a short time, and Nicholas Zutt only just started, but I greatly valued our time together working tirelessly in the dark lab running experiments. Thank you to all of my colleagues in Rajibul Islam's trapped ions group, for letting me borrow that wrench. I will return it soon, I swear!

I would also like to thank my roommates for my first few years here, Andy Ding and Noah Greenberg, let's have another movie night soon! Thank you so much to my best friend Michael Busch for giving me the encouragement I needed both when I did and didn't need it. Thank you to my dear friend Yamin Zhou for your support. Finally, thank you to my parents and brothers, for always being those lighthouses far away, but always watching and believing in me.

Dedication

This is dedicated to my cat, Bruce, who got me through.

Table of Contents

List of Figures

List of Tables

List of Abbreviations

AC alternating current 8, 102, 104–115, 118, 119

AOM acousto-optic modulator 20, 24, 26, 27, 29, 67

AWG arbitrary waveform generator 29, 30, 67, 76, 77, 98, 118

CCD charge coupled device 20, 28, 55

DC direct current 11, 23, 114

ECDL external-cavity diode laser 23–27, 64, 66, 76

EOM electro-optic modulator 14, 24, 25, 28, 29, 55, 64–67, 75–79, 81, 84

FNCS fiber noise canceling system 64, 67

HeNe Helium-Neon 26, 57

HF hyperfine 5, 6, 12, 15–17, 21, 22, 28, 43, 44, 55, 68, 70–73, 86, 97, 103

HWP half-wave plate 23, 24, 26, 37, 67

LP low-pass 64, 67

MB Maxwell-Boltzmann 53, 126

MS Mølmer-Sørensen 22

NA numerical aperture 27

PBS polarizing beam-splitter 24, 37, 66, 67

PDH Pound-Drever-Hall 25, 64–67, 75, 76, 78

PID proportional, integral, derivative 26, 27

PLL phase lock loop 29

PMT photo-multiplier tube 12, 28, 30, 45, 46, 55, 56, 76, 126–128

QWP quarter-wave plate 24, 25, 66

REMPI resonance enhanced multi-photon photo-ionization 7, 8, 31, 32, 40, 42, 46, 51, 52, 54, 55, 58, 59, 117

RF radiofrequency 10, 11, 23, 24, 26, 27, 29, 30, 40, 45, 61, 65–67, 75, 77, 79, 81, 110, 116, 124

SN signal-to-noise 28, 45

SPAM State preparation and measurement 3, 5, 7, 8, 18, 62, 63, 96–101, 103, 104, 117, 118

TOF time-of-flight 31, 49, 51–53, 116, 126

TTL transistor-transistor logic 23, 29, 30, 36

Chapter 1

Introduction

Trapped ions have proven to be extremely useful for a broad range of fields in physics, chemistry, and quantum information [1–3]. They are a crucial tool, allowing for very precise control of quantum states, simulation of quantum systems and precise measurements of atomic properties. Researchers used ion traps early on to do mass spectroscopy experiments, and today ion traps are highly valuable tools in mass spectroscopy [1] because of their sensitivity and control. Ion traps have also always been used for metrology, especially as an atomic clock [4], with some of the best frequency standards coming from ions [5]. Quantum information using trapped ions came a bit later, but it has since become one of the primary fields using trapped ions. As a quantum information platform, trapped ions have some of the best fidelities in single qubit operations [6], entangling operations [7], and measurements [8]. Their gate-time to coherence time ratio is unmatched by any other quantum information platform [2].

Ions are quite simple, made up of a single atom with either extra or missing electrons. The charged nature of an ion makes it quite easy to push and pull, and to confine. Every ion of its kind is exactly the same in terms of frequencies, transition strengths, couplings with other atoms, etc. It's very easy to generate a large number of trappable ions by just heating up or vaporizing a sample. All of these advantages make ions quite easy to trap and to work with.

Typically, ions are picked from the alkaline earth metals column of the periodic table (Figure 1.1). These ions will have a closed shell and a single valence electron, and this electron is the primary thing we focus on within the trapped ion. This electron can be excited to different energy levels using lasers of different frequency. These energy levels can be used for doing all kinds of interesting things, such as fluorescing and imaging the ion, measuring extremely precise frequencies, performing quantum oscillations, and creating entanglement. In quantum information, we use this electron as our quantum information carrier. If we trap multiple ions in a single trap, they all share motional modes and we can use electron transitions to entangle ions through these motional modes.

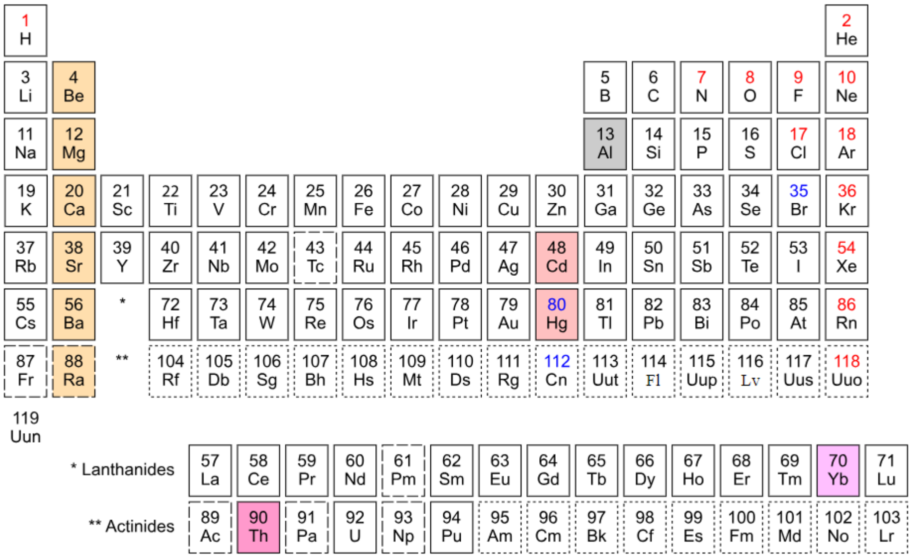

Figure 1.1: The periodic table: the most commonly used ions are shaded. Yellow-shaded elements are the alkaline metals, which have very simple electronic energy structures.

Trapped ions are especially interesting for applications in quantum information, which utilizes their quantum properties to perform algorithms which could in principle be faster than possible on any classical computer. The first of these quantum properties is superposition, an effect where the state of a qubit can be found in either the $|0\rangle$ or the $|1\rangle$ state with some probability. This strange probabilistic nature of qubits allows one to essentially try many possible configurations of the qubits at once. When you measure a qubit, however, it is forced to collapse into one of the states. So to take advantage of superposition, algorithms are designed such that the correct answers constructively interfere and wrong answers destructively interfere. Experiments must also be performed many times to build statistics and infer the actual quantum states.

The other quantum property which quantum computers take advantage of is quantum entanglement. Two particles are entangled if their quantum states are correlated with one another such that their individual quantum states cannot possibly be described independently. It is kind of like a superposition between separate qubits. An entangled quantum state of two qubits a and b might look like the maximally entangled bell states:

$$|\Psi^{\pm}\rangle = \left(|0\rangle_a|0\rangle_b \pm |1\rangle_a|1\rangle_b\right)/\sqrt{2}, \tag{1.1}$$

or

$$|\Phi^{\pm}\rangle = \left(|0\rangle_a|1\rangle_b \pm |1\rangle_a|0\rangle_b\right)/\sqrt{2}. \tag{1.2}$$

These states cannot be factored out into terms containing only one of the qubits. If you were to measure one the qubits, the other would necessarily immediately collapse into the same (for $|\Psi^{\pm}\rangle$) or opposite (for $|\Phi^{\pm}\rangle$) state, even if they were physically separated by a long distance. Entanglement is crucial for building controlled-not gates and quantum Fourier transform operations [9] in quantum computation, and is also a useful feature for ancilla qubit readout in quantum error correction schemes [10, 11].

Trapped ions have thus far been extremely successful at utilizing these quantum properties of the electron to create quantum gates for quantum computation. In terms of fidelities, single qubit gate operations in ions can be performed with on the order of 1×10^{-6} error [6], and entangling operations can have on the order of 1×10^{-3} error [7,12]. Using the common ion trap motional mode for entanglement makes it a fully connected system, which in principle, allows any pair of ions in a chain able to be entangled. With more complicated trap electrode setups, you can also shuttle ions around and do a myriad of useful operations to help improve and scale up quantum computation [13]. State preparation and measurement (SPAM) in trapped ions is equally impressive, with the record recently being set at under 1×10^{-4} error [8]. Not only are the operations quite high fidelity, the coherence times can be quite long compared to the operation times, allowing for many quantum operations to be performed in a single quantum computation even without error correction [2]. All of these impressive results make trapped ions one of the leading contenders as a platform for quantum computing.

While trapped ions have a lot of very attractive features, one of the outstanding challenges today is scaling to higher numbers of ions to perform useful algorithms and implement fault-tolerant error correction. In order for any quantum computer to be useful for solving problems better than a regular computer, many thousands of qubits are needed. In addition, to avoid debilitating errors building up during the computation, each of these qubits needs many additional qubits for performing fault-tolerant error correction. These quantum operations need to be performed on thousands and thousands of individual ions and some of these ions need to be individually read out during the computation [2]. Currently, individual ion traps are limited to on the order of 100 ions, with a limit of around 50 of them for individual control and addressing. In order to solve this scaling problem in trapped ions, there are many approaches being explored. These include using ion traps with many different zones, allowing for shuttling ions and chains around, and building networks of ion traps and using photon entanglement to allow them to communicate. Another less explored option is to utilize more of the computational space already available within the trapped ions, making what's called a qudit, a d-dimensional quantum information carrier. As the qudit dimension is increased, the computational space dramatically increases; with n qudits of dimension d, the computational space increases as d^n.

Beyond the scaling argument for using qudits, there are also some algorithmic advantages that come with using qudits instead of qubits. Some algorithms, such as the Toffoli gate, can be done using half [14] the number of two-qutrit gates compared to the traditional method using two-qubit gates, and generalized N-controlled Toffoli gates can be implemented with a 70× reduction [15] in qutrit gates compared to the number of qubit gates. This improved efficiency has been shown to occur in many other kinds of quantum gates and algorithms as well [16]. Quantum phase estimation can also be performed using roughly half the number of qudits than qubits for some examples [17]. Algorithms which aim to simulate higher-dimensional quantum systems intuitively can be much better by using qudits [18, 19].

Qudits also seem to be advantageous in terms of quantum error correction. The simplest way is through simpler gate implementations such as the Toffoli gate mentioned previously [16]; this gate is very frequently featured as a part of error correcting protocols. Many studies have indicated that error correction thresholds become more favorable for higher dimensional qudit computation [20–23]. Magic-state distillation, a crucial but often difficult procedure used in many error correction protocols, can also be improved by using higher dimensions [21, 24]. Therefore, fault-tolerant quantum computing for qudits may be able to sustain a higher error rate than for qubits.

The most used ions all have a similar energy structure for the valence electron as shown in Figure 1.2, with a ground state S and some P and D states at higher energies. The electron prefers to be in the lowest ground S state, which effectively has an infinite lifetime, while the higher energy states are much shorter-lived. The P states have lifetimes on the order of nanoseconds and the D states have lifetimes on the order of milliseconds to seconds. The electron can be driven from the ground to P states via dipole transition using lasers, from which it very quickly decays into lower energy states. To prevent the electron getting stuck in the longer lived D states, repump lasers are used to drive back to the P states. Fluorescence of the dipole transitions can be measured by imaging systems to actually see and measure the ions. A qubit is most commonly defined within two of the ground state levels. The qubit state can be prepared by driving dipole transitions in such a way that the electron eventually ends up in a known prepared state. The state of a qubit can be discerned by driving fluorescence transitions only resonant with one of the qubit states.

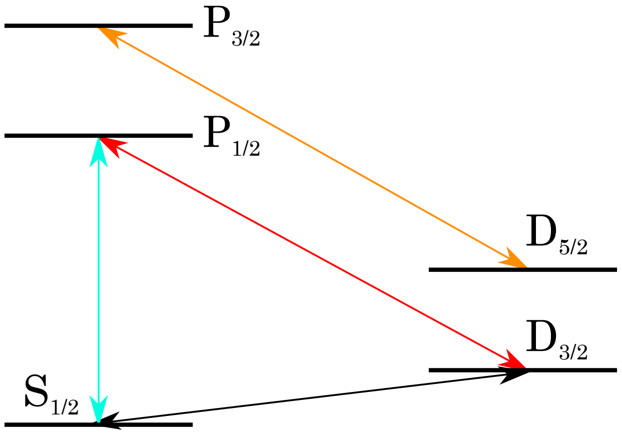

Figure 1.2: Typical energy structure of a trapped ion. The P states have on the order of nanosecond lifetimes and the D states have on the order of second lifetimes.

Single qubit operations are performed using either microwaves directly between the qubit states, or Raman two-photon transitions via the intermediate P states. Entanglement can be done by driving several Raman transitions with detunings such that motional modes of the ion chain are at least partially excited.

One of the most commonly used ions is the alkaline metal barium [8, 25–30]. Barium is quite useful for several reasons. Many of its electronic transitions have frequencies in the visible range, making it relatively easier to align and find optical components such as fibers. Even the Raman laser used for barium is well in the visible range at 532 nm. The $D_{5/2}$ energy level in barium is especially useful, with its very long lifetime [31] of 35 s. This particularly long lifetime of the $D_{5/2}$ state in barium is one strong reason for why we choose to use it as a qudit.

When defining a qubit in a trapped ion, we are often ignoring and trying to avoid the abundance of other states also present. In hyperfine (HF) qudits, there are often four or more states within the ground state alone, and ten or more states in the long-lived D states ($D_{3/2}$ states are not used because of the need to flush it during SPAM). These additional states can be used to increase the computational space of a single ion as a qudit. Single qudit gates can be straightforwardly generalized using pulses between individual sets of qudit levels. Any d-dimensional single qudit unitary can be generated by sequences of such pulses, as shown in Reference [32]. Entangling gates can also be generalized from the qubit versions [33, 34]. Because of the additional states being utilized, one must be a little more careful with how measurements are performed on qudits. As different qudit states are measured, the $D_{5/2}$ metastable level can be used to store the remaining qudit states,

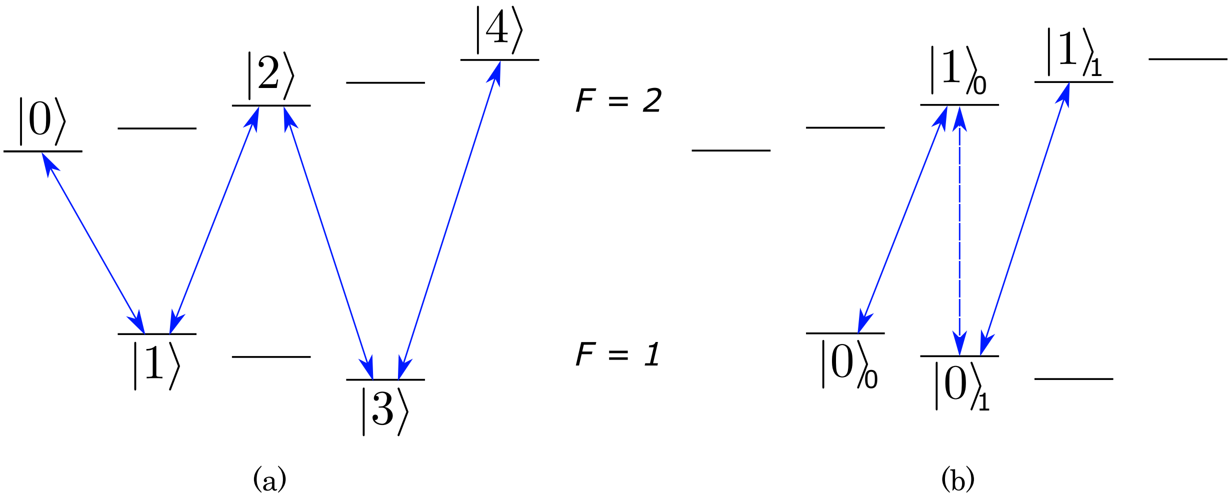

Figure 1.3: Some examples of qudits. Different levels within each F state are Zeeman levels m_F, which have different energies depending on the applied magnetic field. (a) A 5-level qudit encoding in an $I = 3/2$ (nuclear spin) electronic ground state. (b) A 4-level qudit encoding in an $I = 3/2$ electronic ground state, used to make two qubits from a single information carrier, a ququart.

allowing for discrimination between all of them and giving the ability to perform a full measurement.

One could use the HF states as the computational states of a qudit in many different ways, with some examples shown in Figure 1.3. There are lots of states to choose from, with a total of eight states within the ground manifold. In addition, one could imagine using a single ion to define two qubits, called a ququart [35] (Figure 1.3(b)). Finally, the metastable states in the $D_{5/2}$ level can be used to further increase the dimensionality of a qudit [33–38]. In this work, we use the isotope $^{137}\mathrm{Ba}^{+}$ to demonstrate this. We choose this isotope because it has a nuclear spin of 3/2, giving us an abundance of energy states to work with: a total of 32 energy states in the $S_{1/2}$ and the $D_{5/2}$ levels.

1.1 Thesis outline

The overall structure of the thesis is as follows. Chapter 2 gives some background on trapped ions and quantum computation. After giving a background of everything, I present our results, with Chapter 3 showing our successful ion loading using laser ablation and photoionization. Next, the results of our 13-level qudit measurement are given in Chapter 4. Finally, some initial results on magnetic field compensation are presented in Chapter 5 before a brief conclusion in Chapter 6.

This thesis begins in Chapter 2 by going into a lot of the background behind this work. This includes how trapped ion systems (specifically Paul traps) are able to trap individual ions so that they can be used as a qubit. Next, I discuss barium ions, the chosen ion for our lab, and why they are a good choice to work with. I give some details on how this ion can be addressed in a trapped ion system.

With the qubit platform of barium ions chosen, I then discuss how we can use it for quantum computation. First, a discussion on how we use trapped ions for performing quantum computation operations is presented. All of the steps necessary for doing full quantum computation with ions are laid out here, including how we define the qubit, coherence, SPAM, and single- and two-qubit gates. Our lab is interested in extending the idea of a qubit further by using qudits instead. I discuss how we can do all of the necessary quantum computation operations with qudits in trapped ions. The work developing these operations [33] was one of our lab's first publications in 2020, and was a joint co-authorship between myself and Pei Jiang Low. In Section 2.2, I start going into the specifics of our trap apparatus. First I give details about our ion trap and the optics/lasers used in our lab. Specifics on which devices and control systems we use, optics paths, and details on which transitions we drive are presented here. A lot more details about how this all was brought up can be found in my master's thesis [39] from 2019.

In Chapter 3, I give details on the project of loading ions in our apparatus. First, I give a general background of the different ways in which ion traps are typically loaded. The different options for producing atoms are presented and advantages and disadvantages are weighed. Next, our specific ablation loading technique using a 532 nm pulsed laser and a $BaCl_2$ target is discussed. Details about what kind of target we use, which laser we use to ablate, and how we brought up this laser are given. Finally, I talk about the different ways of turning the things we ablate into trappable ions. General methods are mentioned, but we quickly move into the details of the method we use: resonance enhanced multi-photon photo-ionization (REMPI) with 554 nm and 405 nm lasers.

Section 3.2 presents the details of how we do ablation, and the results from characterizing the ablation, loading rates, and our selectivity results. First, the ablation itself is characterized, the process of getting a new spot to work is given, and the plume generated from ablation is characterized. Following that, I show that the method works for loading ions and present loading rates. In the final part of this chapter, I discuss how well we were able to selectively load different isotopes of barium using our REMPI ionization method. I was the first author in the publication of these results in 2022 [40].

Chapter 4 presents on the qudit measurement results we achieved with up to a 13-level qudit. First, the general information on the main transition featured (using the 1762 nm laser) is given, with the laser system, laser paths, and optics discussed in detail. Quadrupole transition information is given, with specifics to our 1762 nm transition presented, including the expected transition strengths and electronic energy structure. With the requisite background and theoretical information given, Section 4.2 shows how we were able to find all of the many transition frequencies in $^{138}\mathrm{Ba}^{+}$ and $^{137}\mathrm{Ba}^{+}$. Coherent operations are shown, including Rabi oscillations and Ramsey sequences, and methods for calibrating the transition frequencies and π-times. In the final part of the chapter, Section 4.3 presents our SPAM results, with 3- and 6-level qudit measurements in $^{138}\mathrm{Ba}^{+}$ and a 13-level qudit measurement in $^{137}\mathrm{Ba}^{+}$. These results were released as a working paper in 2023, with Pei Jiang Low as first author and myself as the second author [37].

The penultimate Chapter 5 gives our initial results towards mitigating magnetic field noise, which we believe to be the largest error source reducing the fidelities of our shelving operations. First, a background is given and I discuss why we believe magnetic field noise is our largest error source. For the remainder of the chapter, two methods to mitigate this noise are presented: alternating current (AC)-line noise compensation and permanent magnets. For AC-line noise compensation in Section 5.2, I present initial experimental results indicating that this particular type of magnetic field noise might not be the main contributing noise source. In the final section of this chapter (5.3), I show the permanent magnets we plan to install on our trap next to mitigate other magnetic field noise contributions.

The last chapter (Chapter 6) concludes my thesis by summarizing the overall results presented and giving an outlook for future experiments and improvements.

Chapter 2

Background and Apparatus

In this chapter, the background of trapping ions and performing quantum computation on them as qubits or qudits is presented, and details about our experiment are given. First, I describe how individual ions can be trapped using electromagnetic fields, and how we can address them using lasers to make them useful for quantum computation. I justify our use of the specific ion barium and show how we can trap and address it. A background on quantum computation in qubits is given. Certain criteria must be met for trapped ions to be used as a qubit, and I present how these are satisfied. I discuss how we can extend these ideas to do qudit quantum computation in trapped ions. A detailed description of our apparatus is given, including information on the ion trap we built, and all of the laser systems and optics we use to address trapped barium ions. Further details on the building of the ion trap and optics setups can be found in mine and Pei Jiang Low's master's theses [39, 41].

2.1 Trapped ions, quantum computing, and qudits - background

2.1.1 Trapped ions

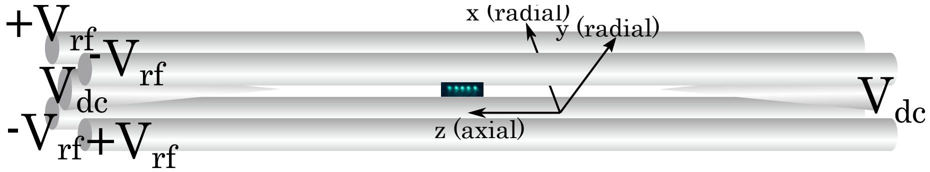

Figure 2.1: Commonly used ion trap design, the four-rod Paul trap, the type we use in our experiment. The two sets of diagonal rods have radiofrequency (RF) voltage exactly out of phase with each other for radial confinement in the x and y directions. The two needles have a static voltage for confinement axially in the z direction.

Because ions are charged, trapping them is just a matter of using electromagnetic fields in a way that we create a confining potential for the ion to be trapped in. The potential at the trap center is

$$\Phi = \frac{\Phi_0}{r_0^2}\left(\alpha_x x^2 + \alpha_y y^2 + \alpha_z z^2\right), \tag{2.1}$$

where Φ_0 is some amplitude for the potential, r_0 is the minimum distance from the trap center to the electrodes, and α_i are the coefficients of potential strength in each direction $i \in \{x, y, z\}$. Because of Laplace's equation, $\nabla\Phi = 0$, we have

$$\alpha_x + \alpha_y + \alpha_z = 0, \tag{2.2}$$

therefore only two of these directions can have confining potentials and one of them must have an anti-confining potential. In a Paul trap [42–44], this limitation is overcome by using a time-dependent RF ω_{rf} on four metal rods (see Figure 2.1),

$$\Phi_0(t) = V\cos(\omega_{rf}), \tag{2.3}$$

with voltage amplitude V. The RF voltage used is around 100 V to 600 V peak-to-peak, and for each set of opposing rods, the RF is exactly out of phase with the RF on the other pair. The RF is on the order of 20 MHz and if you average over time the effective potential looks like a quadratic potential. In this configuration the oscillating electromagnetic field in the radial direction is periodically switching between confining and anti-confining along the axis between and along the rods, which we call the RF null. This direction is defined to be the z direction, while x and y are the radial directions. To add confinement in the axial direction, needles on either side with static voltages on the order of 1 V to 200 V are used. Because charge can build up on surfaces surrounding the trap, there can be an overall static electric field which can push the ion away from the RF null, where the potential is minimum. This can cause undesirable additional motion of the ion called micromotion, which can make it harder to perform many quantum operations with the trapped ions. To move the ion back to the RF null, direct current (DC) voltage offsets are applied to the rods to cancel out the stray electric field.

An ion at this trap center moves around within the effective quadrupolar potential in a predictable way. It oscillates at a frequency called the secular frequency,

$$\omega_i = \frac{\omega_{rf}}{2}\sqrt{a_i + \frac{q_i^2}{2}}, \tag{2.4}$$

which depends on trap geometric factors a_i and q_i in the respective direction $i \in \{x, y\}$. If you trap multiple ions in the same trap, their charges will cause them to push against each other. Depending on how many you trap and the voltages being applied, they can line up in a linear chain with their positions not changing in the axial direction. Typically, around ten ions can be trapped in a linear chain before they start to squeeze each other off the RF null. These potentials have overall motional modes at certain frequencies in the radial and axial directions. These motional modes can be used as a bus to entangle the ions within the chain.

To generate the ions to be trapped, there are several different methods including Joule heating using an oven, or ablation using a high-power pulsed laser. These methods can be used to generate ions directly or to create a plume of neutral atoms; an ionization method can then be applied to generate the ions to be trapped. A major part of this work (Chapter 3), was to develop and characterize this method in our system, resulting in a reliable way for us to trap barium ions. The ions generated by these techniques are usually quite hot; when initially trapped, they are unable to crystallize until they have been cooled down sufficiently. One of the simplest and most commonly used methods for doing this is Doppler cooling with a laser driving one of the ion's dipole transitions. An ion moving through a laser beam will see the frequency of the laser Doppler shifted by an amount dependent on the speed v of the ion and the angle θ between the ion velocity and the laser,

$$f_{ob} = f_s\left(1 + \frac{v\sin\theta}{c}\right). \tag{2.5}$$

If the ion is moving towards the laser, the frequency will be blue-shifted to a higher frequency. The laser frequency is set to be red of the transition so that the ion is more likely to absorb a photon while moving towards the laser; when it does absorb a photon, it experiences a small momentum kick which slows it down some. The electron will then relax from the excited state, spontaneously emitting a photon in a random direction and again causing the ion to feel a small momentum kick in the opposite direction of the emitted photon. Because absorption preferentially slows the ion down and emitting a photon is random, the net result is a reduction in the speed and temperature of the ion. This method can be used to cool a trapped ion down to the Doppler limit on the order of milli-kelvin [45],

$$T_{Doppler} = \frac{\hbar\gamma}{2k_B}, \tag{2.6}$$

where $\hbar \approx 1 \times 10^{-34}\,\mathrm{J\,s}$ is the reduced Planck constant, $k_B \approx 1 \times 10^{-23}\,\mathrm{m^2\,kg\,s^{-2}\,K^{-2}}$ is the Boltzmann constant, and γ is the linewidth of the dipole transition (usually on the order of 100 MHz). This limit comes from the random momentum kicks caused by spontaneous emission. In terms of the motional modes, an ion cooled to the Doppler limit has a phonon level on the order of $n = 10$.

2.1.2 Barium ions

Barium is an alkaline metal with atomic number $Z = 56$ and a total weight of around 140 amu, putting it at middling weight compared to other typically used elements in ion traps. As a neutral atom, it has a completely closed off inner electron shell, with two valence electrons in the outer shell. If it sheds one of these valence electrons, it becomes an ion with a single valence electron, simplifying the atomic physics and control significantly. When ionized, it has a typical energy structure which is shown in Figures 2.2 and 2.3 for the two relevant isotopes used in this work, $^{138}\mathrm{Ba}^+$ and $^{137}\mathrm{Ba}^+$. $^{138}\mathrm{Ba}$ is the most abundant isotope of barium at around 72% of natural barium, while $^{137}\mathrm{Ba}$ is the next most abundant isotope at 11% (see Table 2.1). $^{138}\mathrm{Ba}^+$ has no nuclear spin, so the electronic structure is quite simple and it is easier to trap and fluoresce. $^{137}\mathrm{Ba}^+$ on the other hand has a nuclear spin of $I = 3/2$, so it has a particularly rich electronic energy structure with the ground state $F = 1$ and $F = 2$ states splitting into 3 and 5 separate levels with an applied magnetic field. The $D_{5/2}$ level which we feature in this work is even more rich, with the four HF levels splitting into 24 separate levels in a magnetic field; although the $F' = 3$ and $F' = 4$ levels have very close energies so much care is needed when using them.

A 493 nm laser is used to drive the dipole transition between $S_{1/2} \leftrightarrow P_{1/2}$ to Doppler cool the ion and cause it to fluoresce; fluorescence can be measured using a photo-multiplier

mass	138	137	136	135	134	133
abundance	71.7%	11.2%	7.9%	6.6%	2.4%	-
I	0	3/2	0	3/2	0	1/2
S_Δ	-	8 GHz		7 GHz		10 GHz

Table 2.1: Relevant information about the isotopes of barium. ^{133}Ba$^+$ is a synthetic, radioactive isotope and is not naturally occurring. I is the nuclear spin and S_Δ is the splitting in the $S_{1/2}$ ground state.

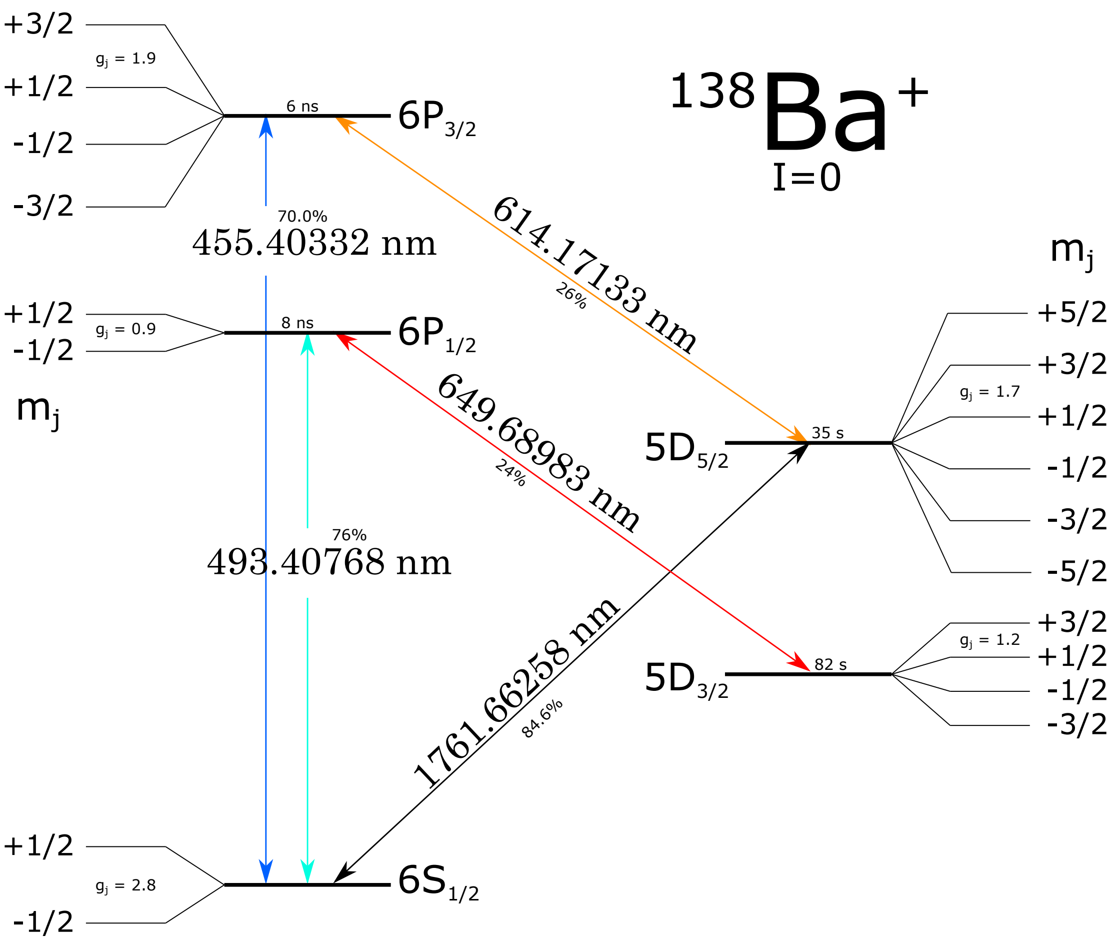

Figure 2.2: ^{138}Ba$^+$ electronic energy structure.

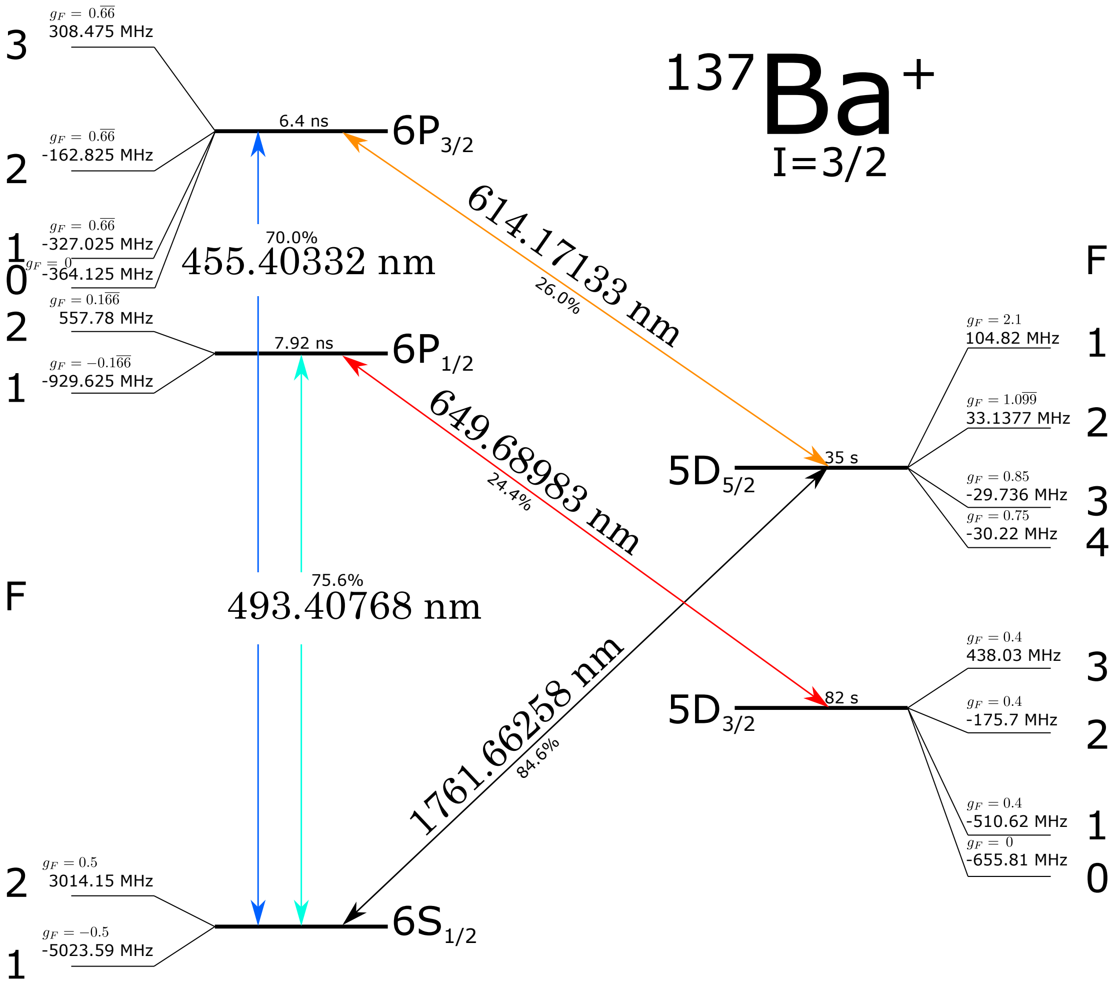

Figure 2.3: ^{137}Ba$^+$ electronic energy structure.

tube (PMT) or a camera. The $P_{1/2}$ state has a $\sim 25\%$ probability of decaying into the $D_{3/2}$ (lifetime $\sim 80\,\mathrm{s}$), and so a 650 nm laser is used to drive the dipole transitions $D_{3/2} \leftrightarrow P_{1/2}$ to keep the electron in the fluorescence cycle. This laser is called the repump laser. ^{137}Ba$^+$ has large splittings in these energy levels, so an electro-optic modulator (EOM) is used to impart sidebands onto the laser which can drive all of the transitions needed. A 1762 nm stabilized laser can be used to drive different quadrupole transition from $S_{1/2} \leftrightarrow D_{5/2}$, as demonstrated in Chapter 4. To flush out this state, a 614 nm can be used to drive the $D_{5/2} \leftrightarrow P_{3/2}$ dipole transition, from which the ion will decay back into the ground state. Finally, Raman transitions between the ground states or the $D_{5/2}$ metastable states are typically driven using a 532 nm laser.

2.1.3 Quantum computing

There are many types of problems in mathematics which are classified as NP (nondeterministic polynomial), meaning that efficient algorithms have not yet been found to solve them on a classical computer. These problems are very difficult for regular computers to solve because the time and resources required to solve them scale exponential as you go to higher inputs. One very famous example of an NP problem is finding the prime factors of an integer. With quantum computers, however, this problem is efficiently solvable. Something about quantum mechanics gives quantum computers the ability to more easily solve many problems which would be very difficult on classical computers. In addition to these obvious algorithmic advantages, many quantum processes can also be much more easily simulated using the quantum system of a quantum computer. This makes sense: the weirdness of quantum mechanics can more easily be simulated using other quantum systems. Because of these discoveries, quantum computing has taken off in recent years, with industry cropping up around superconducting and trapped ions quantum computing especially.

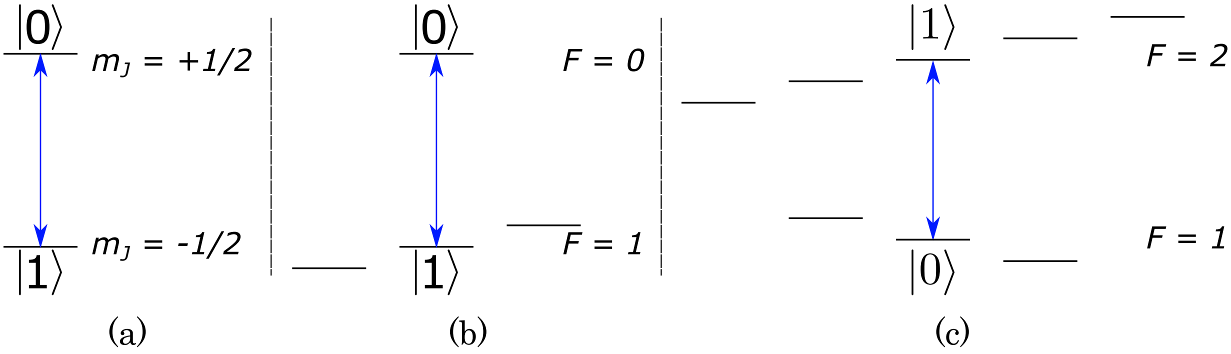

Figure 2.4: Some examples of qubits. (a) A Zeeman qubit encoded in the m_J states of an $I = 0$ ion. (b) A simple HF qubit encoded in the m_F clock states of an $I = 1/2$ ion. (c) A HF qubit encoded in the m_F clock states of an $I = 3/2$ ion.

In order to build a quantum computer, the following DiVincenzo criteria must be satisfied:

1. Ability to encode basis states. (define a qubit)

2. Stability of these basis states against decoherence. (the qubit must be coherent enough to perform many operations)

3. Ability to prepare an initial state (state preparation).

4. Ability to reliably measure out the state in the basis (measurement).

5. Ability to perform arbitrary single-qubit gates (single-qubit gates).

6. Ability to entangle two qubits (two-qubit gates).

In trapped ions, all of these criteria have been met. Most commonly, a qubit is defined using two of the electronic ground states (see figure 2.4). In Zeeman qubits, these are the spin up and spin down states. In HF qubits, things get a little bit more complicated. For ions with nuclear spin $I = 1/2$, the electronic structure is simpler and there is a natural choice for the qubit states. The clock states with quantum number $m = 0$ are chosen because they both have the least amount of magnetic field sensitivity, resulting in what is called a clock qubit. With higher nuclear spin such as $I = 3/2$, the choice is more arbitrary, but often at least one of the states is chosen as a stretched state (maximum m) because of the state preparation we will talk about later. It's also possible to use a metastable state such as the $D_{5/2}$ level to encode one or both qubit states to create what's called an optical or metastable qubit respectively [46]. Clock qubits in trapped ions can have quite long coherence times, on the order of seconds to minutes [47]. The main errors limiting Zeeman qubits and non-clock HF qubits are magnetic field errors coming from the magnetic field sensitivity of the qubit states. These errors are known and there have been techniques developed to mitigate them, so these types of qubits should also be able to reach a similar coherence as clock states [48, 49]. This coherence time is already extremely long compared to the typical gate operation time which is on the order of microseconds; in fact, trapped ions have a coherence to gate time ratio on the order of a million, which is the best of all quantum information platforms [2]. This means that for a trapped ion quantum computer with the best coherence and the best fidelities possible, on the order of a million gates can be coherently performed.

In clock qubits, state preparation is very easy because of their specific HF structure. The $S_{1/2}$ state has HF levels $F \in \{0, 1\}$, and the $P_{1/2}$ level also has $F' \in \{0, 1\}$ HF levels. Dipole transitions result in the transition between $|S_{1/2}, F = 0\rangle \leftrightarrow |P_{1/2}, F' = 0\rangle$ levels to be forbidden. So to perform state preparation in the $F = 0$ state, all you have to do is drive a dipole transition from $|S_{1/2}, F = 1\rangle \leftrightarrow |P_{1/2}, F' = 1\rangle$. After several cycles, the ion is very likely to have decayed into the HF ground state $F = 0$, which has no degeneracy. For Zeeman and more complex HF qudits, state preparation is not as simple. The easiest way

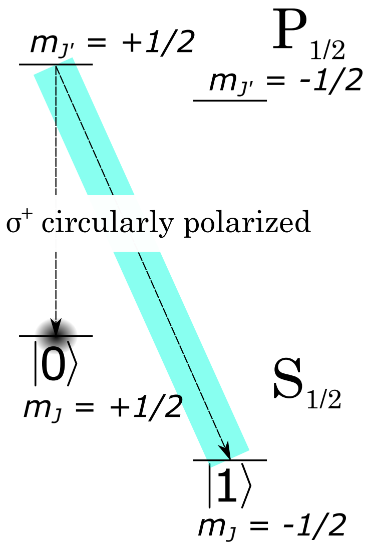

Figure 2.5: σ^+ or σ^- polarized light driving the dipole transition from $|S_{1/2}, m_J = \mp 1/2\rangle \leftrightarrow |P_{1/2}, m_J' = \pm 1/2\rangle$, is used to move the electron population into the $m_J = +1/2$ or $m_J = -1/2$ stretched state respectively. The same scheme can be used to pump into the stretched states of $I > 1/2$ ions.

of doing it is to drive transitions into the excited $P_{1/2}$ level with light which is polarized to only drive transitions which change the quantum m number in one direction (see Figure 2.5). After driving these transitions for many cycles, the electron will eventually reach a stretched state with high probability. In this work, we demonstrate this polarization technique to achieve state preparation with around 1% error. The polarization method for state preparation is not nearly as high fidelity as the simpler clock qubit method. To reach similar fidelity state preparation as in a clock qubit, other more complicated methods involving the quadrupole transition to the $D_{5/2}$ state can be used [8].

For readout of the qubit state, the $I = 1/2$ clock qubit again has a very simple procedure. Because of the aforementioned forbidden transition from $|S_{1/2}, F = 0\rangle \leftrightarrow |P_{1/2}, F' = 0\rangle$, if the $|S_{1/2}, F = 1\rangle \leftrightarrow |P_{1/2}, F' = 0\rangle$ transition is driven, the ion will never decay into the $|S_{1/2}, F = 0\rangle$ state. By collecting fluorescence while driving this transition, one can discriminate between the two qubit levels without them mixing during the measurement. If the ion is seen as bright, the qubit is known to be in the $|S_{1/2}, F = 1\rangle$ state, otherwise it is in $|S_{1/2}, F = 0\rangle$. The Zeeman and $I > 1/2$ HF qubits do not have such a forbidden rule to take advantage of. Any dipole transitions driven will mix all of the ground state levels. In order to discriminate between the qubit states, often a quadrupole transition

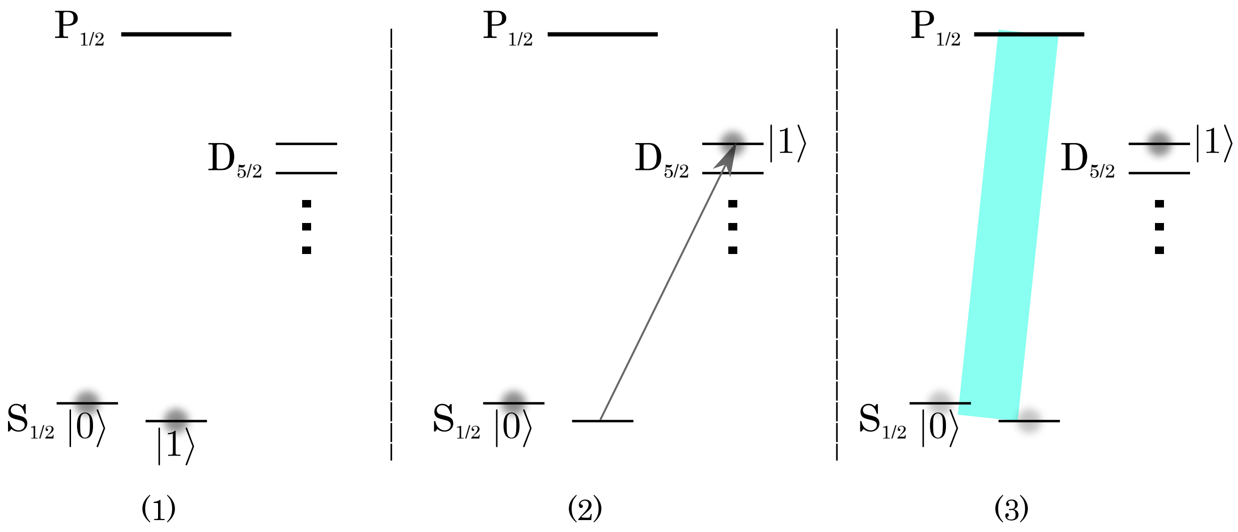

Figure 2.6: State readout of a Zeeman or $I > 1/2$ qubit. (1) Initially, all state population is in the ground $S_{1/2}$ state. (2) The $|1\rangle$ state is moved to the $D_{5/2}$ state to hide it from the fluorescence lasers. (3) The ion is fluoresced on the $S_{1/2} \leftrightarrow P_{1/2}$ transition. If fluorescence is seen, the ion is measured to be in state $|0\rangle$, otherwise it is measured to be in state $|1\rangle$.

to the $D_{5/2}$ level is utilized (see Figure 2.6). Moving one of the qubit states into this metastable state allows one to fluoresce the remaining qubit state without disrupting the stored state [8, 25, 33, 34, 36–39]. This process is called shelving, and it has been used to demonstrate the best SPAM error (1×10^{-4}) of any ion qubit [8]. It can also be used to create an optical qubit, which uses one of the optical pumping techniques described in the previous paragraph, and where measurement is simply done by fluorescing the ground state.

Single qubit operations look very similar for all types of qubits, and there are many different ways to perform them. The simplest way to perform single qubit gates within the $S_{1/2}$ ground level is to direct microwave frequencies of 1 GHz to 12 GHz at the ion through a microwave horn. This method is global unless you use magnetic field gradients [50], so a different method is more often used in order to be able to individually address ions. A Raman transition is a two-photon transition using the excited states; this effectively creates a virtual intermediate state which allows for performing coherent operations between states in the ground level depending on the frequency difference between the two Raman lasers. The lasers used for Raman transition are typically at either 532 nm or 369 nm, depending on the specific ion being used. For optical qubits, single qubit gates can easily be performed by the laser used to shelve. All of these operations can be done in microseconds, and the

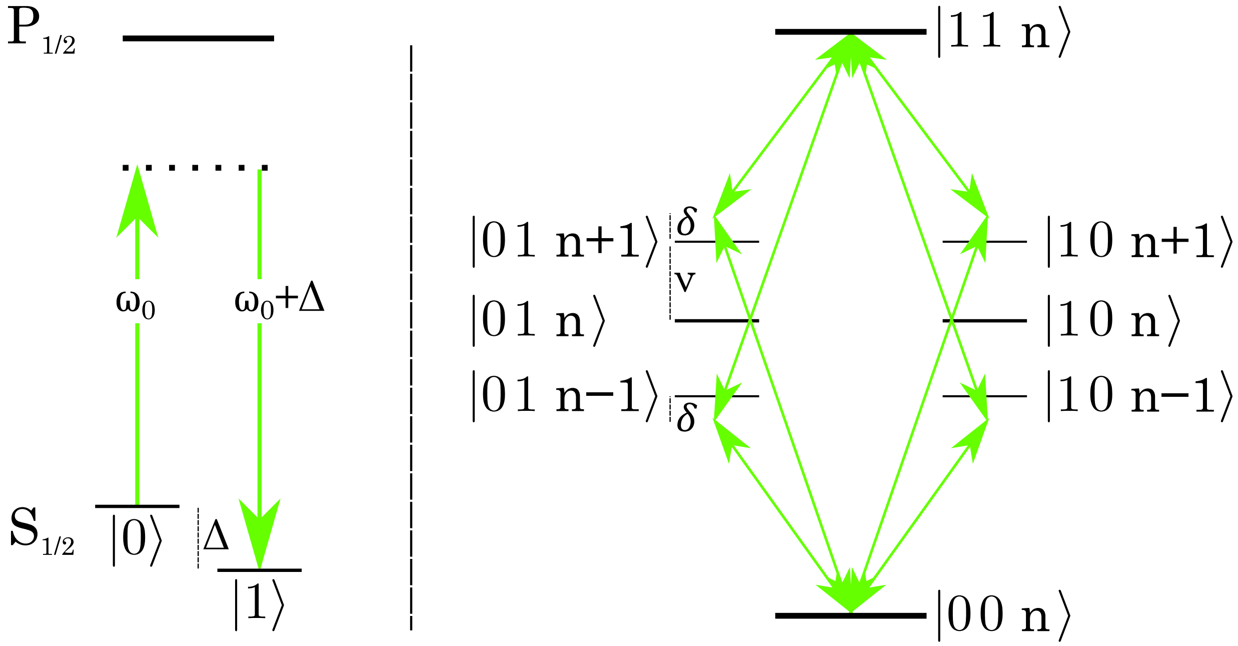

(a) (b)

Figure 2.7: (a) A single qubit gate uses a two-photon Raman transition. (b) An entangling gate uses multiple Raman transitions driving motional modes.

best results have error on the order of 1×10^{-5} [6,7,51].

Entangling gates can be done with microwaves and magnetic field gradients [52], but much more often, Raman lasers are used [7]. Two qubits within a chain have shared motional modes in each direction of confinement. One of these motional modes can be picked to be used as a bus for correlating the two ions and generating an entangling operation such as a controlled phase gate (see Figure 2.7(b)). If ω_0 is the frequency to drive a qubit transition directly and ν is the frequency of a motional mode, you set the two Raman laser frequencies to be $\omega_0 \pm (\nu + \delta)$, where δ is some small detuning. Driving the motional sideband in this way causes the ions be displaced from their equilibrium, following a circular path in phase space; crucially, different qubit states follow opposite trajectories, and they both return to the origin at the same period. If the Raman lasers are shined onto the two ions for this period of time, the ions will become entangled through the motional bus, but their motion will end up being completely decoupled from the mode.

The resulting state evolution looks like

$$\begin{aligned}|00\rangle &\rightarrow |00\rangle\\ |01\rangle &\rightarrow -|01\rangle\\ |10\rangle &\rightarrow -|10\rangle\\ |11\rangle &\rightarrow |11\rangle,\end{aligned} \tag{2.7}$$

where a phase is added only when the two qubits are in opposite states. With this operation, simply adding some single qubit gates results in the more useful z-basis phase gate or the controlled-not gate. Entangling gates in optical qubits can again use the shelving laser, however they tend to be much slower. These phase entangling gates using Raman lasers have been demonstrated in trapped ions with errors on the order of 1×10^{-3}. For slower optical qubits, entangling gates have been demonstrated with errors on the order of 1×10^{-2}.

Satisfying the DiVincenzo requirements above allows one to start doing full quantum computation, but they are not sufficient to make a quantum computer which can be better than a classical computer (i.e. solve NP problems). Qubits with high enough fidelities are also required. Further, even if the fidelities are quite good, an error correction scheme is still necessary to mitigate the errors caused by decoherence of the qubits. All error correction schemes involve using extra qubits, or using multiple qubits together to make up one logical qubit. This results in even more qubits needed to compose a useful quantum computer. Overall, it is likely that many thousands of qubits will be needed in order for a quantum computer to be able to solve problems better than classical computers can.

This is especially a problem for ion traps, which can only contain on the order of 100 ions within a single chain. Within those chains, it's currently only possible to individually address around half of the ions using the best techniques such using a multi-channel acousto-optic modulator (AOM). One solution to this problem is to use complex electrode geometries which can contain multiple traps which can be controlled and moved around, called the quantum charge coupled device (CCD) architecture [53]. Another solution is to use another qubit medium, typically photons, to connect networks of ion traps together, called photonic interconnects [54, 55]. A much less explored solution which can complement these two strategies is to use more of the computational space within the quantum systems being used, going to d-level qudit quantum computation instead of just 2-level qubits. Much of the theory and background was established long ago [18,32,56–63], which led to many proposals [64–66], especially more recently [33, 67–73]. There have also been several publications which demonstrate qudits on trapped ion systems [34–38, 74–78], and on other quantum information platforms [79–83]. With all of these proposals and demonstrations, interest in developing helpful techniques [84–89], quantum error correction [90–96], and parallel readout/state tomography [97–99] in qudit systems has been increasing. All of this interest [100,101] is due to advantages that qudits exhibit in quantum error correction [20–23,102,103], quantum algorithms [15–17,104–111], and quantum simulations [67,112–118].

2.1.4 Qudits

A qudit is just a d-level quantum information unit; instead of using $d = 2$ levels as in a qubit, $d > 2$ levels are used. The DiVincenzo requirements can be generalized and stated for qudits by simply replacing the word qubit with qudit. Not only that, but many of the operations are the same or similar in trapped ion systems. The state preparation, in fact, is exactly the same, optically pumping either to a non-degenerate dark state such as the $|F = 0, m_F = 0\rangle$ ground state of an $I = 1/2$ ground state, or to a stretched state of a Zeeman or $I > 1/2$ qudit using polarized light or other techniques [8].

The qudit states can be picked from the HF ground states as shown in Figure 1.3, or chosen as some combination of these and $D_{5/2}$ metastable states, as we do in section 4.3. It should be noted that no matter which qudit states are picked, at least one will almost always have to deal with some level of magnetic field sensitivity; there is no magic set of states such as those used in many qubits. This does not have to be an issue though, as magnetic field noise can be suppressed using known techniques, resulting in magnetic field sensitive qubits with similar coherence times as their insensitive counterparts [48].

It turns out that single qubit gates can be easily constructed by picking qudit states which can be connected by individual transitions, like the encoding in Figure 1.3(a). Any single qudit unitary can be decomposed into a series of no more than $d(d-1)/2$ individual rotations between different qudit states [32,33]:

$$\hat{U} = \hat{V}_K \hat{V}_{K-1} \dots \hat{V}_1 \hat{\Theta}. \tag{2.8}$$

Each $\hat{V}_K$ is an individual Givens rotation between two of the qudit states,

$$\hat{V}_{jk}(\theta, \phi) = \exp\left(i\theta\left[e^{i\phi}|j\rangle\langle k| + e^{-i\phi}|k\rangle\langle j|\right]\right), \tag{2.9}$$

and $\hat{\Theta}$ is an extra phase in the diagonals of the unitary, which can be cancelled with no more than $2(d-1)$ operations. Here, j and k are the two qudit states being addressed, θ is the pulse angle, and ϕ is the phase of the operation. As an example, the following are the generalized qutrit Pauli gates:

$$\begin{aligned}
\hat{X}_3 &= \hat{V}_{01}\left[\pi/2, \pi/2\right] \hat{V}_{12}\left[\pi/2, \pi/2\right] \hat{V}_{01}\left[\pi, 0\right] \\
\hat{Y}_3 &= \hat{V}_{01}\left[\pi/2, \pi/2\right] \hat{V}_{12}\left[\pi/2, \pi/2\right] \hat{V}_{01}\left[\pi/2, 7\pi/6\right] \hat{V}_{01}\left[\pi/2, \pi/2\right] \\
\hat{Z}_3 &= \hat{V}_{12}\left[\pi/2, \pi/6\right] \hat{V}_{12}\left[\pi/2, \pi/2\right].
\end{aligned} \tag{2.10}$$

Entangling gates on qudits can be generalized directly from the standard Mølmer-Sørensen (MS) gate [33–36]. This involves using more pairs of detuned Raman beams driving between pairs of qudit states (see Figure 2.7) to perform entangling gates as described in section 2.1.3. This kind of generalization of the MS gate results in a messy entangled state such as the following qutrit state [33]:

$$|\Psi_0\Psi_1\rangle = \left(\frac{1}{4} - \frac{1}{2}e^{-i\frac{\pi}{4}}\right)|0,0\rangle - \frac{1}{4}|0,2\rangle - \frac{1}{2}|1,1\rangle - \frac{1}{4}|2,0\rangle + \left(\frac{1}{4} + \frac{1}{2}e^{-i\frac{\pi}{4}}\right)|2,2\rangle. \quad (2.11)$$

This state is technically entangled, and the operation is technically an entangling operation. If you combine this kind of entanglement with single qudit gates, any quantum operation can be performed. Just add some single qudit gates to this particular generalized MS gate and it can be transformed into say, the Toffolli gate.

When using multiple energy levels to encode different states, it is much harder to discriminate between each of the individual states in a measurement. Simply using the standard fluorescence technique described in previous sections would cause all of the qudit states in a HF qudit to be measured, destroying all of the quantum information and revealing nothing about the qudit state. In order to discriminate between the qudit states, the metastable $D_{5/2}$ level is used as a shelf for quantum information [33–38], similar to the shelving measurement described in Section 2.1.3 (see Figure 2.6). For a qudit measurement procedure using this shelving metastable level, drive a π-pulse quadrupole transition from each of the $S_{1/2}$ qudit states (except for one) into a different $D_{5/2}$ level using a laser. With all but one of the qudit states hidden in the shelf level, fluorescence measurement can proceed on the remaining state. Next, return one of the shelved states using another π-pulse and perform a fluorescence measurement on it. The first fluorescence measurement for which fluorescence is detected determines which state the qudit was in. This measurement scheme was demonstrated in Chapter 4 of this work. An optical qudit is similar, but without the extra shelving step at the start since the qudit states are already in the $D_{5/2}$ level.

2.2 Apparatus

2.2.1 Ion trap, electronics, lasers, and optics

We use an RF Paul trap, like the one depicted in Figure 2.1. On each rod, we apply on the order of 50 V to 70 V RF to the rods at a frequency of 20.772 MHz to confine ions radially. Each set of opposing rods has the same applied RF, with the other set of opposing rods having an opposite polarity. The source of this RF has an RF transistor-transistor logic (TTL) switch in the line, allowing us to quickly toggle the trapping potential off or on, a feature which we use to perform direct-ion loading. One of the radial directions is squeezed by adding around 3 V DC voltage, which helps with cooling and confining the ions in a chain. The voltages can also be adjusted to push the ion chain to the RF null and to compensate for micromotion. Each needle has around 9 V DC voltage for confinement in the axial direction [41]. The trap is mounted inside of a spherical hexagon vacuum chamber which is pumped down to under 1×10^{-10} mbar to reduce background collisions with the trapped ions. Six of the side viewports are used for delivering lasers while two of them are used for pumping the system and delivering electronic connections into the chamber. On each of the viewports, magnetic field coils are mounted to be able to control the quantization axis at the ions and to compensate for the earth's magnetic field [39]. Typically, around 2 A to 5 A of current is run through either one or a pair of opposite coils (top right and bottom left coils in Figure 2.8) for generating the quantization magnetic field of around 0.4 mT to 1 mT.

For ablating, a $BaCl_2$ natural abundance target was mounted into the vacuum chamber below one of the viewports. A pulsed Nd:YAG 532 nm laser is used to ablate and generate neutral barium for ionizing and trapping. This laser is reflected off of a mirror on a motorized mount so that we can easily change the position the laser hits on the target. It is directed into the vacuum chamber from the top viewport. This pulsed laser and the ablation method is described and characterized in detail in Chapter 3.

To ionize neutral atoms ablated from the target, we use a two-step photoionization process with the first step driving one of the electrons in neutral barium from the ground state to the ${}^1P_1$ intermediate state, at 553.7 nm. Changing the frequency of the laser used to drive this transition allows us to preferentially trap one of the isotopes of barium in our trap. In our setup, we normally trap either ${}^{138}\text{Ba}^+$ or ${}^{137}\text{Ba}^+$, the two most abundant isotopes of barium. The laser we use to drive this transition is an 1107 nm external-cavity diode laser (ECDL) [119]. This infrared (IR) laser is passed through a frequency doubler, resulting in 554 nm light, which we pass through a slow shutter, a half-wave plate (HWP), and a linear polarizer (used for controlling the power). The next step of our photoionization

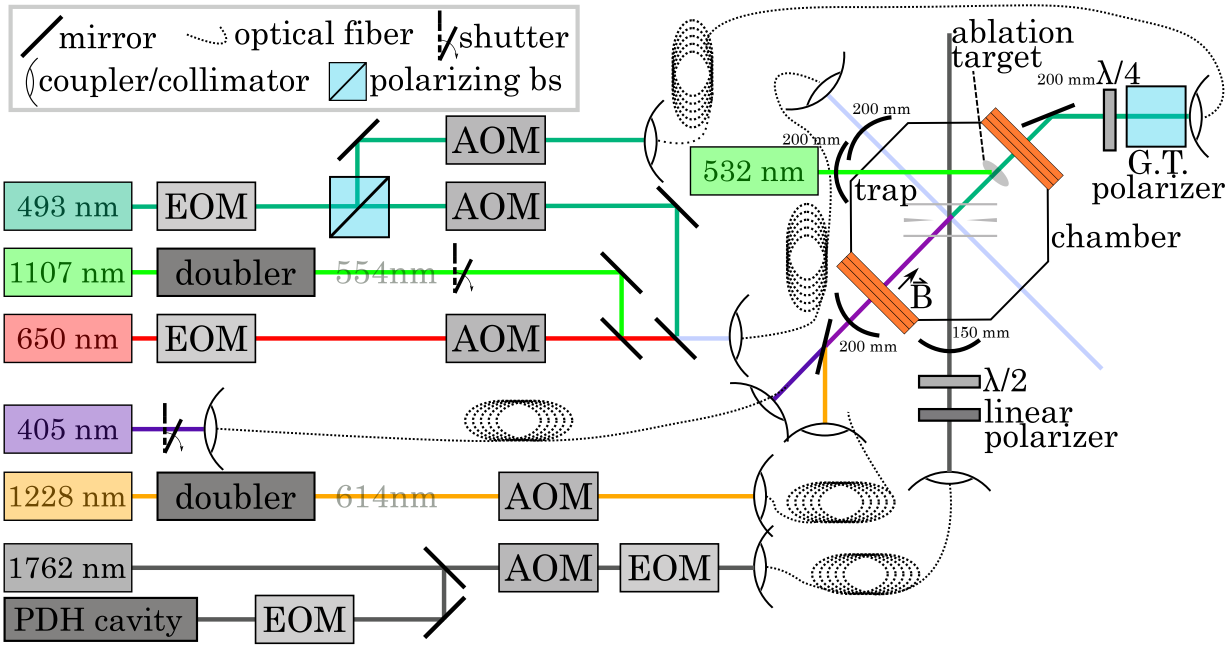

Figure 2.8: Optics, trap, and ablation setup (not all mirrors and lenses shown). A legend is shown in the top left box. All lasers are focused into the chamber using convex mirrors. Generally, optical fibers are used to deliver lasers to the vacuum chamber.

process uses a 405 nm bare diode, which also has a slow shutter for turning it on or off to the trap.

For fluorescence readout and Doppler cooling of trapped ions, we have two ECDL's [120] at 493 nm and 650 nm for driving the two dipole transitions from $S_{1/2}$ and $D_{3/2}$ to $P_{1/2}$. We call the 493 nm laser the cooling laser, and we use fluorescence from this laser to measure ions. The 650 nm laser is called the repump laser, because it is necessary to keep the electron from becoming dark in the $D_{3/2}$ state, which it is very likely to do given the nearly 25% branching ratio. Both of these lasers have AOM's and EOM's in their beam paths for fast switching them on or off to the trap, and adding red and blue-shifted frequency sidebands to the lasers. The AOM's are driven with 200 MHz RF, and powers around 1 W. The cooling laser is split off into two paths using a HWP and a polarizing beam-splitter (PBS), one of which is used for cooling and measurement, while the other is used for state preparation by optical pumping. The optical pumping beam also has an AOM in its path (same RF parameters), and its polarization is controlled using a Glan-Thompson polarizer and quarter-wave plate (QWP) before being sent to the trap. Both fluorescence lasers (493 nm and 650 nm) are combined with the first-step photoionization

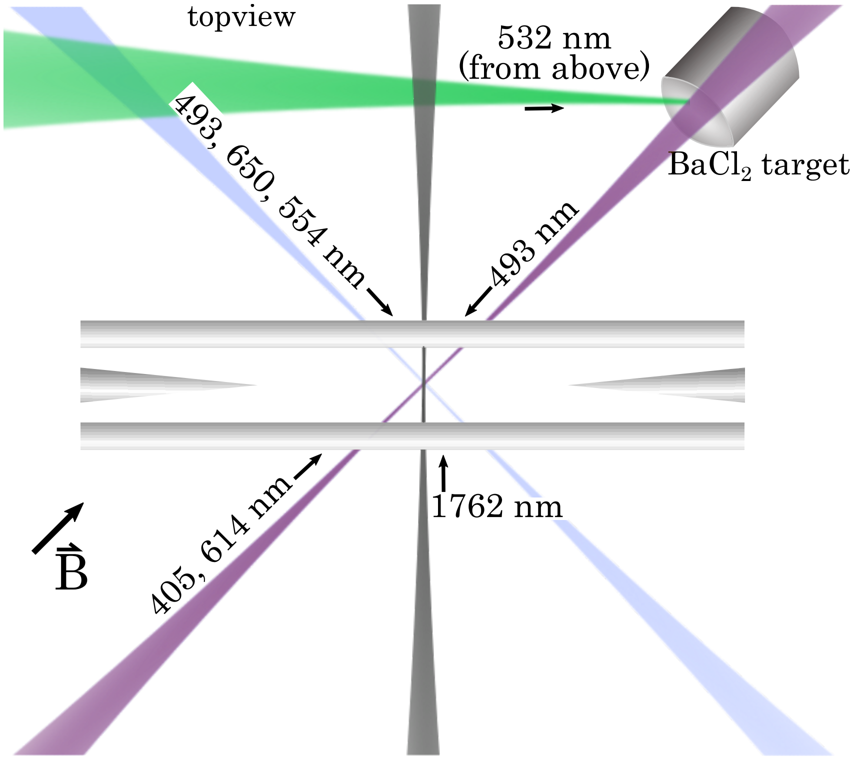

Figure 2.9: Delivery of lasers to ion. Lasers focus through the trap rods, passing through the trapping region to address ions. The ablation laser is delivered from the top viewport.

laser (554 nm) using a series of dichroic mirrors with different cutoff frequencies, and are coupled into one optical fiber before being sent to the trap. We call this beam the combined beam. For more details about these lasers, see References [39, 121].

To drive quadrupole transitions from the ground state to the metastable $D_{5/2}$ state, we use a 1762 nm narrow-linewidth laser which was put together by Stable Laser Systems (SLS) [122]. This laser is an ECDL which has a pickoff coupled into a stable laser cavity which uses a Pound-Drever-Hall (PDH) locking system to keep the laser frequency locked to one of the sidebands imparted by an EOM in the path. Using this locking method, the laser is able to achieve a linewidth on the order of 1 Hz. The laser setup also has an intensity stabilization stage which uses an interferometer to cancel any intensity fluctuations in the optical fiber which the laser is coupled into for delivery. Before being sent into the chamber, the polarization is purified using a linear polarizer and controlled using a QWP. It's then telescoped to a larger size using a convex and concave mirror pair so that we can focus it down tighter at the ion. The bring-up and operation of this laser, its optics path, and how we use it are detailed further in Section 4.1.

To drive out of the $D_{5/2}$ metastable state more quickly than its natural lifetime, we drive the $D_{5/2} \leftrightarrow P_{3/2}$ transition using a 1228 nm laser [123] which is frequency doubled to 614 nm. This shelving repump laser is sent through an AOM with 200 MHz RF at around 1 W for quick switching, then fiber coupled for delivery to the vacuum chamber area.

The first-step ionization laser (554 nm), the cooling lasers (493 nm, 650 nm), and the shelving repump laser (614 nm) all have pick-offs which are sent to a wavemeter [124] with 10 MHz precision. The wavelength of each laser is read out and can be corrected using a proportional, integral, derivative (PID) system fed into the piezo control of the ECDL's. This allows us to keep the laser frequencies locked to the atomic transitions they drive even as they drift from temperature changes, as well as change the frequencies depending on isotopes we wish to trap or scans to perform. We re-calibrate the wavemeter daily using a stable Helium-Neon (HeNe) laser source of known frequency.

Figures 2.8 and 2.9 show where each of these lasers is delivered into the vacuum chamber and the ion trap center. The combined beam (554 nm, 493 nm, 650 nm) is sent in from the top left (in Figure 2.9) viewport of the vacuum chamber in one beam which is focused down to a 35 µm radius at the ion trap using a 200 mm concave mirror just before the vacuum chamber. The saturation power of these beams is then $P^g_{sat} = 0.56\,\mu$W, $P^b_{sat} = 0.84\,\mu$W and $P^r_{sat} = 0.37\,\mu$W respectively. The direction of this beam was chosen so that all trap axes (radial x, y, and axial) can be cooled using just these cooling lasers. The 554 nm is sent through this viewport so that its wavevector is perpendicular to the path ablated atoms take to the trap center; this reduces Doppler shift and broadening so we can selectively drive this transition for different isotopes. The cooling 493 nm and 650 nm lasers have around 10 µW to 100 µW and 150 µW to 250 µW of power at the trap respectively, while the ionization laser can be varied from 1 µW to 200 µW by changing the angle of the HWP in its beam path.

To perform optical pumping for state preparation, the wavevector of the laser must be along the quantization magnetic field axis. So the 493 nm optical pumping beam is delivered to the trap through the top right (in Figure 2.9) viewport and its polarization is well controlled to have either left σ^- or right σ^+ polarization. This beam has around 2 µW laser power and is focused down to a 35 µm radius at the trap center using a concave mirror with focal length 200 mm.

The second step photoionization laser (405 nm) and the shelving repump beam (614 nm) are aligned into one beam and delivered through the bottom left (in Figure 3.3) viewport. This limits the cross section in which we drive both steps of the photoionization to be within the the trapping region, resulting in trapped ions with a lower potential energy which can be cooled more easily. These two lasers are focused down to a 35 µm radius at the trap center using a 200 mm concave mirror, giving the 614 nm laser a saturation power of $P^o_{sat} = 0.54\,\mu$W. The ionization laser and shelving repump laser have 2000 µW and 10 µW laser power at the trap respectively.

The 1762 nm laser is focused to a 23 µm radius using a 150 mm lens and sent into the vacuum chamber through the bottom (in Figure 3.3) viewport. With this orientation, it is at a 45° angle to the quantization magnetic field, which is a useful orientation for maximizing the strengths of different quadrupole transitions [39], as described in Section 4.2. See Chapter 4 for more details on this laser and optics used to deliver it to the trap.

Most of the laser beams delivered to the vacuum chamber have a flipper mirror setup to deflect the beam to a power sensor for remotely checking the laser powers.

All ECDL's used in our lab have current and temperature control of the diode stage and piezo control of the cavity grating angle, allowing overall control of the power and frequency of the laser using the current and temperature, and fast control of the frequency using the piezo devices on their cavities. Most of our lasers are controlled using either a DLCPro Topica laser controller [125], the Thorlabs PRO8000 [126] controller, or the moglabs DLC202 [127].

All of the lasers which are read out in the wavemeter use a PID which is built into the wavemeter software, and the error signal is fed into either the laser controller (with voltage gain and delivery built in), or into an external piezo amplifier. This signal is then fed into the piezo modulation of the lasers.

In most of our optics lines we have either a slow shutter or a fast AOM switch. The shutters are able to switch a line on or off in milliseconds. AOM's deflect part of the laser beam at an angle which depends on the RF frequency being applied while the ratio of deflected laser power depends on the RF power being applied. The deflected laser beam is coupled into an optical fiber. So if we turn off the RF being applied, we can turn off the deflected beam and none of the laser power will be coupled into the fiber. This switching can be performed as quickly as we are able to switch the supplied RF, which can be around 50 ns to 1000 ns depending on the RF switch used. We use fast switching for lasers which need to be quickly switched during experiments, such as the cooling lasers and the shelving laser. The RF power delivered to the AOM's can be changed using programmable attenuators, thus changing the laser power being deflected, coupled, and sent to the trap.

To image neutral fluorescence and ions in the trap center, we use a one inch objective system [41] optimized for collecting 493 nm light, with an numerical aperture (NA) of 0.26. With this aperture, we can collect around 1.75% of light from the ion position. The image is collected in a lens tube setup and sent through a 1:1 telescope with 100 mm focusing lenses and an aperture in the middle, which acts as a spacial filter, reducing light being collected from directions other than where the ion is. We use another aperture to close the image down to a smaller field of view to reduce the background noise and get a stronger signal-to-noise (SN) ratio. This is especially helpful for measuring fluorescence of moving neutral atoms, where we only want to collect photons from atoms which are passing through the trapping region and the lasers. A dichroic mount in the lens tube setup allows us to switch to different color filters. We have band pass filters which only allow wavelengths of light near 493 nm or 554 nm, and we also have a dual band pass filter which allows both of these wavelengths through. For normal use, the dual band pass filter is used so that we can see neutral fluorescence when loading and see the ion once it's loaded. The image can be directed to either a PMT or a CCD camera. For both of these paths, the image is focused onto the readout device using a 125 mm lens. The CCD camera is used for just seeing chains of ions and aligning laser paths, while the PMT is used for measuring the overall brightness of either an individual ion or a chain of ions. Each pixel on the camera corresponds to 1.9 µm at the ion position. Most experiments need to collect photon counts and so we use the PMT most of the time.

$^{138}\text{Ba}^+$ has very simple energy structure (Figure 2.2), and so the EOM is not needed to cause it to fluoresce. $^{137}\text{Ba}^+$ on the other hand has a more complex energy structure (Figure 2.3) which requires additional frequencies in order to cause it to fluoresce. We use EOM's to impart additional sidebands onto the lasers in order to generate all of these additional frequencies. The ground state in $^{137}\text{Ba}^+$ has a HF splitting of $\sim 8\,\text{GHz}$, and both of these states must be addressed using the 493 nm laser. There are many ways of driving these transitions, but the one we found to be most reliable for us is to drive both states through the $|P_{1/2}\ F' = 2\rangle$ state by setting the carrier frequency in between and driving both transitions using EOM sidebands at $\sim 4\,\text{GHz}$, as shown in Figure 2.10. This allows us to stay within the lasers free spectral range of the laser when switching between the $^{138}\text{Ba}^+$ and $^{137}\text{Ba}^+$, and the overall optical power driving transitions is not reduced as much since we only have to drive the EOM with one frequency. For the repump laser, we have many more transitions to drive since there are four HF states in the $D_{3/2}$ level. We drive $|D_{3/2}, F \in \{0, 1, 2\}\rangle$ states into the $|P_{1/2}, F' = 1\rangle$ state and the $|D_{3/2}, F = 3\rangle$ state into the $|P_{1/2}, F' = 2\rangle$. Three different frequency sidebands are applied to the EOM while the carrier is used to drive the $|D_{3/2}, F = 2\rangle \leftrightarrow |P_{1/2}, F' = 1\rangle$ transition directly. This method results in frequencies in the 300 MHz to 800 MHz range, which are easy to source and apply to one EOM.

To drive different quadrupole transitions in $^{137}\text{Ba}^+$ using the 1762 nm laser, an extra EOM is used after the whole stabilization system. The transitions are driven directly using the blue sideband imparted to the laser by this EOM. This allows us to quickly and

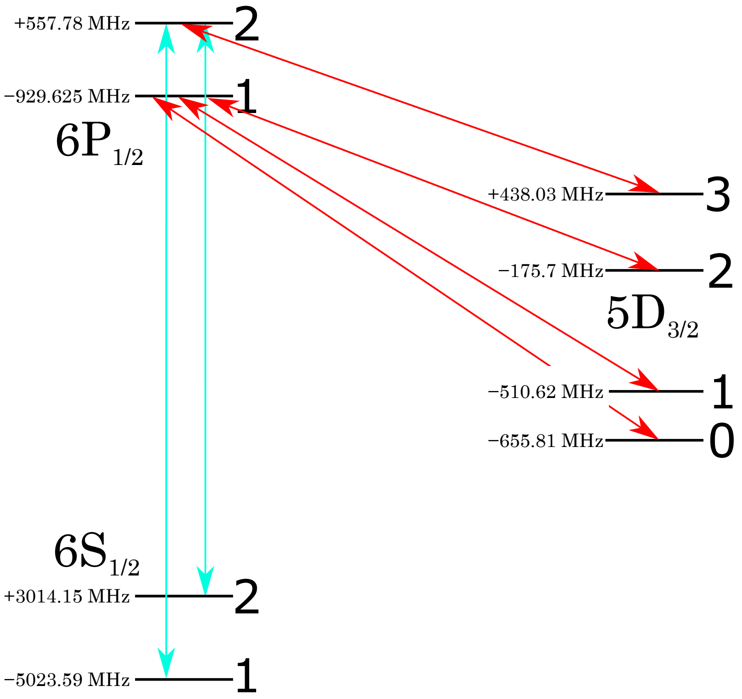

Figure 2.10: Transitions used to cause $^{137}\mathrm{Ba}^+$ to fluoresce continuously. Both $S_{1/2}$ ground states are driven through the $|P_{1/2}, F' = 2\rangle$ state. $|D_{3/2}, F \in \{0, 1, 2\}\rangle$ states are driven through the $|P_{1/2}, F' = 1\rangle$ state while the $|D_{3/2}, F = 3\rangle$ state is driven through the $|P_{1/2}, F' = 2\rangle$ state.

precisely control the frequency driving the quadrupole transition.

For generating frequencies in our lab, we use a variety of different frequency sources depending on the use case. For trap RF, we use a simple function generator with an amplifier and a balanced drive resonator [41] with a Q-factor of around 300. To generate fixed 200 MHz frequencies for driving AOM's, we use a single phase lock loop (PLL) source which is split off, amplified, and sent to the different AOM's with separate RF switches we can control through TTL. Cooling laser EOM's are driven with separate PLL's with their own amplifiers and switches, giving the ability to switch between different frequency sets for driving different transitions in the ions.

The quadrupole transition must be driven much more precisely, so the EOM in the 1762 nm line has its frequency source as an arbitrary waveform generator (AWG), which can precisely send any waveform and quickly change the frequency of simple preset waveforms. This allows us to scan over this transition precisely and quickly.

For controlling most of our devices and performing experiments, we use the Sandia National Lab published control system IonControl [128]. This system uses a Qt python user interface to control network devices and perform timed controlling of TTL's and readout of counters such as PMT's. The program is written in python, and pulse programs are written in pseudo-python, with precise timing of controls at the microsecond level. Scans can run pulse programs through a range of scan parameters, and overall experiments can be controlled by writing full python scripts which run individual scans for calibration or collecting data-sets, changing global parameters, and talking to network devices. Using IonControl, we are able to toggle TTL's of various devices such as RF switches, shutters, flipper mirrors and triggers. We are also able to change voltages being applied to the trap electrodes, frequencies of lasers, and various AWG and RF source settings.

Chapter 3

Ablation Loading of Barium Ions

In this chapter, the results of our laser ablation and loading from $BaCl_2$ targets are presented, with characterization of the process and the ablated plume of atoms, and loading rates and selectivity results. First, some background on ion loading is given, presenting the different loading methods and focusing on the method we choose to use, ablation. I give details about our laser ablation setup, and present the characterization of the laser we use to ablate. Ionization methods are presented, and details are given on the REMPI method we use in our setup.

In the later half of the chapter, our results from exploring laser ablation and loading using it are presented. First, some characteristics of the ablation process are shown. Spot lifetimes are found to be on the order of $10,000$ pulses. A conditioning effect is revealed in which a fresh spot must be ablated before it can be used to generate an appreciable atom flux using lower ablation laser fluence. This also gives access to a fluence regime in which mostly only neutral atoms are ablated, which can reduce the charge build-up more prevalent with higher fluence. The ablation plume of atoms is characterized using a time-resolved spectroscopy method (time-of-flight (TOF) spectrum). This resulted in a resolution of the different isotope peaks in the 554 nm laser spectrum, in particular, the ^{137}Ba peak we use to trap $^{137}Ba^+$. Doppler shifts can be seen, illustrating the need for the ablation plume to be perpendicular to the ionization laser. Reducing to a TOF resulted in an estimation of the temperature of ablated atoms of on the order of $35,000$ K.

Next, the results of loading of ions using ablation and REMPI are shown. Loading rates for $^{138}Ba^+$ and $^{137}Ba^+$ are measured to be around 1 and 0.1 ions/pulse respectively, a ratio which was expected based on the abundance of the isotopes. The loading rate is shown to be correlated with the neutral fluorescence we measure, which allows us to monitor what we expect the loading rate to be dynamically. Finally, results on the selectivity of our ablation and REMPI method are presented, with $^{137}\text{Ba}^+$ able to be loaded with around 3x higher probability than its natural abundance.

3.1 Ion loading - background

3.1.1 Ion loading methods

There are many different ways to produce ions to trap. First, a flux of either neutral atoms or ions which passes through the trap center is needed. Two typical ways of generating this flux are through resistive heating of an oven [26, 27, 30, 129–133], or through laser ablation [28, 29, 40, 134–141]. Resistive heating involves running current through a wire to heat a chunk of metal (with whatever isotope one wishes to trap) up to several hundred degrees. At some threshold, a continuous vapor of atoms will shed off of the metal, out of the oven, and towards the trap center. In laser ablation, a high-power pulsed laser is focused onto the surface of a target (again, with whatever isotope one wishes to trap). This huge amount of energy ablates the surface, generating an explosion, and a plume of neutral atoms, molecules, and ions is ejected. Some of these particles will pass through the trap zone where they can be trapped.

There are several advantages gained by using laser ablation instead of the traditional approach with an oven. Because of the much higher energies involved in ablation, it can directly break apart molecules from the target. This gives many more options for types of sources. For barium, this is particularly useful as barium metal reacts with oxygen within seconds [27]. To make a barium oven, one must be very careful to not let this happen, by using a glove bag or some other method to keeping it out of atmosphere. But for ablation, compound targets such as $BaCl_2$ [28, 29, 40, 140] or others [28, 140] can be used; a metal just like what's used in an oven [135–139, 142–146] could also be used. An oven, which emits a continuous flow of atoms, can contaminate the trap electrodes significantly, add stray charge in the chamber, and increase the vacuum chamber pressure more than ablation, which contaminates for a much shorter amount of time [135, 138]. This shorter amount of time also results in a lower overall heat-load near the trap [139], causing less noise and heating for trapped ions. Using laser ablation can be much faster, with the ablation itself taking on the order of nanoseconds, and trapping on the order of milliseconds.

As an aside, we did use an oven with barium metal in our trap towards the beginning. With it, we were able to load ions successfully on the order of minutes. However, this introduced a lot of micromotion to the ion from charge build-up, and so we had to compensate for it quite often. However, as mentioned in the previous paragraph, the barium metal was a challenge to install and having to work around its fast oxidation issue caused everything about trap installation to become more complicated (working in a glove bag is not so easy). In fact, we installed a fresh barium oven in the current iteration of the trap, on the opposite side of the $BaCl_2$ ablation target. However, this time the installation

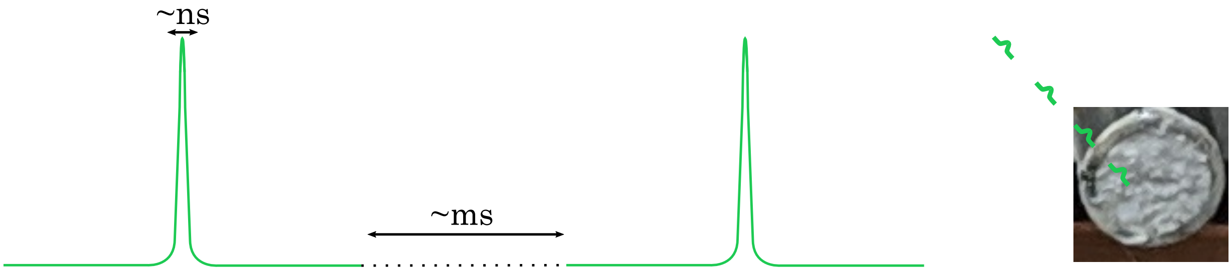

(a)

(b)

Figure 3.1: (a) A pulsed laser generates a pulse of light on the order of nanoseconds, with a repetition rate of hertz to kilohertz. (b) Our $BaCl_2$ natural abundance ablation target. The ablation laser hits the target from above.

failed. While we were transferring the barium metal into the oven, we noticed it immediately turning white, even though our glove bag was full of nitrogen air. This indicated that it was already starting to oxidize. Indeed, when we got the trap back up and working and tried to load using the oven, we were unsuccessful. With all of the barium in the oven seemingly oxidized, the oven is now just a vestige sitting in the chamber. For this reason, we now rely soley on laser ablation for trapping ions.

Many different kinds of lasers can be used to ablate, but in trap loading, typically Nd:YAG or CO2 lasers are used. The basic idea of these lasers is to pack all of the laser power into a single pulse (see Figure 3.1(a)), so that it can deposit all of its energy in a time-period of faster than $\sim 10\,\mathrm{ns}$. These pulsed lasers do this repeatedly on the order of hertz to kilohertz, with the time between pulses used to build up energy for the next pulse. This huge amount of energy is directed towards and focused onto a target containing the ion one wishes to trap. Upon hitting the target, much of the energy is absorbed immediately, causing the surface to essentially explode in the small area the laser is incident on. A hot vapor of all kinds of molecules, ions, and neutral atoms is ejected from the surface in all directions. The vast majority of these products are extremely high energy. But because of the huge amount of material generated, some products have a low enough energy to be trapped.

Note that there are typically two ablation styles used: high-energy single pulses, or lower-energy bunches of pulses. When using a higher pulse energy, typically the laser is repeatedly pulsed on the order of hertz or slower, with each shot having a high probability of loading an ion. For the lower pulse energy method, the laser is pulsed much more quickly, on the order of kilohertz. The process is more thermal, and can actually be quite similar to the oven loading scheme, but with still less contamination. In this work, we use a slow repetition rate, high energy laser for ablation and loading from single pulses.

3.1.2 Ablation setup

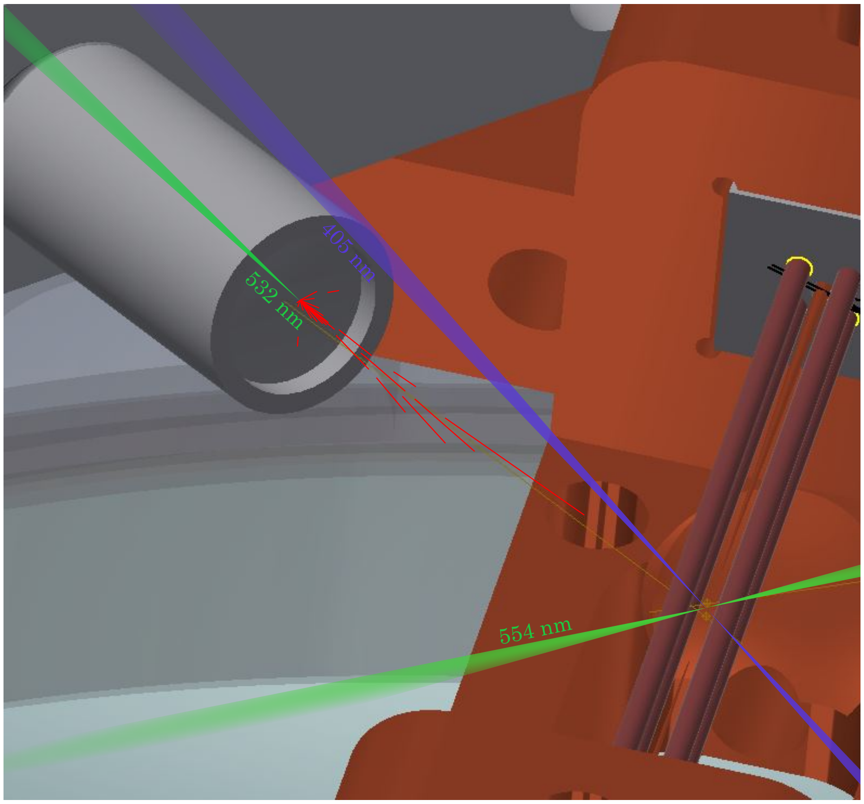

Figure 3.2: Our ablation setup: the ablation laser comes in from above, hitting the target, which points towards the trap center. The ionization lasers overlap at the trap center.

We chose to use the commonly used ablation target $BaCl_2$ for our source of barium [28, 29, 40, 140, 141]. Our target holder is a cylinder with a concave spherical surface at the end, in which we put our source (see Figures 3.1(b) and 3.2). The diameter of the cylinder is 4.16 mm, and the cylinder concave end is set in by 1 mm so that 30 g of the source can be deposited. The source of $BaCl_2$ salt was applied to the surface by mixing it with deionized water and pasting it into the concave surface. During bake-out of the vacuum chamber, the water was evaporated and pumped out, resulting in a dry source of $BaCl_2$ salt stuck to the surface. The ablation process preferentially ablates material into the direction normal to the ablation surface [147–149], so we mount the target so that it is pointed directly towards the trap center. The surface in which the source is deposited is also spherical with a radius of the distance to the trap center. For our bulk target, these things aren't crucial because the target doesn't keep to the shape of the base. The surface of the salt is also not perfectly flat or conformed to the surface. However these things can help for smaller quantity targets which do have smooth surface profiles and retain the shape of the substrate [141].

Originally, we used a tattoo removal laser which we purchased from eBay. It is a 532 nm Nd:YAG laser with a pulse-time of 7 ns and a pulse energy of up to 1000 mJ. This laser had a very large variation in pulse energy and a beam profile which was very far from Gaussian. With its terrible beam profile, it was difficult to collimate the laser for free space optics and even harder to focus the laser enough to ablate. In addition, we found that a single pulse of the flash lamp actually caused multiple pulses to be generated and each pulse varied wildly in pulse energy. This pulse energy increased quickly as the device warmed up from pulsing, with around 5x the pulse energy after using it for around 10 s. Probably the worst thing about this laser was the interference it could cause with other devices in the lab. Sometimes it would cause monitors to randomly turn off while it was pulsing, and spectrum analyzers would show white-noise increases of 30 dB every time it pulsed. While we were eventually able to trap using it and perform some characterization of the ablation, it was not reliable enough and so we acquired a more precise, consistent, and controllable laser.

We also attempted to use a higher repetition rate ultraviolet nitrogen laser at 337 nm, but were unsuccessful at ablating with it. The laser either wasn't high enough power or we couldn't get the focus to be as tight as we needed to have high enough fluence for ablating.

In the end, we settled on a minilite Nd:YAG pulsed laser [150] with a repetition rate of 1 Hz to 20 Hz, a pulse-time of 5 ns, and a pulse energy of 10 µJ to 2000 µJ. A trigger signal is sent to the laser which triggers a powerful flash-lamp and starts the laser pulse sequence. The flash-lamp excites the gain medium of the laser, neodymium atoms, which spontaneously decay quickly. A Q-switch in the cavity reduces spontaneous emission, keeping the atoms excited for longer. After some time, the potential energy is maximized in the gain medium and the Q-switch is opened. The atoms all spontaneously decay, resulting in a large amount of optical power concentrated in one small period of time. This cavity generates light at 1064 nm, which can be doubled in frequency to 532 nm using a harmonic generation crystal. The Q-switching can be done automatically by the controller or manually using another TTL; the optimal wait-time changes from pulse to pulse and is around 150 ns. We use the automatic Q-switching so that the pulse energy can be more consistent, and the timing was measured to be 142.5 ± 0.3 µs after the TTL signal.

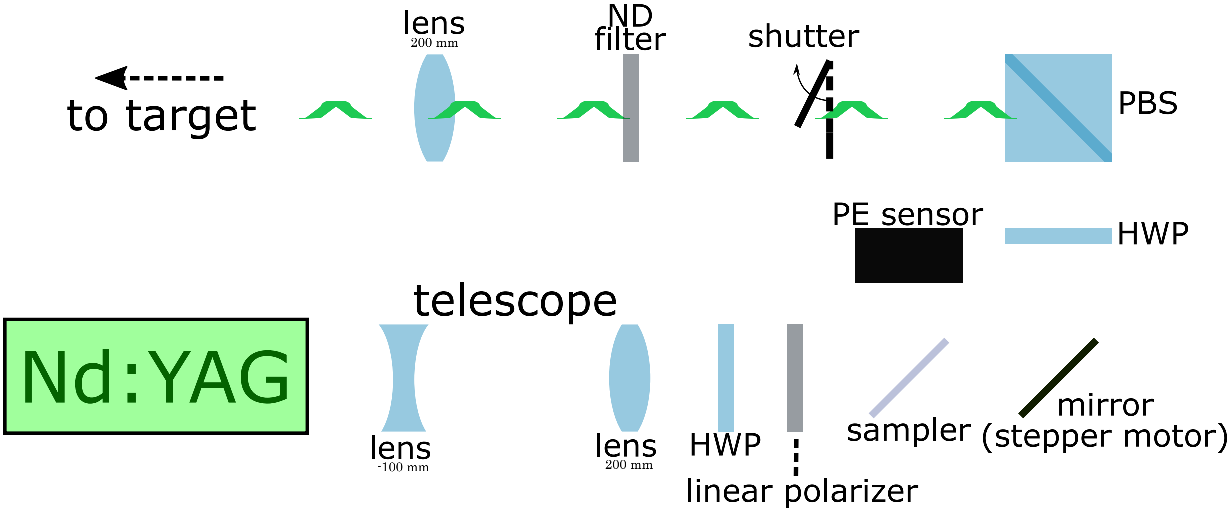

Figure 3.3: The optics used to control the ablation laser and deliver it to the $BaCl_2$ target in the vacuum chamber. The mirror has stepper motors, allowing us to precisely point the beam onto different spots on the target. A pyro-electric energy sensor (PE sensor) measures the pick-off pulse energy. A neutral-density (ND) filter reduces the power to be similar to the pick-off power.

The ablation optics configuration in our experiment is shown in Figure 2.8. We first telescope the laser using a diverging and converging lens pair with 100 mm and 200 mm focal lengths respectively. This increases the diameter of the beam from 3 mm to 9 mm, allowing us to focus the beam tighter onto the ablation target. Next, a wire-grid polarizer and a HWP pair is used to change the pulse energy of the laser. The polarizer is mounted on a remote controlled rotation mount, allowing us to precisely adjust the pulse energy we are ablating with. A beam sampler is used to pick off some power which is read out using a pyro-electric energy sensor [151]. Another HWP with a PBS allows us to split the power to another target which we won't be discussing here [40]. A neutral density (ND) filter is used to make the power being sent to the target similar to the sampled power. We use a slow shutter in the line as a fail-safe so that we only send the ablation laser when we actually want to ablate. Finally, the laser is focused down onto the ablation target using a 200 mm convex lens. The focused beam has a radius of 98 µm, and hits the target from through the top viewport of our vacuum chamber, the same one being used for the imaging objective. This focus gives us on the order of 500 spots on the target for ablation. However, the angle between the target's normal vector and the beam pointing of the ablation laser is 56°. Therefore, how well focused the laser is on the target depends on which part of the target we hit, causing the fluence to depend on the spot on the target.

Below the trap, we have mounted a camera for looking at the ablation targets. The angle is not able to see exactly where on the target we are hitting, but we can at least use it for calibrating the stepper-motor mirrors to the center of the targets and being sure that we are always hitting the target. We use the camera to recenter on to the ablation target as follows. First, we start with stepper motor positions which seem to be close to the center by eye. Next, one of the directions is swept slowly towards either the positive or negative edge of the target in that direction. The sweep is stopped when the beam is just about to fall off of the target, based on looking at the camera. This point is very subjective, but as long as the same signal is seen every time you try to find this point, it should be at least somewhat consistent. After one edge is found, the opposite edge is found in the same manner. The average of these two points is now the center position for this axis, and the process is repeated for the other axis, with the first axis set to this new center. With both axes re-centered, a new overall target center estimate is defined. But because the first guess was very rough, more iterations of the procedure should be done to get closer to the true center. We typically do around 3 iterations of this before the center position changes by a negligible amount, thus concluding the re-centering procedure. It's important that the pulse energy be set to the same value each time this procedure is done to ensure the same center is calibrated to. Every time, we use the low pulse energy mode available on the laser, and the polarizer aligned to give the minimum power.

Overall, the distance from edge to edge in the stepper motors' units is around 0.215 mm. The known distance from edge to edge is the diameter of the target, 4.166 mm. Comparing the two, we see that the ratio of actual movement across the target to stepper motor movement is $(4.166\,\mathrm{mm}_{actual})\,/\,(0.215\,\mathrm{mm}_{motor})$. The beam pointing is at an angle of 56° from the target surface normal vector, so the laser focus change from moving the ablation laser pointing using the stepper motor is

$$\Delta z = \frac{(4.166\,\mathrm{mm}_{actual})}{(0.215\,\mathrm{mm}_{motor})\cos(56^\circ)}\Delta x_{motor}. \tag{3.1}$$

This means that moving the stepper motor by Δx_{motor} millimeters moves the focus Δz millimeters in actual space. Using equation 3.1, we can find how far off our ablation laser focus is from the target center by collecting neutral fluorescence (554 nm) from ablating different spots on the target from one edge to the other. The results of this technique are shown in Figure 3.4(a), with a pulse energy of 144 mJ. The data point near 0 mm is an outlier, but we believe the reason this spot had particularly high neutral fluorescence is because it is near the most commonly used area of the target. As explained later in section 3.2.1, the area may be well conditioned already. A clear peak is seen, indicating that the

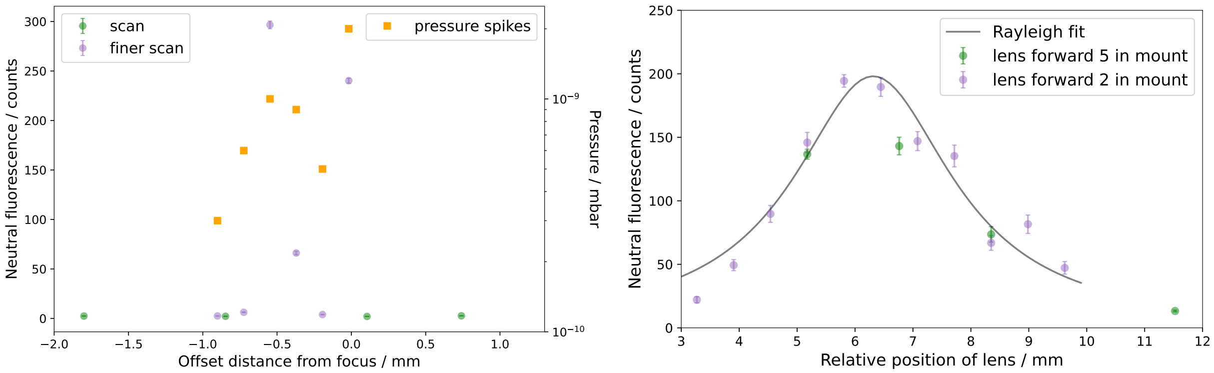

(a) (b)

Figure 3.4: (a) First ablation laser focusing method, which moves the beam across the target and uses the known geometry to estimate how much this changes the focus. A pulse energy of 140 µJ was used, with fluorescence being measured from 2.5 µs after the ablation pulse. (b) Second method for focusing the ablation laser, which involves moving the focusing lens and re-centering. Each data point has a sample size of 120 pulses.

focusing lens could be off by around 0.5 mm. The pressure spikes seen in the pressure gauge also correlate well with the neutral fluorescence and indicate the same peak position.

A lens tube setup with a lens is used for moving the focus; the lens can be moved forward and backwards by rotating the tube, changing the focus position. The distance traveled in the lens tube can be found using the pitch of the SM screws and how many turns we rotate the lens. A second method to focus onto the ablation target is to move this lens and just see much neutral fluorescence is measured from ablating with this focus. It was difficult to focus the beam exactly onto the target for a few reasons. There is variation in the neutral fluorescence signal coming from pulse energy fluctuations and individual spot variation from pulse to pulse. But the biggest variation comes from the fact that moving the focusing lens to a different position moves the ablation laser pointing slightly. We correct for this by re-centering back to the same spot for different focal lengths. This experiment is shown in Figure 3.4(b), using a pulse energy of 144 mJ. The results were consistent as long as we didn't have to change the way the lens was mounted in the lens tube (different orientations gave different ranges of travel). The final run, which is the green data-set in Figure 3.4(b) was consistent and an optimal position to put the lens for focusing on the trap center is clear. Fitting to the data with a fluence function based on the Rayleigh range,

$$f(z) = \frac{A}{\left(1 + \left(\frac{z - z_0}{z_R}\right)^2\right)} + BG, \tag{3.2}$$

gives the exact position to put the lens. Here, the fitting parameters are amplitude A, background BG, the focal position z_0, and the Rayleigh range z_R. In the end though, the acute angle of the laser to begin with means the focus changes for different spots quite significantly anyways, so it's not strictly necessary to get this perfect. However, it does help make more parts of the target have a sufficient focus for ablating and trapping.

After aligning the target, we were successful in ablating and measuring neutral fluorescence of atoms passing through the imaging system field of view, and could trap ions. In the time since then, we have used many different spots and areas of the target, which we keep track of (see Figure 3.5) so that we can go back to previous spots or know which spots are unused or could work well. Sometimes a spot or area works really well; we can produce and trap ions for thousands of pulses. Other times, a spot either never works or works for a small number of pulses. For more details on this, see section 3.2.1.

3.1.3 Ionization methods

Using laser ablation, charged ions can be generated and trapped directly in Paul traps [28, 29, 138, 142, 144, 145, 152], Penning traps [143, 153, 154], and has been used to generate multiply charged ions [155–158]. This method involves using a relatively large pulse energy on the ablation laser to generate more ions in the plume. The trap RF is initially off, so that ions are free to pass through the trap center without being deflected away. About 26 µs after the ablation laser hits the target, the trap RF is turned back on to catch the ions as they fly through the trap center. We have demonstrated this technique in our experiment to trap ions using a pulse fluence of around $0.32\,\mathrm{J\,cm^{-2}}$, and were able to achieve a loading rate of around 1 ion/pulse for $^{138}\mathrm{Ba}^{+}$.

Ions can also be generated by using electron-impact ionization [159–161] on the ablated neutral atoms, however this method is significantly less efficient than other methods [130, 162].

We prefer to use a technique called REMPI to generate ions for trapping because of its good loading rate, low contamination low and charge build-up in the vacuum chamber, and its ability to discriminate between different isotopes [129, 134, 164]. This method uses multiple lasers to sequentially ionize a neutral atom by first exciting a valence electron, then ejecting it completely. REMPI has been prevalent as a way of producing and trapping

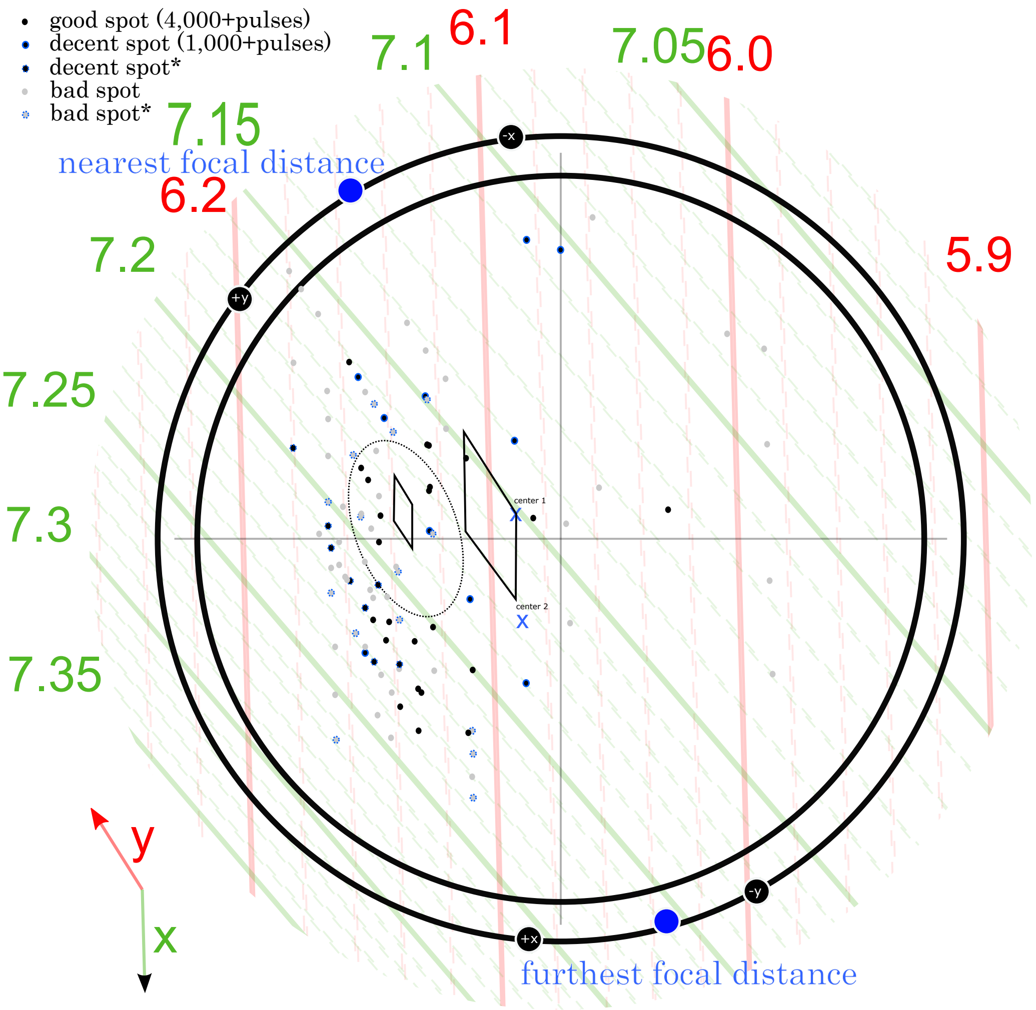

Figure 3.5: Map of our ablation target, with spots and areas we've used labeled. The units are in millimeters of the mirror stepper motors. The directions are not perpendicular because of the acute angle the ablation laser hits the target at. The two trapezoidal regions near the center were sweeps we did while ablating (see Appendix A). The circled area to the left is a spot which we completely used up by sending lots of very high pulse-energy pulses. "decent spot*" denotes a spot which gave really good neutral fluorescence but only for under 1,000 pulses. "bad spot" denotes spots which gave decent fluorescence but for under 1,000 pulses.

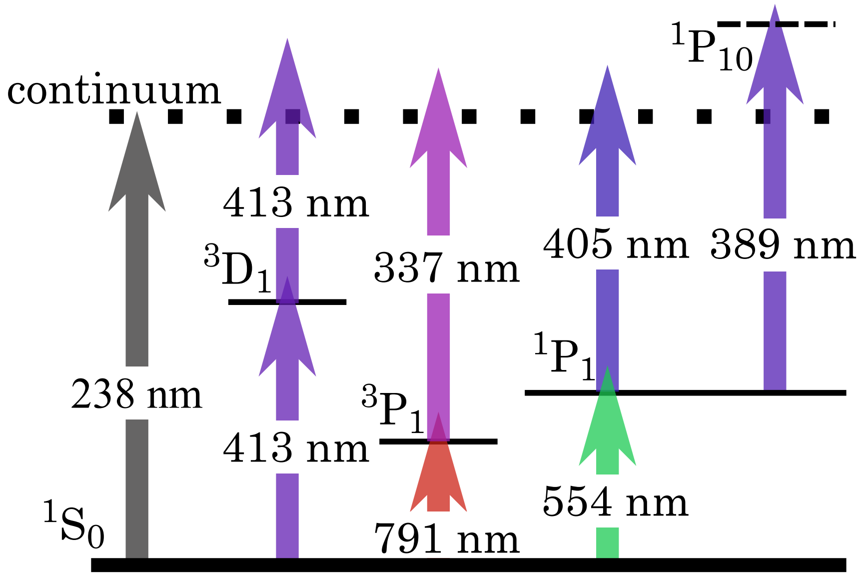

Figure 3.6: A laser with wavelength 238 nm laser or lower can ionize barium, or multiple steps can be used. A single 413 nm laser could be used to drive both steps. A 791 nm first step can be used with an ultraviolet 337 nm second step. Finally, a 554 nm laser can be used for the first step with either an ultraviolet laser of 417 nm or lower wavelength, or an auto-ionizing resonance [163] such as the one at 389 nm can be driven.

different ions, from calcium [130,136,139,165–168] and barium [27,30,40,131,132,146,164], to ytterbium [137,169,170] and other isotopes [129,134,171]. The first step of the process is a coherent transition in the neutral atom electronic energy structure, and different isotopes of the atom have slightly different frequencies. This makes the method isotope selective, meaning a specific isotope can be preferentially trapped by simply tuning the laser driving this transition to the appropriate frequency. In quantum information, this is particularly useful because of the need to deterministically load multiple of the same isotope at once. $^{137}\mathrm{Ba}^+$ has a very low natural abundance, so this method is crucial to be able to load it with a higher probability. The second step just has to have a high enough energy to kick the electron completely out into the continuum from the intermediate level, with a wavelength typically on the order of 400 nm or lower.

For barium, there are many options for performing this REMPI process with different sets of lasers [39] (see Figure 3.6). One transition commonly used for the first step is the 791 nm transition from the ground state to the $6s6p^3P_1$ excited state [27, 131, 132]. From this intermediate state, a laser with a wavelength at least under 340 nm is required

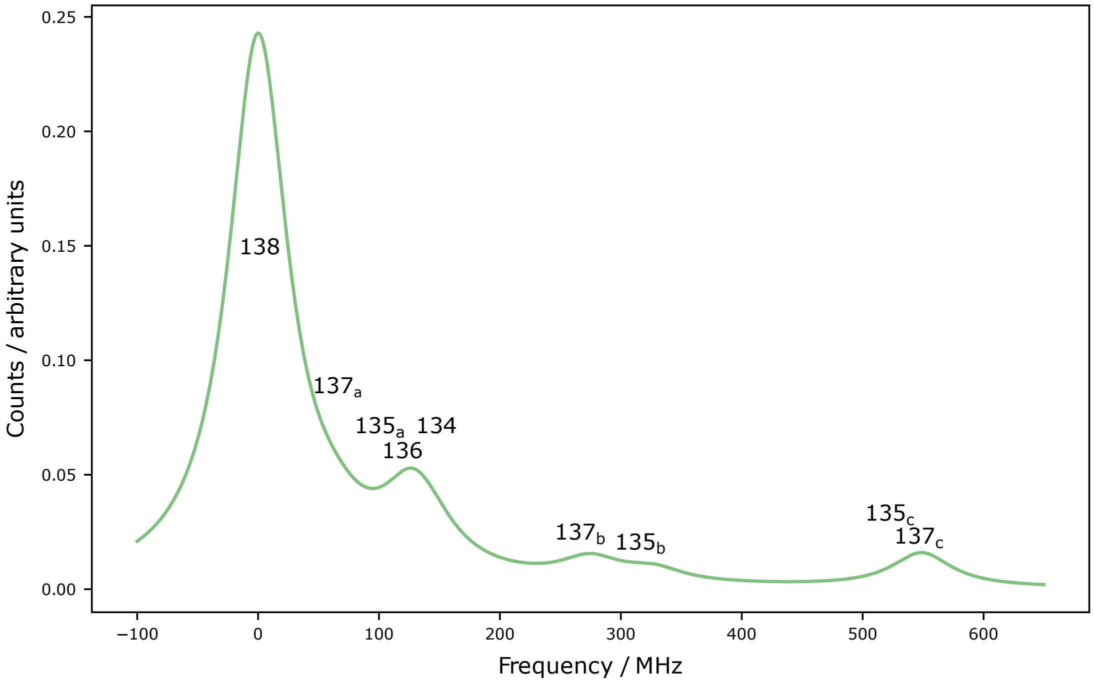

Figure 3.7: Theory curve [172–175] for the first-step photo-ionization laser 554 nm. Different isotopes are labeled, with subscripts a, b, and c denoting $F' \in \{5/2, 3/2, 1/2\}$ transitions in the isotopes with HF structure, ^{135}Ba and ^{137}Ba. To trap an isotope, set the laser frequency to its peak. Transition frequencies are listed in Table 3.1. The peak labeled 137_b is used for trapping $^{137}\mathrm{Ba}^+$ in our lab.

to ionize. The first transition ever used in barium, and the one used in this work, is the 554 nm transition [172–175] from the ground state to the $6s6p\,^1P_1$ excited state [30, 40, 146, 164] (see Figure 3.7 and Table 3.1). From this intermediate state, a laser with wavelength under 417 nm is required to ionize. We prefer this method because of its visible and nearly visible wavelengths, its low but sufficient differences in isotopic transitions, and its high ionization probability. For our second step, we use a cheap, readily available bare 405 nm laser with up to 4 mW of laser power at the trap. The lowest peak in the 554 nm spectrum is used for trapping $^{138}\mathrm{Ba}^+$, while the mostly isolated peak at 275 MHz is used for trapping $^{137}\mathrm{Ba}^+$.

It should be noted that there are also other methods, including the option to use a single laser at 413 nm to drive both a resonant transition into the excited state $6s6p\,^3D_1$ and the second step into the continuum [176]. In our lab, we recently demonstrated a

Isotope	Freq. (MHz)	Isotope	Freq. (MHz)
138	0	$137_b(3/2)$	274.56
$137_a(5/2)$	63.43	$135_b(3/2)$	323.44
$135_a(5/2)$	120.55	$135_c(1/2)$	547.3
134	142.8	$137_c(1/2)$	549.47

Table 3.1: Ionization transition frequencies of the first step ionization transition for different isotopes of barium using the 554 nm laser. The HF structure of the ^{135}Ba and ^{137}Ba isotopes give us three different transitions each [172–175]

method involving an auto-ionizing transition at 389 nm after the first 554 nm which has an order of magnitude higher ionization rate [163, 177].

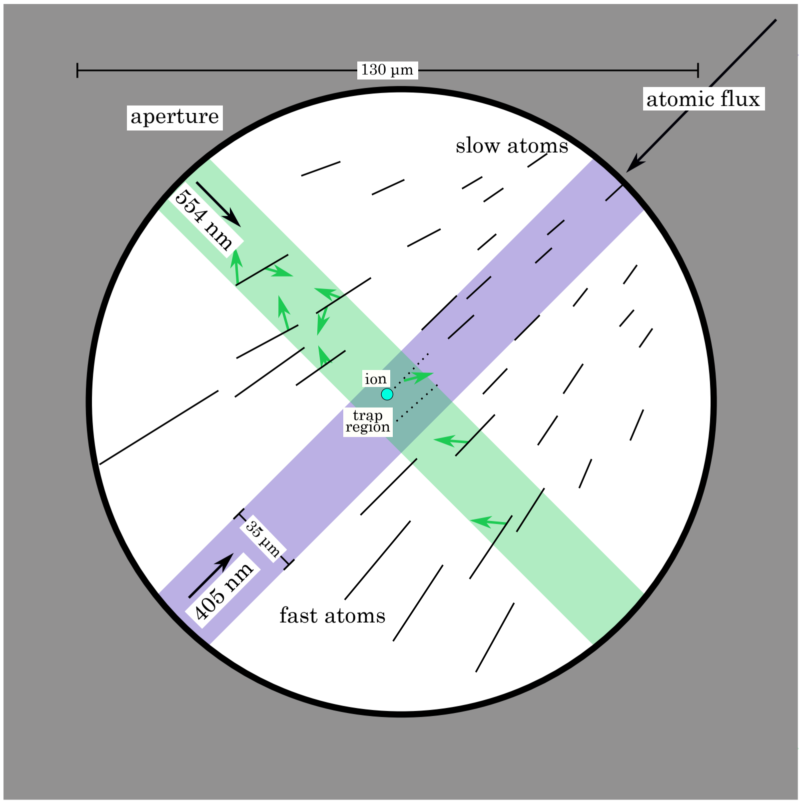

Figure 3.8: The ablation plume comes from the top right $BaCl_2$ target and goes through the trap center, where the two ionization beams are overlapping and transitions are driven. Lines are atoms, with longer lines being faster atoms (exagerated lengths and angles). Dotted lines denote atoms which can be ionized. The imaging system of this area has an aperture to limit the view to mostly the trap center.

3.2 Ablation

In our setup, we orient our first-step 554 nm laser perpendicular to the trappable ablation plume to minimize Doppler shift on this transition and maximize isotope selectivity. For the second step, we orient a 405 nm bare-diode laser perpendicular to the first-step laser. This limits the area of photo-ionization to be right at the trap center so that the ions generated will start off at the minimal trap potential. As shown in Figure 3.8, atoms will fluoresce from the 554 nm laser in the whole beam path, but will only fully ionize where this beam overlaps with the 405 nm laser at the trap center. Also shown are how the faster atoms arrive ahead of the slower more trappable atoms. If a neutral atom is excited by the 554 nm laser then subsequently ionized by the 405 nm laser, then the produced ion will experience the trap RF electromagnetic fields and be confined, if it has a sufficiently low energy.

In our imaging system, we have an aperture which limits the spacial collection region to 300 µm near the ion trap center (see Figure 3.8). This allows us to collect fluorescence mostly from only neutral atoms which have a wavevector mostly in the direction perpendicular to the laser, reducing Doppler shift of our neutral fluorescence measurements. It also allows us to have a better SN ratio in both neutral fluorescence experiments and all measurements of trapped ions. Laser powers are set to on the order of 100-200x saturation of their respective transitions they drive in neutral and ionized barium. For the 554 nm laser, this is 3 µW to 100 µW, depending on the experiment. The cooling 493 nm laser is at 40 µW power, and the repump 650 nm laser power is 300 µW. The laser frequencies are set to the resonance frequencies of the neutral isotope ^{138}Ba for the 554 nm transition and the ionized isotope $^{138}\mathrm{Ba}^{+}$ resonance frequencies for the 493 nm and 650 nm transitions. For all results here, we use laser fluences well below 1 J/cm^2, or a pulse energy of 0.6 µJ. A magnetic field of 1.048 mT is generated using two magnetic field coils on the viewports that the 405 nm laser passes through (top right and bottom left of Figure 2.9).

To characterize the ablation process, neutral fluorescence is quantified by collecting PMT counts in a 55 µs time window beginning 3 µs after the ablation laser pulse strikes the ablation target. As shown in Figure 3.13(a), this time window allows us to collect the majority of the observable neutral fluorescence signal. Often this collection window is set to start later, around 20 µs after the ablation pulse to reduce Doppler shift and to focus more on atoms which are slower and may be trapped. To look at different fluorescence signals, we use various light filters to focus on the wavelengths of interest for certain experiments. For neutral fluorescence experiments, we use a band-pass filter [178] which only allows 553 ± 17 nm light through to the imaging devices. To collect only ion fluorescence, we use a short-pass filter [179] which only allows wavelengths under 500 nm through. For normal operations, trapping ions and performing experiments with them, we wish to see the neutral fluorescence while we are ablating, but we obviously also need to see the ion once trapped, so we use a dual band-pass filter [180], which allows just 493 nm and 554 nm laser light through.

3.2.1 Ablation characterization

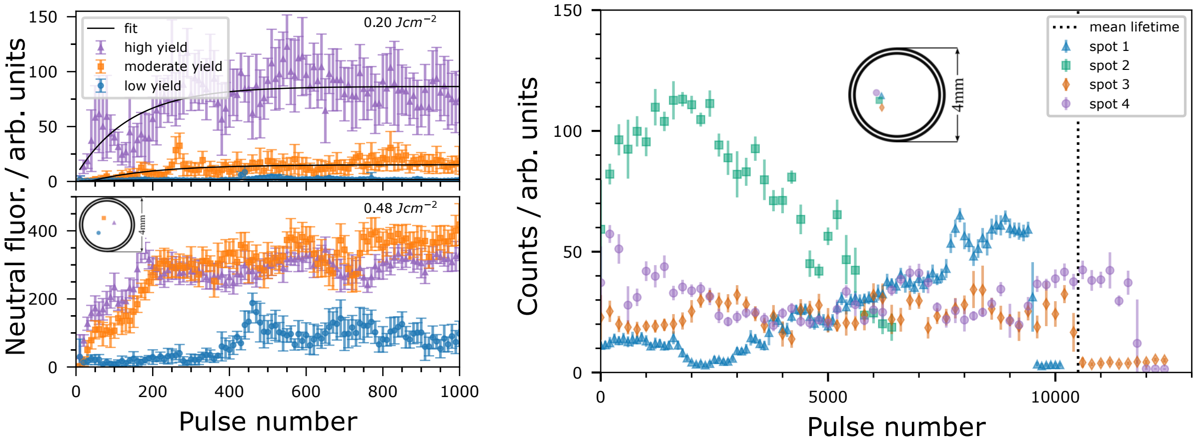

(a)

(b)

Figure 3.9: Ablation conditioning and lifetimes of spots. The first-step REMPI laser 554 nm power is $\sim 150 \times P_{sat}$. (a) A low ($0.20\,\mathrm{J/cm^2}$) and high ($0.48\,\mathrm{J/cm^2}$) fluence are used in the top and bottom graphs respectively. (b) Spot lifetimes of several example spots. Mean lifetime is averaged over 10 spots (not all shown).

On a completely fresh, never ablated before spot on the $BaCl_2$ target, no neutral atom fluorescence is observed using fluences below $0.3\,\mathrm{J/cm^2}$. However, if a higher fluence of 0.3 to $0.75\,\mathrm{J/cm^2}$ is used, neutral fluorescence can be observed on the order of 100 to 400 counts on the PMT. Returning to lower fluence again on this spot, often neutral fluorescence can be observed. We dub this process of using higher fluence pulses in order to activate a spot to be able to give neutral atoms which we can observe, using lower fluence, "conditioning". This process doesn't work all the time for all spots, and sometimes we don't even observe fluorescence using the higher conditioning fluence.

This process of conditioning a spot to work better at lower fluences has highly variable outcomes, with three common behaviors emerging as illustrated in Figure 3.9(a). In this experiment several fresh spots were ablated with alternating 10 conditioning pulses at $0.48\,\mathrm{J/cm^2}$ fluence and 10 low-fluence pulses at $0.20\,\mathrm{J/cm^2}$ fluence. Neutral fluorescence collected after each of these ablation pulses is shown in Figure 3.9(a), averaged over the 10 consecutive pulses. The top plot shows the neutral fluorescence from the low-fluence pulses and the bottom plot shows fluorescence from the conditioning pulses. Three spots are shown which exhibit that a fresh spot might be high-yield, with over 50 counts of neutral fluorescence, moderate-yield, with around 10-50 counts, and low-yield, with less than 10 counts. Overall, these three behaviors were observed 29%, 24%, and 47% of the time respectively [40,181]. Around half the time, a spot will not work at all, and the other half of the time it has an equal chance of giving moderate or high counts.

In separate experiments, we observed that without conditioning, a fresh spot with no neutral fluorescence will never exhibit neutral fluorescence even after many thousands of pulses: conditioning is necessary most of the time to activate a spot. We also found that spots towards the edges of the $BaCl_2$ target are much less likely to ever work, possibly because atoms ablated from here have a higher Doppler shift with respect to the laser.

Even for spots that do work, there is significant variation in the magnitude of ablated flux from pulse to pulse, and eventually the signal reduces down to negligible amounts. This spot lifetime is shown in Figure 3.9(b), using a fluence of $0.15\,\mathrm{J/cm^2}$ and a repetition rate of $2\,\mathrm{Hz}$ to ablate several different spots for thousands of pulses. The average spot lifetime was found to be $\sim 10,000$ pulses. We could sometimes revive a zombie spot by conditioning again, but typically this only gives it an extended lifetime of less than $2,000$ pulses.

These observations about varying neutral fluorescence signal could possibly be explained by the result that the majority of atomic flux produced from ablation is directed in the direction normal to the surface being ablated [147–149]. Because of this, if the surface profile of the spot being ablated is not well directed towards the trap center, the neutral fluorescence is expected to be lower. Conditioning a spot may be changing the surface profile, transforming it so that more of the surface points closer in the direction of the trap center. There is also the common belief that conditioning purges away some contaminants on the surface [29,135].

A common explanation for why a single spot's overall neutral fluorescence changes over time, tending to decrease until a spot dies, is some extreme pitting process. In this explanation, a severely angled laser (like our setup) digs into the target until the surface being ablated no longer has line-of-sight to the trap center [138,152,182]. This is unlikely, at least for our case. Looking at the target directly, we see no visible difference between used and unused areas of the target. Further, Reference [135] showed that in calcium metal targets, the depth of digging from ablation using a low fluence is negligible. We instead suspect this dying of a spot is due to a more subtle surface profile change; the surface is slowly shaped so that nearly none of it has a suitable pointing towards the trap center. Overall, the ablation process is quite tricky to characterize and come up with conclusive answers; these effects are as of yet an open mystery.

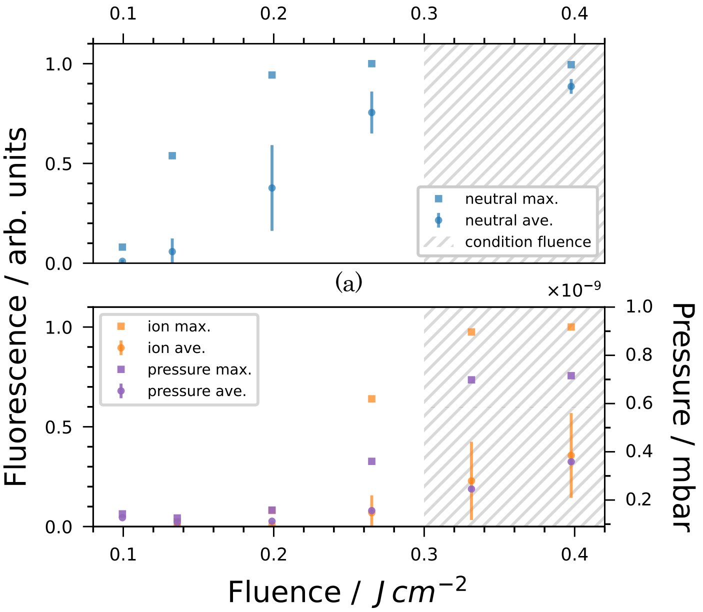

(b)

Figure 3.10: Fluorescence of atoms passing through the field-of-view of the imaging system for different ablation laser fluences. Diagonally hatched areas denote conditioning fluences. (a) Neutral fluorescence (554 nm). (b) Ion fluorescence (493 nm with 650 nm laser on) and pressure spikes read off the vacuum chamber pressure gauge.

When ablating using a pulse energy in the conditioning regime, both charged atoms and neutral atoms are produced. However, by conditioning a spot to be able to ablate using lower fluence, we can access a regime in which mostly neutral atoms are produced. For a conditioned spot, neutral atoms start to be generated with a fluence of above 0.1 J/cm^2 and ions start to be generated above 0.25 J/cm^2 (see Figure 3.10). This data was collected while the ablation laser was swept across a $300 \times 700\,\mu\text{m}^2$ area of the $BaCl_2$ target (see Appendix A for more details). Each area in the sweep is estimated to have been conditioned with about 100 pulses with fluence 0.50 J/cm^2. The mean, maximum, and standard deviation of the neutral fluorescence (top plot) and ion fluorescence (bottom plot), collected over two sweeps (around 120 pulses per sweep), are shown in Figure 3.10. Pressure spikes on the vacuum pressure gauge were also observed at high pulse energies and are shown in the bottom plot. There is quite a large variation in the fluorescence for different spots of the sweep, which is why the max data points differ so much from the average points. Neutral atom fluorescence plateaus very near the start of ion production, at $\sim 0.2\,\mathrm{J/cm^2}$ We also observe that ion production is well correlated with the vacuum chamber pressure spikes.

To avoid excess charge build-up on different parts of the vacuum chamber which displaces the ion and causes micromotion, it is desirable to ablate in the neutral-atom regime. For loading ions specifically, this is especially desirable so that we can build longer chains without disturbing already trapped ions. For this reason, we usually try to find spots which we can condition and activate for moderate- or high-yield with low fluences. Because of how random different spots behave, we have mostly moved away from sweeping the ablation laser.

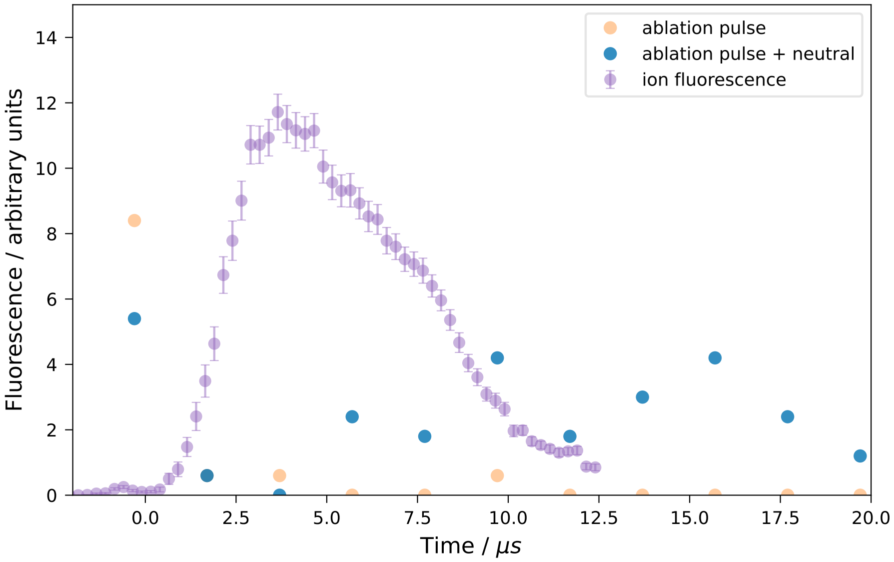

Figure 3.11: Ablation TOF experiments looking at the ablation laser light, ion- and neutral-fluorescence. The ablation pulse and neutral fluorescence cannot be disentangled because of the close wavelengths of the two lasers. A pulse energy of 114 µJ was used.

Ions were found to be much faster than neutral atoms, as illustrated from the TOF experiments shown in Figure 3.11. Light filters were put into the imaging system to isolate the different wavelengths of the 554 nm and 493 nm lasers. Because the ablation laser's wavelength of 532 nm is so near the neutral fluorescence laser, we were unable to isolate these two signals. The ion fluorescence peaks at 3 µs after the ablation pulse, indicating a velocity of 5.000 $\mathrm{m\,s^{-1}}$, while neutral fluorescence peaks at 10 µs to 20 µs after the ablation pulse, indicating a velocity of under 1.500 $\mathrm{m\,s^{-1}}$.

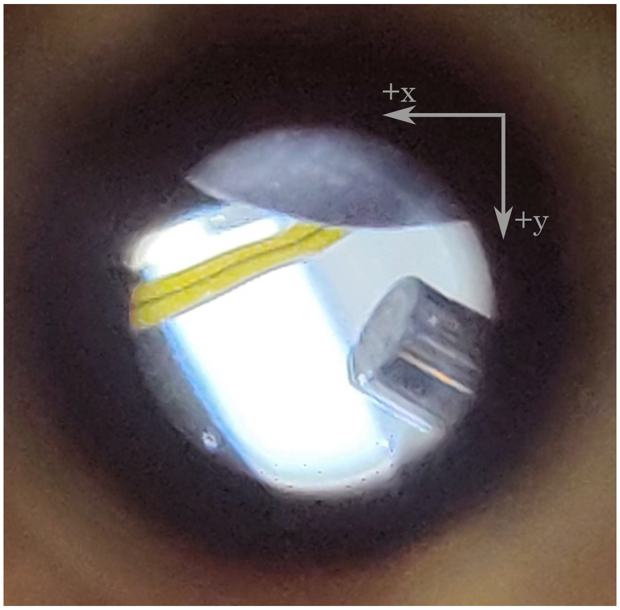

Figure 3.12: The angle in which the ablation laser focuses down and hits the target. The x and y directions of the stepper motor mirror are shown

Overall, the top and bottom of the ablation target have differing focal lengths (see Figure 3.12), with the overall focal length position changing by 3.5 mm. Assuming the center is where the beam is focused, this corresponds to the beam radius increasing to as much as 600 µm at the edges (beam waist 98 µm and Rayleigh range 5.7 µm). This could also be a big part of the explanation for the inconsistency we see when hitting different spots on the target.

The process of finding a new spot to use for trapping can be somewhat time consuming and frustrating, owing to the many unknowns in the ablation process. For a fresh spot on the target, using a low ablation laser fluence of around 0.15 $\mathrm{J/cm^2}$ to 0.3 $\mathrm{J/cm^2}$, usually no neutral fluorescence is observed. With a higher fluence of 0.3 $\mathrm{J/cm^2}$ to 0.75 $\mathrm{J/cm^2}$, we measure a significant amount of neutral fluorescence and see pressure spikes as high as 1×10^{-8} mbar (above a base pressure of 6×10^{-10} mbar). Sometimes these conditioning pulses succeed in activating a new spot to be able to give neutral fluorescence using a lower fluence. However, conditioning a spot does not at all guarantee a spot will work, as shown in Figure 3.9(a). In practice, varying amounts of conditioning pulses are needed, and overall we successfully prepare around 40% of fresh spots. The procedure for finding a new spot is as follows:

1. Move the ablation laser to a fresh spot on the target (see Figure 3.5).
2. Ablate using low fluence to see if there is any neutral fluorescence.
3. If no fluorescence is seen (most likely), increase the pulse energy to the conditioning regime (see Figure 3.10) and ablate with around 10-20 pulses.
4. If no fluorescence is seen even during conditioning, keep pulsing with high fluence no more than around 100 times to try and get the spot to fluoresce.
5. If neutral fluorescence is successfully seen during conditioning, return to a low fluence and ablate again. Pulse tens of times, and if you start to see neutral fluorescence, keep pulsing to try and increase it further.
6. Repeat this process a few times. If the spot doesn't exhibit significant neutral fluorescence, move on to a new spot and repeat the process. New spots should be picked at least half a beam waist away from spots already tried.

Empirically, we have to try 1-5 different spots before finding a good spot with at least moderate yield [181].

Several characteristics of the neutral barium plume can be illuminated by performing a TOF spectrum experiment [40, 183], in which neutral-atom fluorescence is collected in 1 µs time bins for different first-step REMPI laser frequencies. As shown in Figure 3.13, we observe the Doppler shift of ablated atoms, can generate a first-step photoionization spectrum showing resolved isotope peaks, and can extract a velocity distribution to find the temperature of the atoms.

The time-resolved spectrum is shown in Figure 3.13(a), with each point the average of neutral fluorescence from five pulses. Each measurement is calibrated by a reference neutral-fluorescence measurement before and after it to control for the temporally varying signal. For these calibration steps, the laser frequency is set to the ^{138}Ba peak, and a 55 µs time window is used, starting at 2.5 µs after the ablation pulse to collect as large a signal as possible to calibrate with. The previous and subsequent calibration measurements are averaged and used to normalize the measurement in between.

Photons collected in time bins closer to the moment the laser pulse strikes the target are fluoresced from faster atoms, while the slower atoms' fluorescence signal shows up in

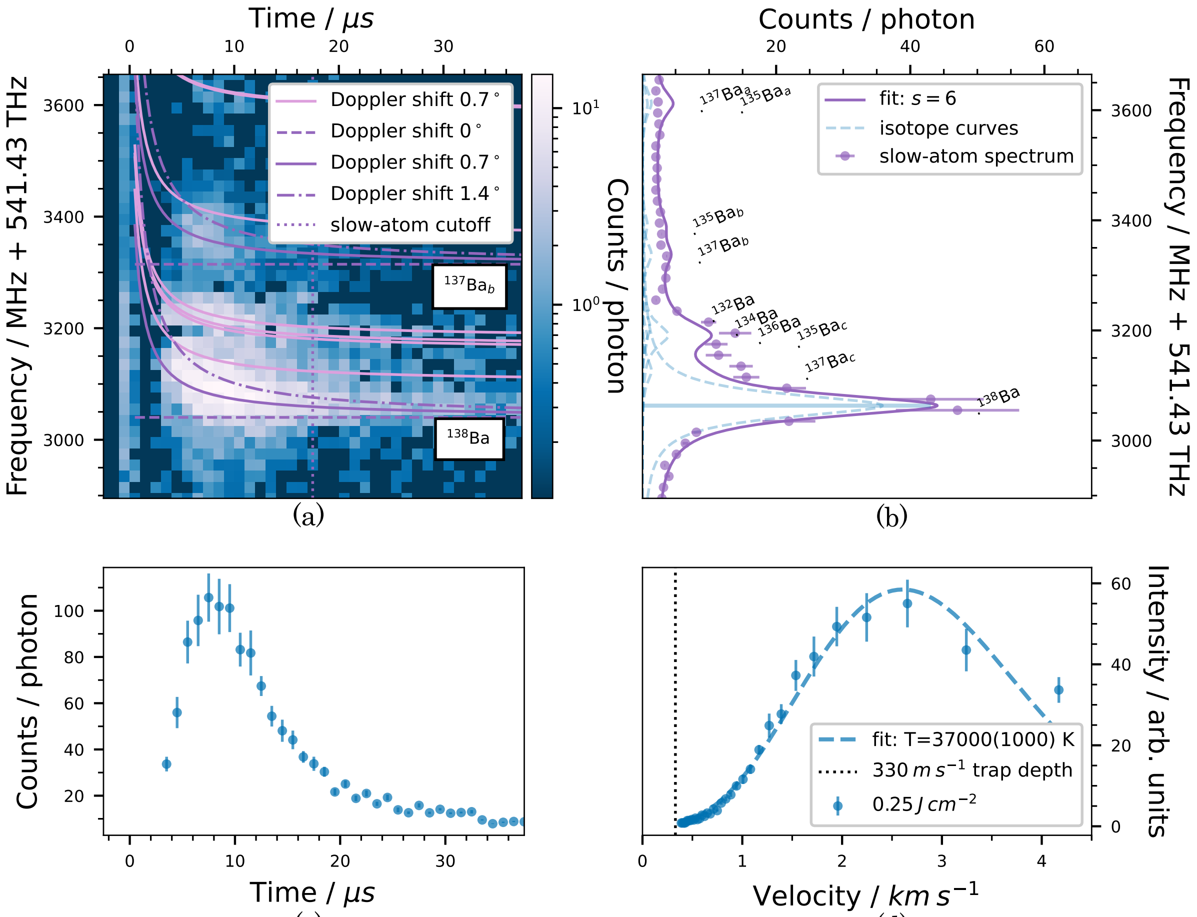

(a) (b)

(c) (d)

Figure 3.13: Ablation TOF spectrum. The first-step REMPI laser power is $12 \times P^g_{sat}$, the ablation fluence is 0.25 J/cm^2. (a) Neutral fluorescence collected from ablating the BaCl$_2$ target for different laser frequencies and time-windows after the ablation pulse. At ≥ 3315 MHz, a different data set is used because the first spot died. Doppler shifts expected for different angles 0° to 1.7° are shown (purple for ^{138}Ba and ^{137}Ba, pink for others). The dotted-purple line denotes the boundary for slow atoms used to generate (b). (b) First-step photoionization spectrum, calculated from integrating over times in (a) after the slow-atom cutoff [164, 172, 173]. (c) TOF distribution obtained by integrating over all frequencies in (a). (d) Velocity distribution calculated by scaling the TOF data in (c) appropriately as described in the text and converting to velocity. The dotted line indicates the estimated highest velocity ion that can be trapped (see Appendix B).

the later times. Only slow atoms with a lower kinetic energy than the trap depth are able to be confined in the Paul trap, with an estimated maximum energy calculated in Appendix B. To reduce Doppler shift and get a representative spectrum that tells us about how well we can selectively load different isotopes, we integrate the time-resolved spectrum over the times for the slower atoms (after the slow-atom cutoff), shown in Figure 3.13(b). Most of the isotopes' peaks are distinguishable, including the well-isolated $^{137}\mathrm{Ba}(j' = 3/2)$ peak we use to trap it. A fit is done using the known theoretical-transition frequencies and transition strengths of different barium isotopes [172–174] and the isotopic abundances. Each transition has a natural linewidth given by the lifetime of the excited state, which is $\Delta\nu_0 = \frac{1}{2\pi 8.4\,\mathrm{ns}} = 19\,\mathrm{MHz}$, and a saturation broadened linewidth given by $\Delta\nu = \Delta\nu_0\sqrt{1+s}$, where $s = P/P^g_{sat}$ is the saturation parameter and P is the laser power. In our fit, each peak is modeled as a Lorenzian with a linewidth $\Delta\nu$, centered about where its theoretical frequency is (with respect to the $^{138}\mathrm{Ba}$ transition), and with an amplitude scaling based on its abundance p_i and transition strength A_i:

$$x = \sum_i \frac{p_i A_i}{1 + \sqrt{\Delta\nu}}, \tag{3.3}$$

summing over all of the peaks i.

If we instead integrate over all of the frequencies, we can produce the time-resolved TOF spectrum shown in Figure 3.13(c), which tells us the distribution of times atoms are arriving. We can use the fixed distance from the ablation target to the trap center, $d = 14.6\,\mathrm{mm}$ to find how fast these atoms are traveling, $v = d/\tau$. To account for the transit time of atoms through the laser (faster atoms produce less neutral fluorescence because they pass through more quickly), we must scale the data by $1/\tau$, where τ is the time after the ablation pulse. The result is the velocity distribution in Figure 3.13(d). A Maxwell-Boltzmann (MB) distribution,

$$f_v(\tau) = \frac{A}{\tau} e^{-\frac{md^2}{2\tau^2 k_b T}}, \tag{3.4}$$

is fit to this data, and a plume temperature of $37,000(1,000)$ K and a peak velocity of $2,600(50)\ \mathrm{m\,s^{-1}}$ is estimated. Here, A is an amplitude-scaling parameter, v is atom velocity, m is the average mass of natural-abundance barium, and k_B is the Boltzmann constant.

Most other groups have measured a neutral atom ablation plume temperature of $1,000$ to $10,000$ K [137, 139, 183], but some have measured similar temperatures as us [183, 184]. Our barium-salt target could be exhibiting different plume dynamics, or the discrepancy may partly be explained by a difference in experiments. If the first-step photoionization laser were perfectly perpendicular to the ablation plume, there would be no

Doppler shift and one would expect the laser frequency to have a global influence on the brightness in the time-resolved spectroscopy data. However, because the two vectors are off from perpendicular, high-velocity atoms see the laser frequency Doppler shifted, depending on the angles θ and the speeds $v = d/\tau$ of the atoms:

$$f_{ob} = f_s \left(1 + \frac{d \sin\theta}{c\tau}\right), \tag{3.5}$$

where f_s is the laser frequency and c is the speed of light. We use this with Equation 3.4 to build a two-dimensional model of Figure 3.13(a) and (b). The Doppler shifts resulting from this fit are shown as the black and green curves in Figure 3.13(a), with a resulting fit angle of $\theta = 0.7°$. For this data set, we estimate the specific spots on the ablation target were $\sim 200\,\mu$m from the target center. From the geometry of our target and the trap center positions, and assuming the laser is well aligned through the viewport, this angle should be $\sim 1°$, which is very near the fit result of 0.7°.

Figure 3.13(a) gives a clue as to what could be causing us to see higher plume temperatures than other groups. In order to take into account Doppler shift, a time-resolved distribution should be collected over a spectrum, as done in this paper and Reference [183]. If the distribution is only collected for one frequency, as is most commonly done [137,139], and Doppler shift is present, then essentially only the slower, un-Doppler shifted atoms are being sampled. The velocity distribution will appear to give a lower temperature.

3.2.2 Ablation loading barium ions

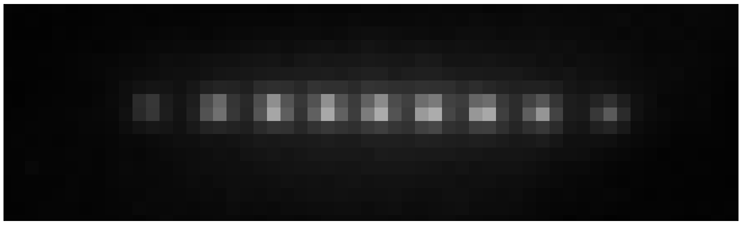

Figure 3.14: Image of a chain of nine trapped ^{138}Ba^{+} ions. Each pixel is 2 µm in the ion plane.

Once a neutral atom has been ablated and subsequently ionized by our REMPI process, it sees our trap electromagnetic field. If the energy of this ion is low enough, it can be completely confined in our ion trap, where it is Doppler cooled by our fluorescence

493 nm and 650 nm lasers. Once it has been cooled sufficiently, it crystallizes into a highly localized point less than 5 µm at the trap center. It continues to fluoresce from the cooling lasers, and some of that fluorescence is captured by our imaging system. If we look at how many PMT count are being collected or look at the image on the CCD, we can actually see how many ions are trapped (see Figure 3.14).

To load a specific isotope, we set the 554 nm wavelength to one of the peaks in Figure 3.13(b). We define the loading rate as the average number of ions trapped for each ablation pulse. The loading rate of that specific isotope should be proportional to the relative abundance of that isotope (see Table 2.1), with ^{138}Ba$^+$ having the highest loading rate.

Using a first-step REMPI laser saturation of $s = 150$, the loading rate for ^{138}Ba$^+$ is typically found to be very close to 1 ions/pulse (out of 33 pulses, see Figure 3.15). Using the same parameters, the ^{137}Ba$^+$ loading rate is measured to be 0.1 ions/pulse (out of 53 pulses), which is very close to the expected loading rate based on comparing isotopic abundances and transition strengths between the two isotopes. With this loading rate, it typically takes on the order of 10 pulses to load ^{137}Ba$^+$, and so we often use up to 10 pulses at a time before checking if we've trapped, just to speed things up. For the most part, this ratio holds true unless there is something wrong with the way we are cooling ^{137}Ba$^+$.

Because of it's more complicated energy space, with a nuclear spin and HF structure, it is more difficult to cool ^{137}Ba$^+$. In order to drive both ground state HF levels and all four $D_{3/2}$ HF states for cooling and fluorescent readout, EOM's are used to split the laser power into many different frequencies, reducing the laser power used to drive each transition. Overall, we see that ^{137}Ba$^+$ is on the order of a third the brightness of ^{138}Ba$^+$. Because of this, even if we successfully load ^{137}Ba$^+$, we don't always know that we did because it takes much longer for it to cool down and crystallize. In addition, it could be that there is some effect of the cooling lasers helping with trapping hotter ions which would be too hot to trap without the cooling. If this is the case, ^{138}Ba$^+$ would gain the most from this effect.

A dual-band-pass filter is used in our imaging system, allowing for measurement of both neutral-atom fluorescence during ablation, and ion fluorescence of trapped ions. This lets us compare the loading rate directly with the neutral fluorescence measured for that loading attempt. Figures 3.15 and 3.16 show the loading of ^{138}Ba$^+$ with laser saturations of $s = 150$ and $s = 15$ respectively. The loading rate of 0.59 ions/pulse using a lower ionization laser power is marginally lower because both experiments are using laser powers well above saturation, resulting in a diminishing increase in transitions being driven.

From these experiments, we can also see that the neutral fluorescence seems to be well correlated with the number of ions being trapped. These experiments were done measuring

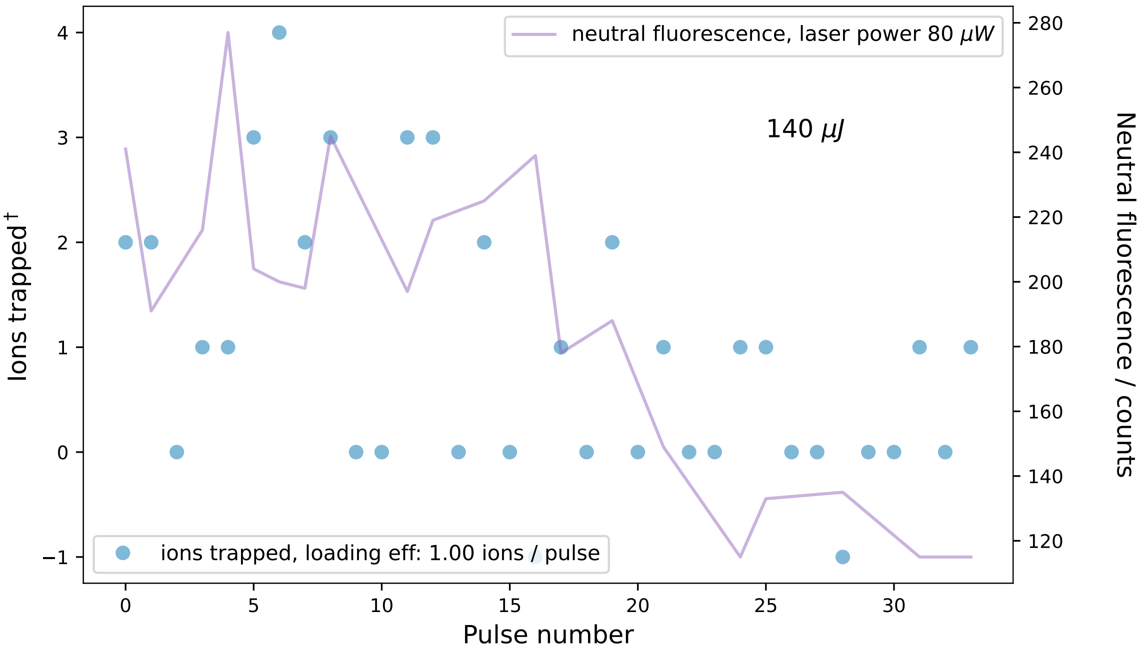

Figure 3.15: The loading efficiency for high ionization laser power 80 µW, or $s = 150$. The number of ions loaded for each pulse is shown. Neutral fluorescence is also shown in the axis on the right. A pulse fluence of 0.23 J/cm^2 is used. †A value of −1 indicates some number of other isotopes were loaded.

all of the neutral fluorescence, with a window starting at 2.5 µs after the ablation pulse. However, if we want a more closely correlated signal, we should delay the start time for the PMT collection window to measure fluorescence from more trappable slow atoms (see Figure 3.13). This would result in less signal from Doppler shifted atoms of other isotopes. We observe that the neutral-fluorescence signal of slow atoms, measured after the slow-atom cutoff in figure 3.13(a), is also well correlated with the loading rate. This means that we can use the neutral fluorescence to on-the-fly monitor what our expected loading rate is without having to perform statistical loading experiments. It's a good signal to watch to be sure that our ablation loading should be working.

Figure 3.17 shows what this correlation looks like over the course of many months. Each data point is a different day, with mostly different parameters. Even with changing parameters, the loading rate is still very well correlated with the neutral fluorescence measurement. For more details on the specifics of each day, see Appendix C.3. The correlation of loading rate to neutral fluorescence measurement seems to also hold up for

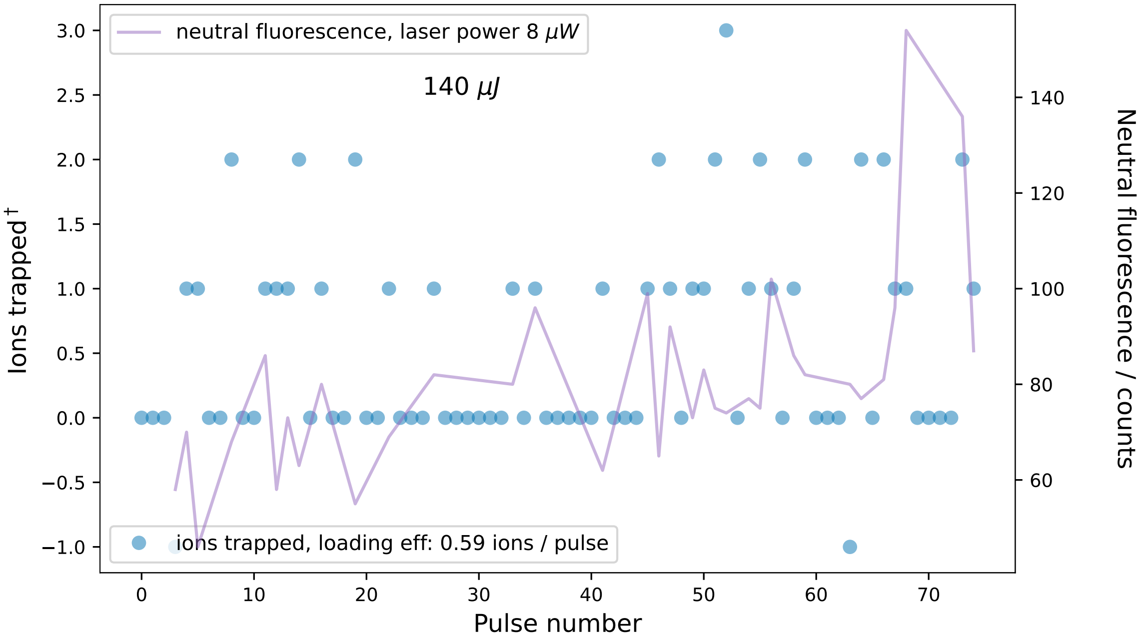

Figure 3.16: The loading efficiency for high ionization laser power 8 µW, or $s = 15$. The number of ions loaded for each pulse is shown. Neutral fluorescence is also shown in the axis on the right. A pulse fluence of 0.23 J/cm^2 is used. †A value of −1 indicates some number of other isotopes were loaded.

trapping ^{137}Ba$^+$.

Early on, and during all of these ablation characterization experiments, we calibrated the wavelength of the 554 nm laser to the first-step photoionization ^{138}Ba peak. We would perform a frequency scan of this laser while collecting slow-atom neutral fluorescence (with the collection window starting 17 µs after the ablation pulse, with a 55 µs width). This calibration helped to alleviate slow drifts in the measured peak frequency. Because of Doppler shift, the peak found using this method can be up to 10 MHz from the actual peak. However, we soon found that these drifts were mostly due to our wavelength meter [124] cavity drifting. We use this wavemeter to lock the laser, so the cavity drifting translated to the 554 nm laser frequency being sent to the trap drifting. We now use a stable HeNe laser to calibrate the wavelength meter and keep its measured frequencies from drifting from the actual frequencies; we no longer need to perform 554 nm laser frequency scans.

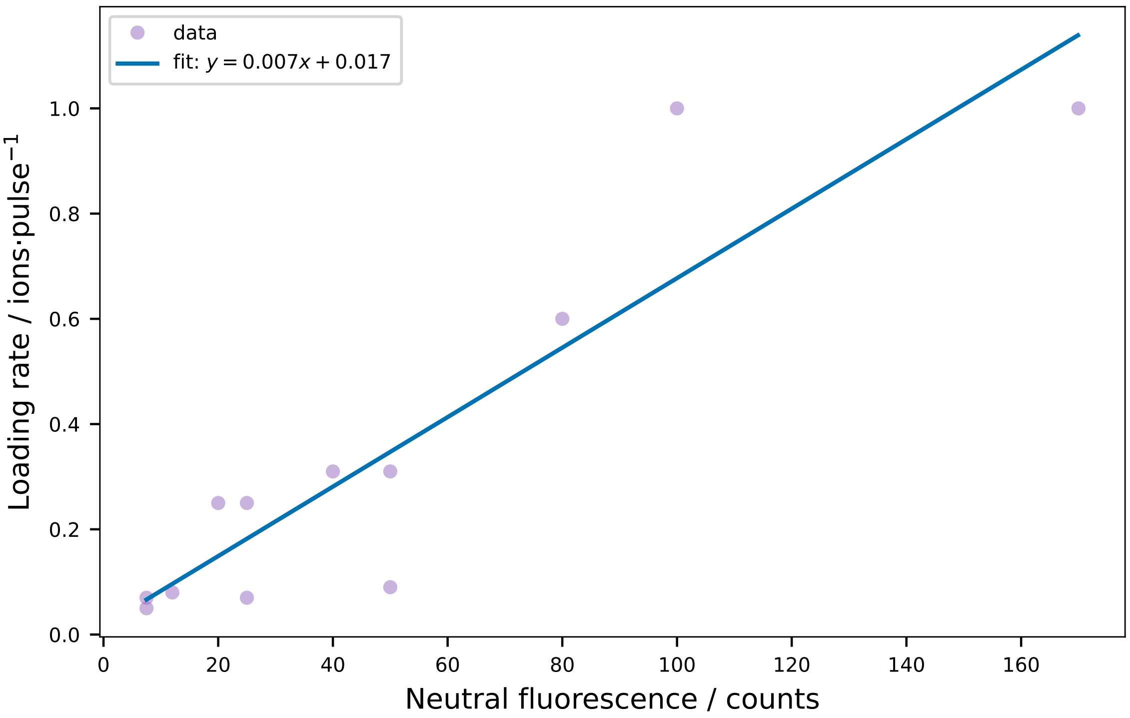

Figure 3.17: Loading rate vs neutral fluorescence counts for loading $^{138}\mathrm{Ba}^{+}$ on different days over the course of months. For details on each data point, see the appendix, Section C.2.

3.2.3 Selectivity of barium loading

With our REMPI technique of ionizing neutral atoms, we can in principle trap a specific isotope of barium with a better probability than what we expect from the natural abundances (see Table 2.1). However, because the lineshapes of the different isotopes have linewidths Δ_ν given by Equation 3.3, their lineshapes overlap one another and reduce our ability to discriminate on different isotopes. The linewidths of these transitions depends on the power of the 554 nm laser, with higher powers saturation broadening the transitions. Therefore, we should be able to improve our selectivity by reducing this laser power, ideally towards saturation P_{sat}^{g} or lower. As we decrease this laser power, the linewidth of the transitions should approach the natural linewidth of the transition, which would be the limit of our selectivity, around 95% for $^{137}\mathrm{Ba}^{+}$.

To quantify the ability to selectively choose isotopes to load, we define the selectivity,

p_{sel}, as the percentage probability of loading an isotope. Next, we define p_{nat} as the natural selectivity, which is just the natural abundance of an isotope (see Table 2.1). We further define the selectivity enhancement as

$$\varepsilon_{sel} = \ln\left(\frac{p_{sel}}{1-p_{sel}}\right) - \ln\left(\frac{p_{nat}}{1-p_{nat}}\right). \tag{3.6}$$

Here, each natural log is the logit function ($logit(p) = \ln(p/(p-1))$), which is useful for quantifying odds. This selectivity enhancement measure compares an achieved selectivity to the selectivity for a unbiased loading method, which traps according to an isotopes' p_{nat}. In this measure, a selectivity enhancement of zero corresponds to being not selective at all, with a probability of loading an isotope the same as its p_{nat}. A selectivity enhancement of near one is a roughly halving of the number of unwanted other isotopes trapped.

In our experiment, we have the ability to fluoresce all naturally-abundant isotopes of barium except for ^{135}Ba$^+$. Crucially, this isotope is the most disruptive one for our ^{137}Ba$^+$ selectivity, since it has a peak within 50 MHz of the transition we use to trap ^{137}Ba$^+$. Because of this, we are likely to trap this isotope quite often. In order to measure the percent of desired ions loaded, considering all trapped atomic or molecular ions (including ^{135}Ba$^+$), we instead look at chains of ions. For each experiment, a chain with at least 3 ^{137}Ba$^+$ are trapped and the number of bright ^{137}Ba$^+$ ions is compared to the number of dark ions (see Reference [40, 121]).

In Figure 3.18, the expected theoretical selectivities for ^{138}Ba$^+$ and ^{137}Ba$^+$ are shown as a function of the first-step REMPI laser frequency. These curves are given for different saturations of the 554 nm transition (i.e. different transition linewidths). The selectivities we actually measured from loading chains of ions are also shown, with ^{138}Ba$^+$ having a selectivity of $85\pm3\%$, or selectivity enhancement factor of $\varepsilon = 0.8$, which means the amount of other isotopes loaded nearly halved. For ^{137}Ba$^+$ the best selectivity we measured was $37\pm5\%$, an enhancement of $\varepsilon = 1.5$. The ^{137}Ba$^+$ selectivity enhancement factor increased from $\varepsilon = 1.3$ to $\varepsilon = 1.5$ by lowering the transition linewidth (using lower power). In most of these cases, the achieved selectivity is lower than the theoretical. In particular, there seems to be a discrepancy in the ^{137}Ba$^+$ theoretical probabilities compared to the measured probabilities for different linewidths. It could be that the saturation model we are using is not working well for our ablation plume. Since neutral atoms fly through the laser quickly, the overall transitions being driven might not be saturated as we assume. We also saw this in the saturation parameter fit in Figure 3.13(b), where the fit gave a saturation half of what we expected.

Overall, we were unable to achieve the expected selectivity for ^{137}Ba$^+$. One mechanism that may be affecting selectivity for this isotope is charge-exchange [165–167, 185]. When

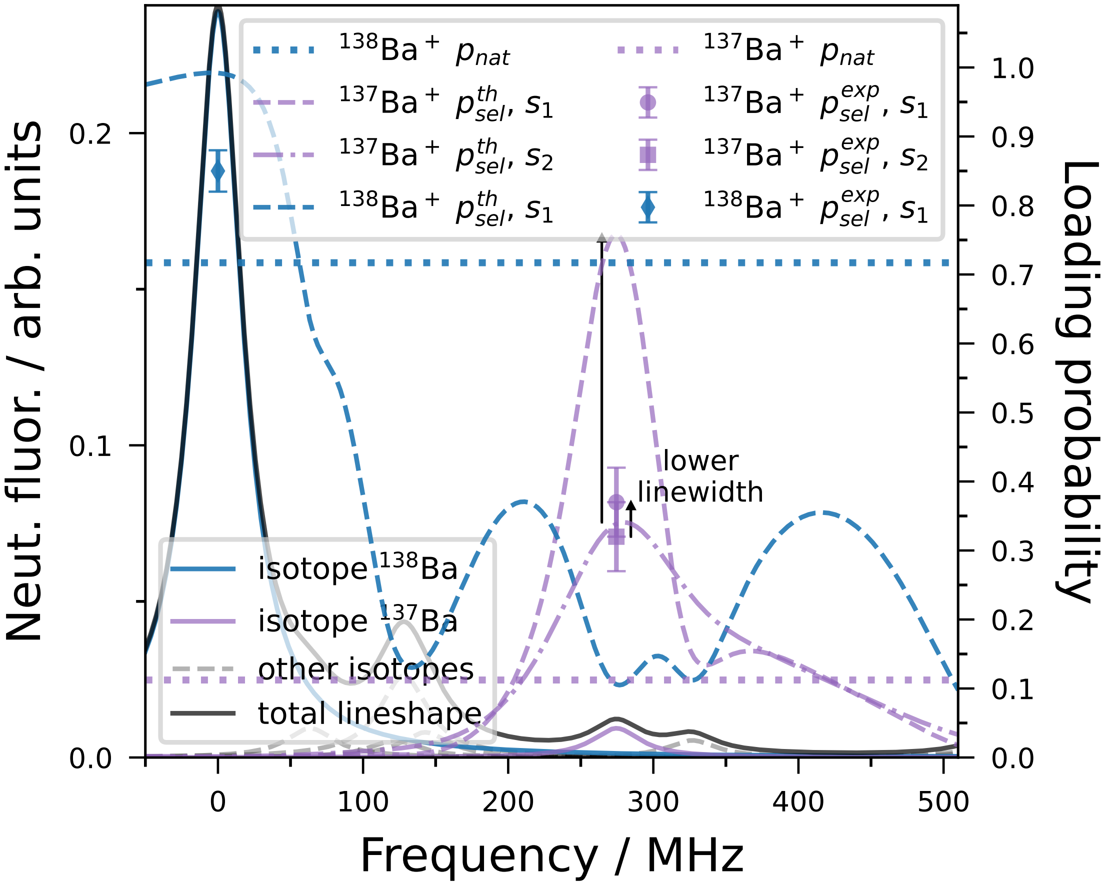

Figure 3.18: Selectivity of loading ^{138}Ba$^+$ and ^{137}Ba$^+$. The theoretical loading probabilities for isotopes of barium using two-step photoionization, p_{sel}^{th}, are calculated by comparing their Lorentzian curves with the total lineshape from all transitions. Experimentally measured selectivities p_{sel}^{exp} are shown as points. s_1 and s_2 denote 4x and 36x saturations of the 554 nm laser respectively.

trying to trap more ions in an already loaded chain, a trapped ^{137}Ba$^+$ ion can experience an electron-transfer collision

$$^{137}\text{Ba}^+ +^{138}\text{Ba} \rightarrow^{137}\text{Ba} +^{138}\text{Ba}^+, \tag{3.7}$$

where a passing neutral atom can donate its electron to the ^{137}Ba$^+$, making the ^{138}Ba turn into a trapped ion while the ^{137}Ba$^+$ ion turns back into an un-trapped neutral atom. By this process, we can end up with an imposter ion in our chain which was supposed to be selectively loaded $^{137}\mathrm{Ba}^{+}$. Because of its relatively-large abundance, this charge-exchange is likely to result in more $^{138}\mathrm{Ba}^{+}$ imposters trapped, reducing the selectivity of other isotopes, in particular, $^{137}\mathrm{Ba}^{+}$. Mortensen et. al. [185] demonstrated this effect strikingly, using it to swap out most of a large crystal of $^{44}\mathrm{Ca}^{+}$ ions with the much more abundant $^{40}\mathrm{Ca}^{+}$ isotope.

Another interesting observation is that our selectivity enhancement for $^{138}\mathrm{Ba}^{+}$ was lower than for $^{137}\mathrm{Ba}^{+}$; $^{138}\mathrm{Ba}^{+}$ was less selective. During selective trapping of $^{138}\mathrm{Ba}^{+}$, the Doppler cooling lasers are also able to cool the other unwanted even isotopes because their transitions are blue detuned from $^{138}\mathrm{Ba}^{+}$'s cooling frequencies This could allow these isotopes to be accidentally trapped more easily, causing a reduction in the selectivity enhancement for $^{138}\mathrm{Ba}^{+}$ compared to for $^{137}\mathrm{Ba}^{+}$.

One simple method of improving selectivity is to acquire an isotope-enriched target. This is great if you only need one specific isotope, but often more than one of the isotopes are used in an experiment. In addition, current techniques used to source the interesting barium isotope $^{133}\mathrm{Ba}$ have targets which leave equal amounts of $^{132}\mathrm{Ba}$ and $^{133}\mathrm{Ba}$. So to load longer chains of this isotope, trapping selectivity techniques are still necessary.

Finally, to improve on the photoionization method for selectively loading presented in this work, a different photoionization path could be employed. As discussed in Section 3.1.3, the first step of photionization exciting to the $6s6p\,^{3}\mathrm{P}_{1}$ state using a 791 nm laser could be used [27, 131, 132]. This scheme has larger isotope shifts, and has already been used to selectively load $^{137}\mathrm{Ba}^{+}$ ions [132]. Other methods have been employed to improve selectivity further by post-loading distillation [165, 166, 186–190]. These methods heat the unwanted isotope out of the trap by using either the cooling lasers to Doppler heat instead of cool [165, 166, 186–188], or by applying an additional RF on the trap electrodes, exciting the secular motion [189, 190] and shaking the ion out of the trap.

Chapter 4

Barium Qudit Measurement

In this chapter, the quadrupole transition from $S_{1/2} \leftrightarrow D_{5/2}$ is explored in detail, with many of the specific transitions found and characterized using Rabi oscillations and Ramsey sequences. Methods for faster calibration of the frequencies and π-times are explained, and a SPAM result of a 13-level qudit is presented.

First, background is presented on the quadrupole transition used in this chapter to shelve electrons in a metastable $D_{5/2}$ state. Details about the specific low-linewidth laser system we use and the optics we use to deliver it to the ion are given. Expectations about the different transitions using this laser are derived, with transition strengths depending on geometrical constraints and the frequencies of the transitions predicted for both isotopes $^{138}\mathrm{Ba}^+$ and $^{137}\mathrm{Ba}^+$.

In the latter half of the chapter, the results of driving this transition are presented. I describe how we were able to find all of the transitions, present the spectrum results and the details on what frequencies each of these transitions are found at. The expected frequencies derived previously match very well with the frequencies we measured, and nearly all of the transitions can be used for quantum information. Next, coherent quantum operations using these quadrupole transitions are explored, with Rabi oscillations and Ramsey sequence results presented for all transitions. Most transitions have a coherence time on the order of 400 µs. Methods for calibrating to all of the transition frequencies and π-times are given and the results are characterized. A frequency interpolation method successfully reduced the number of calibration steps from 14 to just 3. The π-time calibration works in principle to reduce the number of calibrations from 14 to 5, however this didn't work well in our setup because of device specific limitations.

Finally, the qudit SPAM results are presented. A 3-level qutrit and 6-level qudit were successfully measured in ^{138}Ba^{+}, and the fidelities of this operation are given. In ^{137}Ba^{+}, we were able to perform up to a 13-level qudit SPAM experiment, with a resulting fidelity of 91.7%. The SPAM error is shown to not depend on d, but rather the specific transitions we decide to use in our qudit.

4.1 Shelving transitions - background

4.1.1 1762 nm laser

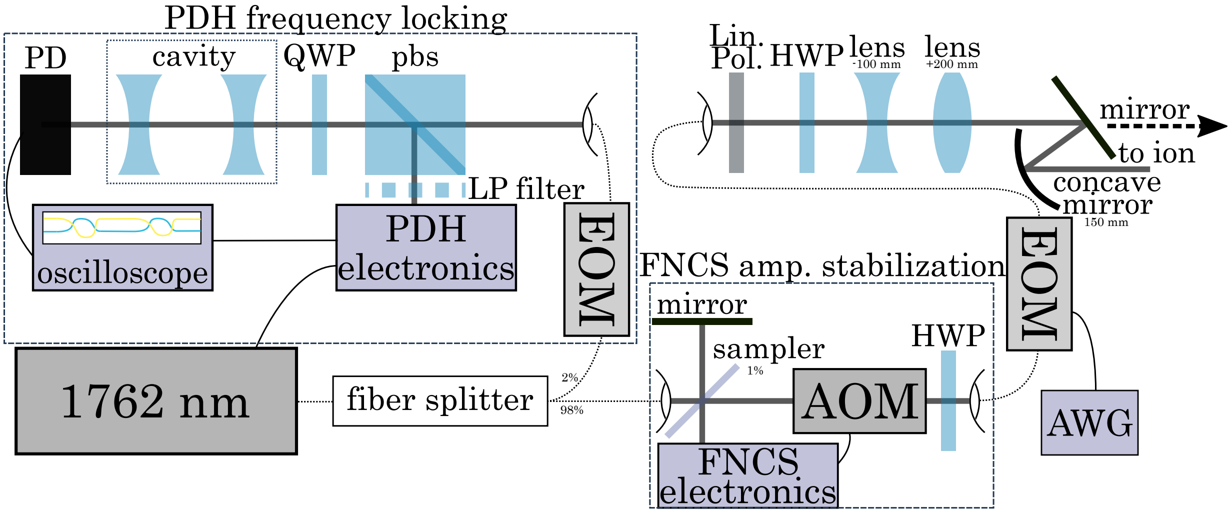

Figure 4.1: 1762 nm laser path. Low-pass (LP) is a low-pass frequency filter and PD is a photodiode. The top left box is the optics used for PDH locking and the bottom right box is the optics used for the fiber noise canceling system (FNCS). Two different EOM's are used, one in the PDH line for generating the sideband to lock to, and one on the right side for generating a controllable sideband we can use to drive transitions in barium.

The quadrupole transition $S_{1/2} \leftrightarrow D_{5/2}$ has a very narrow linewidth, with its 35 s lifetime [31] giving it a millihertz natural linewidth. With Doppler broadening and power broadening, it is found to be more like kilohertz linewidth, but this is still a difficult transition to address. A narrow-linewidth stabilized laser is needed to be able to address it, and we use a Stable Laser Systems [122] stabilized laser system to do this. This system also includes amplitude stabilization using an FNCS.

The SLS uses a standard ECDL laser [120] which is frequency stabilized using a stable temperature-controlled Fabry-Pérot cavity and a PDH sideband locking method to reduce the linewidth from hundreds of megahertz to on the order of hertz. The cavity is inside of a vacuum chamber which is pumped down to around 1.7×10^{-7} mbar, and the reflection of the cavity is used for generating the feedback for locking. The cavity drifts slowly, as shown in Figure 4.2. Over the course of months, the cavity consistently drifts by around $1.87\,\mathrm{kHz\,d^{-1}}$, which is likely due to relaxing optics inside the vacuum chamber. The PDH

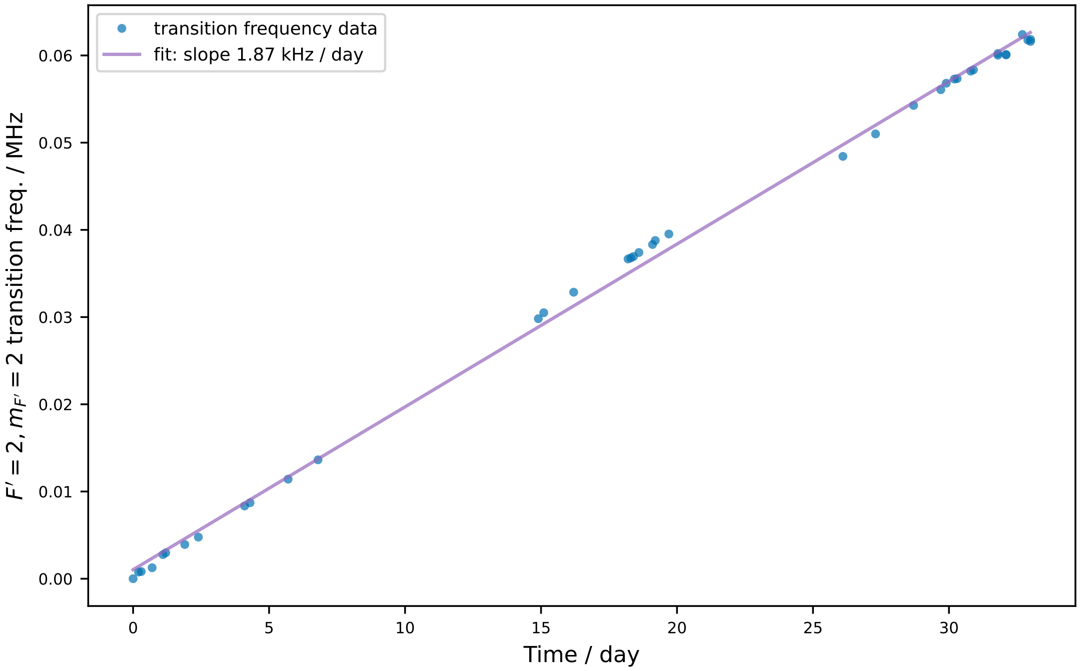

Figure 4.2: Drift of the PDH cavity used to lock the 1762 nm laser. The frequency of the least magnetic field sensitive transition ($|S_{1/2}, F = 2, m_F = 2\rangle \leftrightarrow |D_{5/2}, F' = 2, m_{F'} = 1\rangle$) drifts by $1.87\,\mathrm{kHz\,d^{-1}}$.

control does include an automatic drift adjustment, which can be used to track to this drift. The free spectral range of the cavity is around 1.4 GHz.

Approximately 2% of the 1762 nm laser is split off into the PDH system, where it's first sent through the PDH EOM. The PDH sideband is imparted by an EOM and its frequency can be varied up to 1 GHz. This is a frequency which is added to a 5 MHz RF signal used for extracting error signal, and it allows us to move the carrier frequency around much more freely while still staying locked. Either the red or blue sideband can be locked to, depending on the polarity chosen for the error signal. Sidebands can be easily found by applying a repeating scan on the piezo feedback of the 1762 nm laser and looking for the transmission peak from the sideband (see Figure 4.3), with the frequency response of the laser to piezo voltage being $\sim 140\,\mathrm{MHz\,V^{-1}}$. Blue sidebands have a lower frequency/voltage and red sidebands have a higher frequency/voltage in this graph because we move the laser carrier down in frequency/voltage so that the blue sideband can be transmitted through the cavity. Cavity peaks are separated by around 10 V. The correct sideband can be identified

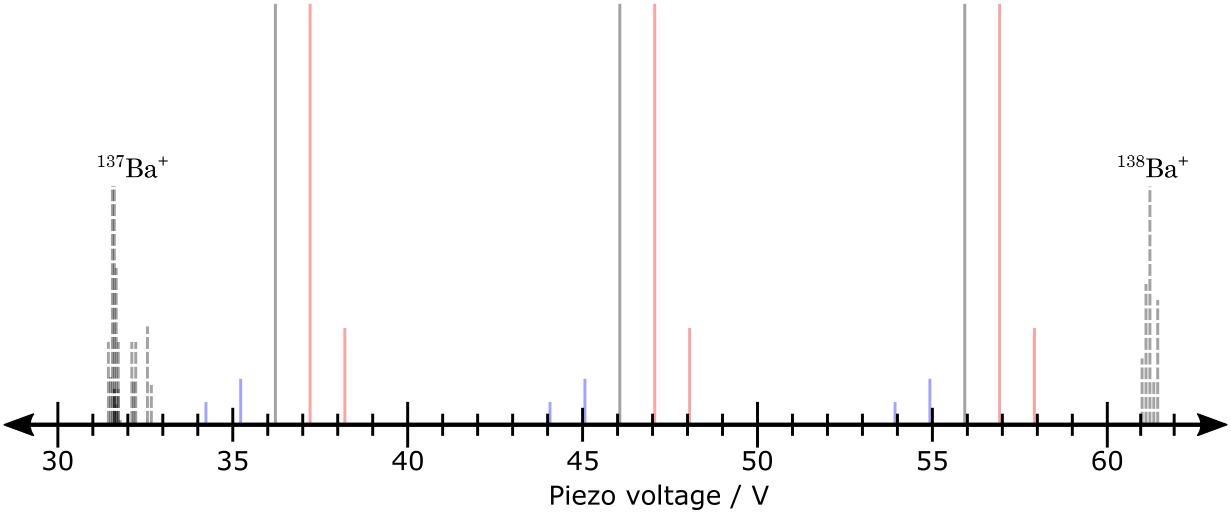

Figure 4.3: The SLS system PDH cavity's response to input 1762 nm laser frequency. Grey peaks are from the laser carrier frequency, blue and red peaks are from the frequencies imparted by the PDH EOM. The transitions of barium are shown in dashed lines, with their heights showing their relative empirical strengths as inferred from their Rabi frequencies presented in later sections.

if locking is on while changing the overall offset voltage of the laser; this is because the PDH lock partially succeeds during the parts of the scan that are close enough to the resonance frequency. If it's still not obvious, you can also change the PDH EOM frequency to see in which direction the peak moves (carrier peaks don't move). Some important parameters for locking to this peak are the RF amplitude (set as a percentage), and frequency. We found that around 140 MHz or higher is the easiest to lock to (around 1 V difference when scanning the piezo voltage). Fast locking is achieved with only current feedback, and locking while the laser frequency drifts slowly is done using feedback to the piezo input of the laser. Without piezo locking, the laser can stay locked for around 30 minutes as long as the optics table is undisturbed. This is because the frequency of the laser can drift around quite a lot, on the order of 70 MHz/min in extreme cases. With piezo locking turned on, the laser can stay locked for an indefinite amount of time if nobody is in the lab, but for on the order of days to weeks normally.

First the ECDL laser [120] is coupled into a fiber using a fiberdock. The fiber splits off part of the power (around 2%) for the PDH system. This picked off PDH light is sent through an EOM which imparts the sidebands which the PDH locks to. Next a PBS and QWP setup is used so that all of the incoming light goes straight to the cavity, but light coming from inside the cavity gets reflected by the PBS. This light is LP filtered and measured by a photodiode (PD) in the PDH electronics system. The system also has another PD to measure the light transmitted by the cavity, which is read off on an oscilloscope; this is helpful for locking the system. This comprises the whole PDH system which locks the laser frequency.

The majority of the laser light continues on into the FNCS. Collimated light is first passed through a sampler + mirror setup which picks off some of the light and sends it into the FNCS electronics. Most of the light continues on through an AOM with an RF frequency of 80 MHz. After that, it passes through a HWP before being coupled back into fiber. This fiber is then passed through an EOM, with RF coming from an AWG, and collimated into free space again. Light reflected back from the end of the fiber (just before delivery optics) collimates back out of this coupler and passes back through the HWP and AOM from the opposite direction. Again some of this light is sampled back into the FNCS electronics. Comparing this returning signal to the input signal, the FNCS can correct for any amplitude fluctuations in the fiber optics path. The AOM used in this path also has an RF switch so that we can use it as an optical switch to quickly turn the 1762 nm laser on or off. Before being focused down onto the ion, the final beam passes through a linear polarizer and HWP to control its polarization. It is then telescoped up to a bigger beam size using a 100 mm diverging lens and a 200 mm converging lens. The beam is focused down to a 23 µm radius at the ion using a 150 mm concave mirror.

Initially, we used the PDH EOM frequency for scanning the 1762 nm laser frequency. As the frequency is changed, the PDH cavity is able to re-lock to the new frequency as long as it's not changed by too much too quickly. In practice, we found that you could adjust it in increments of no more than 0.2 kHz and no faster than around $1\,\mathrm{kHz\,s^{-1}}$ without losing lock. This method worked to be able to find transitions, but it was too slow, so we added the second EOM to the path, imparting sidebands directly onto the laser being sent to the trap. These sidebands are used to drive transitions instead of the carrier, so that we have full fast control of the frequencies through the AWG source. We lock the laser to the red sideband of the PDH EOM and use the blue sideband of the main EOM to drive transitions. We found that in other orientations, the main EOM frequencies needed to drive transitions were too low and it could be possible to drive some transitions accidentally using the second order sidebands of this EOM.

4.1.2 Quadrupole transitions

To drive the electron from the ground state $S_{1/2}$ to the shelving state $D_{5/2}$, a quadrupole transition must be driven with a 1762 nm laser. Quadrupole transitions have selection rules similar to the selection rules in dipole transitions [39]:

$$\begin{aligned} F' &= F \text{ or } F' = F \pm 1 \text{ or } F' = F \pm 2 \\ m_F' &= m_F \text{ or } m_F' = F \pm 1 \text{ or } m_F' = m_F \pm 2. \end{aligned} \tag{4.1}$$

For ions without HF structure, there are only the m_J selection rules, and they are the same as shown above, just change m_F to m_J. From an individual $|S_{1/2}, F\rangle$ level, not all of the excited state levels can be reached because of these selection rules. In $^{138}\text{Ba}^+$ (nuclear spin $I = 0$), the $|S_{1/2}, m_J = +1/2\rangle$ state can only be driven into five of the six excited states because the m_J quantum number cannot be changed by more than 2. In $^{137}\text{Ba}^+$ (nuclear spin $I = 3/2$), the amount of allowed transitions is more dramatically reduced, with the $|S_{1/2}, F = 2, m_F = +2\rangle$ level only having 15 allowed transitions out of a total of 24 energy levels in the excited state.

The zero-field transition strength of each individual transition depends on the Clebsch-Gordon coefficients between the states in a straightforward manner [39, 191, 192]. This strength involves a geometric dependence which is set by the wavevector of the laser, it's polarization, and its angle from the magnetic field vector, shown in Figure 4.4. The first parameter is the angle between the magnetic field and the wavevector ϕ. The second parameter is defined with respect to the projection of the magnetic field onto the plane of incidence of the laser. γ is defined as the angle between the negative of this vector and the polarization vector of the laser ϵ. The transition strength dependence on these parameters is given by

$$\begin{aligned} g^{(0)} &= \frac{1}{2}|\cos\gamma\sin 2\phi| \\ g^{(\pm1)} &= \frac{1}{\sqrt{6}}|\mp\cos\gamma\cos 2\phi + i\sin\gamma\cos\phi| \\ g^{(\pm2)} = |g_{xx}^{(\pm2)} + g_{yx}^{(\pm2)}| &= \frac{1}{\sqrt{6}}\left|\frac{1}{2}\cos\gamma\sin 2\phi \mp i\sin\gamma\sin\phi\right|, \end{aligned} \tag{4.2}$$

and is illustrated in Figure 4.5. In our lab, we empirically picked a polarization which did a decent job of maximizing as many of the transitions in $^{137}\text{Ba}^+$ as possible, so that we could use as many of them as possible for our qudit.

With zero magnetic field, all of the Zeeman sub-levels of fine and HF states are degenerate, at the same energy. An external magnetic field is introduced in atomic experiments to break this degeneracy of electronic energy states, as shown in Figures 4.6 and 4.7. The magnetic field in most trapped ion quantum computing experiments is typically chosen to be 0.2 mT to 1 mT. This ensures that the degeneracy is lifted enough to avoid coherent

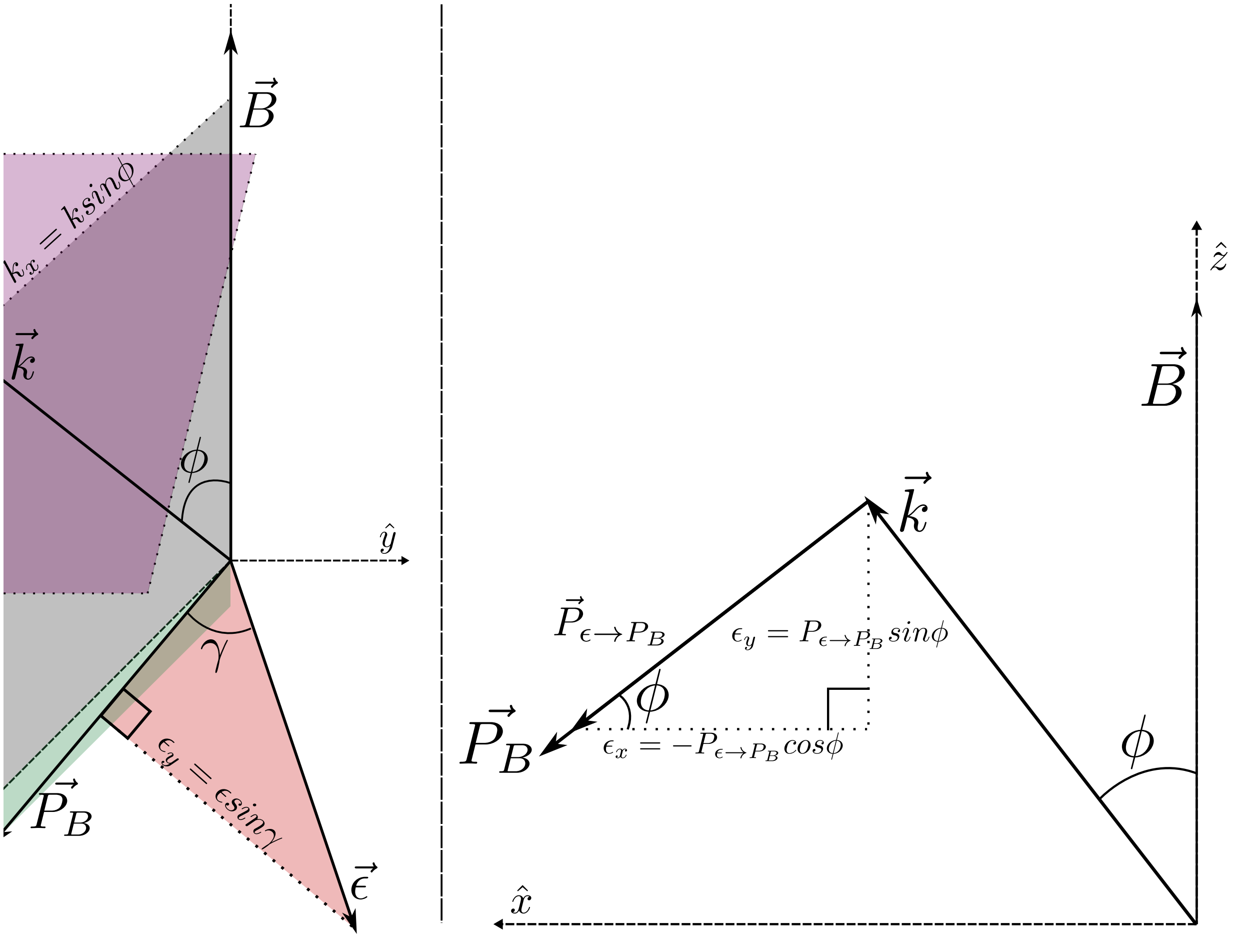

(a) (b)

Figure 4.4: Quadrupole transition laser orientation [39] with respect to the magnetic field, wave vector, and polarization are described using ϕ and γ. (a) Magnetic field $\vec{B}$, wavevector $\vec{k}$, polarization $\vec{\epsilon}$, plane of incidence, and the negative projection of the magnetic field onto the plane of incidence $\vec{P_B}$. (b) Projection of the polarization onto $\vec{P_B}$, labeled $\vec{P}_{\epsilon\to P_B}$.

dark states [193], where the electron can end up in some coherent superposition which has essentially no coupling with the fluorescence lasers anymore.

At these relatively low magnetic fields, the Zeeman effect splits the electronic states linearly (see Figure 4.6). The splitting is dependent on the g-factor of the states (shown in Figures 2.2 and 2.3 for barium ions), and the quantum number of the state m_J or m_F.

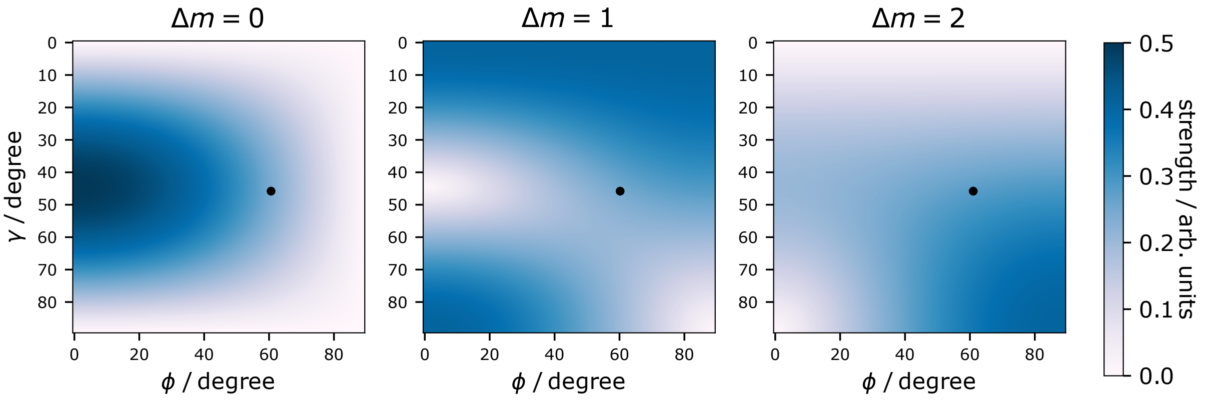

(a) (b) (c)

Figure 4.5: The quadrupole transition strength's geometrical dependence. Blue darker areas have a higher probability of driving the transition and white areas have a lower probability. Two orientations are notable: $\phi = 45°$, $\gamma = 0°$, which restricts only $\Delta m = 0$ transitions, and $\phi = 90°$, $\gamma = 90°$, which only allows $\Delta m = 1$ transitions. The black circle denotes the orientation we use.

For fine-structure and HF structure energy levels, this splitting is given by

$$\Delta E_f = \left(g_L + (g_S - g_L)\frac{J(J+1)+S(S+1)-L(L+1)}{2J(J+1)} \right) \mu_B m_J B = g_J \mu_B m_J B, \quad (4.3)$$

$$\Delta E_{hf} = g_J \frac{(F(F+1)+J(J+1)-I(I+1))}{2F(F+1)} \mu_B m_F B = g_F \mu_B m_F B, \quad (4.4)$$

where $g_J = \left(g_L + (g_S - g_L)\frac{J(J+1)+S(S+1)-L(L+1)}{2J(J+1)} \right)$ is the fine g-factor, $g_l \approx 1$ is the angular momentum g-factor, $g_S \approx 2$ is the electron spin g-factor, S is the electron spin, L is the angular momentum, $J = L + S$ is the total angular momentum, $\mu_B = 9.27 \times 10^{-24}\,\mathrm{J\,T^{-1}}$ is the Bohr magneton, m_J is the magnetic fine quantum number, B is the magnitude of the magnetic field, I is the nuclear spin angular momentum, $F = I + J$ is the HF angular momentum, m_F is the magnetic HF quantum number, and $g_F = g_J \frac{(F(F+1)+J(J+1)-I(I+1))}{2F(F+1)}$ is the HF g-factor. For atoms with no HF structure such as $^{138}\mathrm{Ba}^+$, Equation 4.3 is sufficient to describe the Zeeman splittings up to very high magnetic fields, and the energy structure for $^{138}\mathrm{Ba}^+$ is shown in Figure 4.6. For atoms with a nuclear spin $I > 0$, this model can also be pretty accurate. However, in $^{137}\mathrm{Ba}^+$, the $D_{5/2}$ energy levels begin to overlap with each other very quickly, especially for the $F \in \{3, 4\}$ HF levels. In this regime, the states mix and the F quantum number ceases to be a good way to describe the system. The nuclear spin I and angular momentum J must be used to get an accurate estimation of the magnetic field dependence.

Level	A (MHz)	B (MHz)	F	g_F	Freq (MHz)
$S_{1/2}$	4018.870834	-	1	-0.5	-5023.58875
			2	0.5	3014.15325
$P_{1/2}$	743.7	0	1	$-0.1\overline{6}$	-929.625
			2	$0.1\overline{6}$	557.775
			0	0	-364.5
$P_{3/2}$	127.2	59	1	$0.\overline{6}$	-327.3
			2	$0.\overline{6}$	-162.9
			3	$0.\overline{6}$	308.7
			0	0	-655.81
$D_{3/2}$	189.729	44.5408	1	0.4	-510.6212
			2	0.4	-175.7028
			3	0.4	438.0268
			1	2.1	104.82
$D_{5/2}$	-12.028	59.533	2	$1.0\overline{9}$	33.1377
			3	0.85	-29.73615
			4	0.75	-30.22175

Table 4.1: Characteristics of $^{137}\mathrm{Ba}^+$ energy structure [194–196]. A is the magnetic dipole HF constant, B is the quadrupole HF constant, F is the HF angular momentum, g_F is the HF g-factor.

The Hamiltonian matrix for a single energy level of any atom with HF structure has diagonal terms given by [39]

$$\begin{aligned}\langle\vec{H}\rangle = {} & A m_I m_J + \frac{\mu_B}{\hbar}(g_J m_J B_e + g_I m_I B_e) + \frac{B}{2I(2I-1)J(2J-1)} \\ & \times \left[\frac{3}{2} m_I m_J + 3 m_I^2 m_J^2 + \left\langle \frac{I_- I_+ J_+ J_-}{4} \right\rangle + \left\langle \frac{I_+ I_- J_- J_+}{4} \right\rangle - I(I+1)J(J+1)\right],\end{aligned} \tag{4.5}$$

and off diagonal terms given by

$$\begin{aligned}&2\langle m_J \pm 1, m_I \mp 1|\vec{H}|m_J, m_I\rangle = \\ &\left[A + \frac{B}{2I(2I-1)(J(2J-1)}\left(\frac{3}{2} + 3(m_I \mp 1)(m_j \pm 1) + m_I m_J\right)\right]\langle m_J \pm 1, m_I \mp 1|I_\mp J_\pm|m_J, m_I\rangle,\end{aligned} \tag{4.6}$$

and

$$\langle m_J \pm 2, m_I \mp 2|\vec{H}|m_J, m_I\rangle = \frac{3B}{8I(2I-1)(J(2J-1)}\langle m_J \pm 2, m_I \mp 2|I_\mp I_\mp J_\pm J_\pm|m_J, m_I\rangle, \tag{4.7}$$

where m_I is the nuclear spin magnetic quantum number, A is the magnetic dipole HF constant, B is the electric quadrupole HF constant (see Table 4.1), and $I_\pm$, $J_\pm$ are ladder operators for the nuclear spin momentum and the total angular momentum. These operators can be written as

$$\begin{aligned}\langle I_\mp I_\pm J_\pm J_\mp\rangle &= [I(I+1) - m_I(m_I \pm 1)]\,[J(J+1) - m_J(m_J \mp 1)] \\ \langle m_J \pm 1, m_I \mp 1|I_\mp J_\pm|m_J, m_I\rangle &= \sqrt{[J(J+1) - m_J(m_J \pm 1)]\,[I(I+1) - m_I(m_I \mp 1)]} \\ \langle m_J \pm 2, m_I \mp 2|I_\mp I_\mp J_\pm J_\pm|m_J, m_I\rangle &= \sqrt{[I(I+1) - m_I(m_I \mp 1)]\,[I(I+1) - (m_I \mp 1)(m_I \mp 2)]} \\ &\quad \times \sqrt{[J(J+1) - m_J(m_J \pm 1)]\,[J(J+1) - (m_J \pm 1)(m_J \pm 2]}.\end{aligned} \tag{4.8}$$

Depending on the nuclear spin I of the atom in question and the fine-structure angular momentum J of the electronic energy level, some of these terms may or may not be present. For example, in $^{133}\mathrm{Ba}^+$ with $I = 1/2$, the terms in Equation 4.7 will never exist because the nuclear spin quantum number m_I can never change by more than 1. Similarly, energy levels with $J = 1/2$ angular momentum will never have these terms since the angular momentum quantum number m_J can never change by more than 1. Diagonalizing this equation for multiple levels, the frequencies of different transitions can be found, including the one we care about now, the $S_{1/2} \leftrightarrow D_{5/2}$ quadrupole transition in $^{137}\mathrm{Ba}^+$. Simply diagonalize the equation for the ground state $S_{1/2}$, the excited state $D_{5/2}$, and find the frequency differences between the upper and lower energy levels for transitions which are allowed.

The theoretical frequencies of the quadrupole transition are shown in Figures 4.6 and 4.7 for $^{138}\mathrm{Ba}^+$ and $^{137}\mathrm{Ba}^+$. These just show the transitions which we can drive from the $|S_{1/2}, m_J = +1/2\rangle$ and $|S_{1/2}, F = 2, m_F = +2\rangle$ states which are optically pumped to in the current polarization of that beam path.

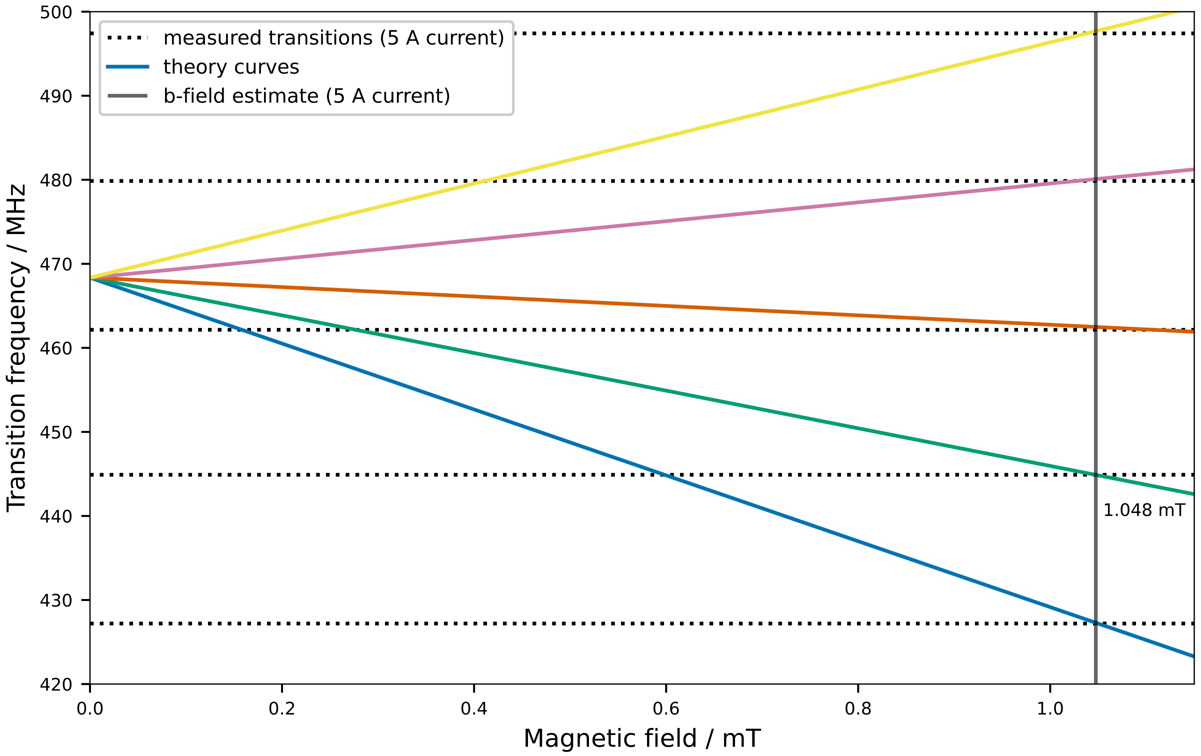

Figure 4.6: Expected transition frequencies in $^{138}\mathrm{Ba}^+$ as a function of the magnetic field, calculated from Equation 4.3. The horizontal lines are the transition frequencies measured and discussed in Section 4.2 (two coils driven at 5 A), and the magnetic field is estimated to be $10.48\,\mathrm{G} = 1.048\,\mathrm{mT}$.

The frequencies for $^{138}\mathrm{Ba}^+$ were simply calculated from the subtracting the linear splitting of the $S_{1/2}$ ground state from the linear splitting of the excited state $D_{5/2}$. The result is an even splitting of the energy levels, with a splitting on the order of 10 MHz past 0.8 mT. The two outer transitions to the states $m_{J'} \in \{+5/2, -3/2\}$ are the most sensitive to magnetic field while the middle $m_{J'} = +1/2$ transition is the least magnetic field sensitive.

The frequencies for the quadrupole transitions of $^{137}\mathrm{Ba}^+$ were calculated using Equations 4.5, 4.6, and 4.7 to construct a matrix. The diagonalization of this matrix for each separate magnetic field yields the frequencies for each transition at that magnetic field. The upper $F' \in \{1, 2\}$ transitions are well isolated from each other, however the two $F' \in \{3, 4\}$ transitions have frequencies which are extremely close to one another. As the magnetic field is increased, the HF states immediately start crossing and mixing with each other.

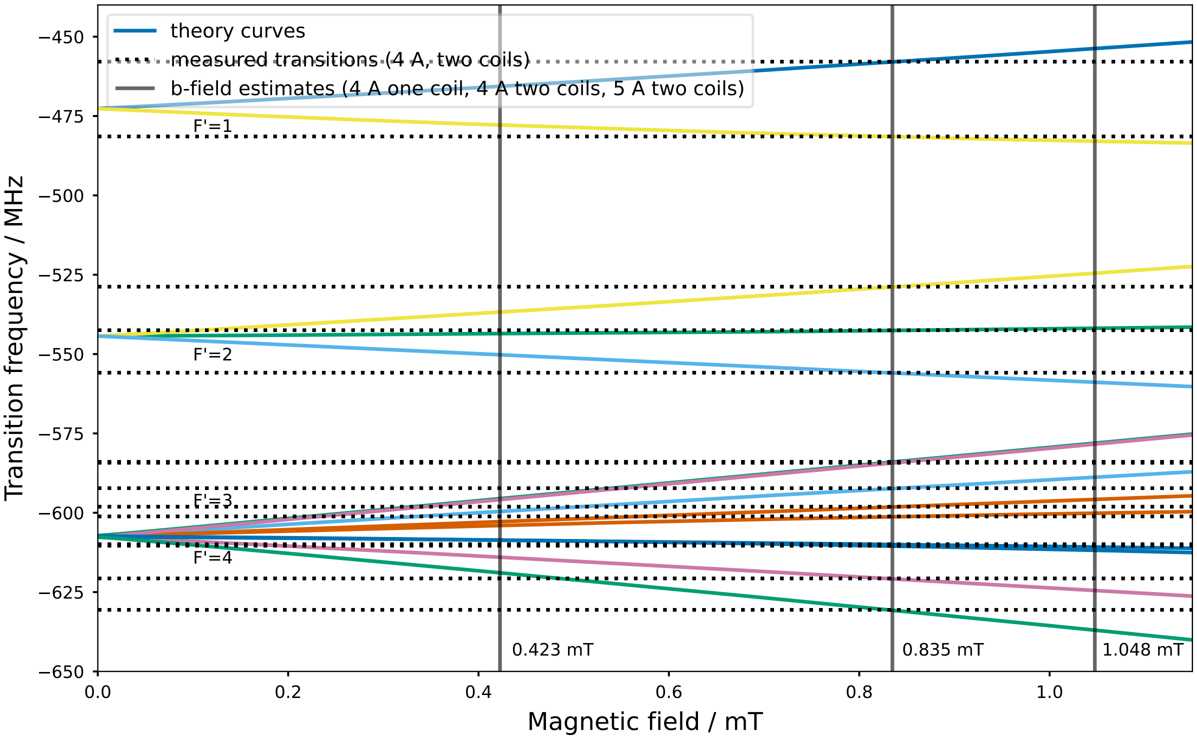

Figure 4.7: Expected transition frequencies in $^{137}\mathrm{Ba}^+$ as a function of the magnetic field, calculated from diagonalizing the matrix from Equations 4.5, 4.6, 4.7. The horizontal lines are the transition frequencies measured and discussed in Section 4.2 with 4 A applied to both magnetic field coils. The magnetic field for this configuration is estimated to be 8.35 G =0.835 mT.

For this reason, these states experience some interference which results in surprisingly low transition strengths of the $F' = 3$ transitions described in the next section. One might think that this close proximity of the two sets of levels would make it much harder to use these levels. However, while it might be a bit harder to find which transitions are which, the transitions themselves are quite narrow and there are no problems performing coherent operations on almost all of these transitions.

4.2 Transitions characterization

We use the 1762 nm laser to drive quadrupole transitions in barium. For the experiments presented, we use an overall laser power of 3 mW and an RF power on the second EOM of 3 dBm unless otherwise stated. For the most part, we perform optical pumping for on the order of 500 µs and shelf-repumping (614 nm) for 500 µs to 5.000 µs, depending on the power of this laser at the time of the experiment. This power fluctuated somewhat from 4 µW to 13 µW at the ion. The fluorescence cooling lasers, 493 nm and 650 nm, had laser powers of 20 µW to 50 µW and 150 µW to 250 µW. When locking to the cavity peak for driving transitions in $^{138}\mathrm{Ba}^+$, a PDH EOM frequency of 140 MHz is used with a power amplitude of 10%. For driving $^{137}\mathrm{Ba}^+$ transitions, we lock to the cavity peak using a PDH EOM frequency of 240 MHz with a power amplitude of 20%.

4.2.1 Transition spectra

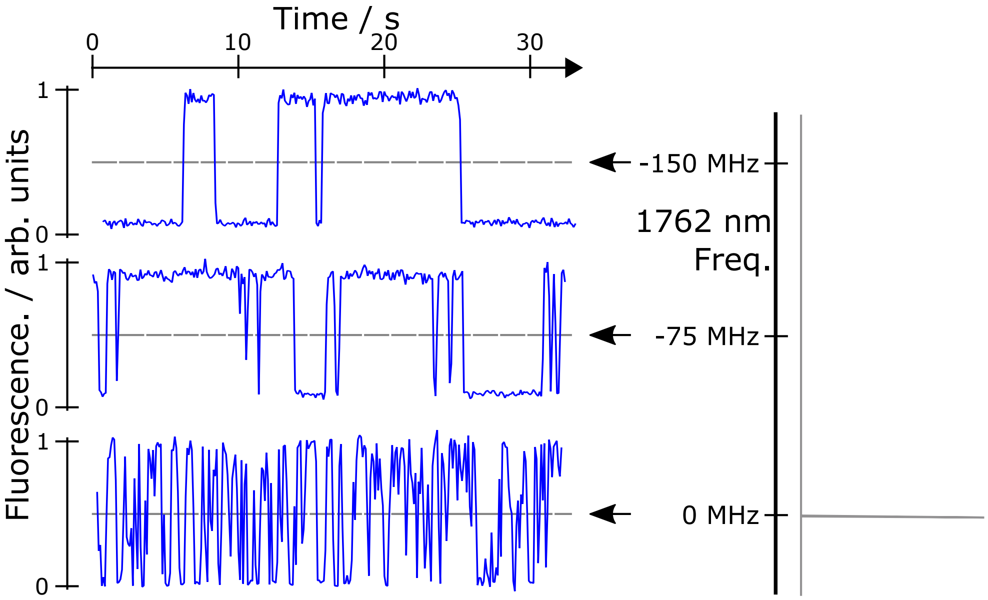

Figure 4.8: The 493 nm fluorescence signal flip-flops between bright and dark with the 1762 nm laser approaching the correct transition frequency. Both cooling lasers are on, and as the 1762 nm nears the correct frequency, the flip-flops become more frequent. The right side shows the 1762 nm spectrum without the cooling lasers, with the transition peak being very narrow.

The natural linewidth of this transition is quite narrow, in the millihertz range. With broadening mechanisms, this is widened up to kilohertz, which is still quite narrow and difficult to find. Using a wavelength-meter, we adjusted the frequency to be within 1 GHz of where we expected the transition to be, but this is still a huge frequency space to search for a kilohertz transition. Fortunately, we can broaden the transition, helping us to roughly find it: just keep the cooling lasers (493 nm and 650 nm) on while addressing the ion with the shelving laser. As shown in Figure 4.8, if the cooling lasers are on with the shelving laser, the ion can become shelved and then be de-shelved on a timescale of seconds. As the shelving laser frequency is tuned closer to the correct transition frequency, the flip-flopping becomes more and more frequent. Using this method, we can broaden the transition so that we can tune our laser frequency to within 10's of megahertz of the actual transitions.

Once the vicinity of the transitions has been found, the laser must be locked to the PDH cavity in order to keep its frequency stable enough to coherently drive quadrupole transitions into the $D_{5/2}$ state. In Figure 4.3, the peaks of the cavity are shown; gray peaks are from the laser carrier, and blue/red peaks are from the sidebands imparted by the PDH EOM. The laser frequency is controlled by changing the piezo voltage in the ECDL, with a ratio of $\sim 140\,\mathrm{MHz\,V^{-1}}$. The transitions in $^{138}\mathrm{Ba}^+$ and $^{137}\mathrm{Ba}^+$ are also shown in this Figure.

To drive transitions in these isotopes, sidebands from a nearby carrier are locked to. With the laser locked, the frequency of either the PDH EOM or the external EOM can be scanned over with the laser being sent to the trapped ion. This frequency scanning can be done directly with the PDH EOM, but as mentioned in the previous section, this is slow because the laser must re-lock between steps. Instead, we lock to a fixed, low-frequency, PDH EOM red sideband while we scan the frequency applied to the second EOM. The frequencies are supplied by an AWG, and the blue sideband imparted by this EOM is used to drive the transitions.

To analyze the fluorescence data from the PMT, typically some kind of threshold is defined and all of the data is compared to that threshold. If the counts are higher than that threshold, then the ion is considered to be fluorescing in the ground state. If the counts are lower, the ion is considered to be dark and not in the fluorescence states (it's in the $D_{5/2}$ or some other dark state). The typical way of doing this is to perform some calibration regularly which uses statistics to determine the best threshold. In our work, we use a retroactive method where we use the data itself to determine the threshold (see Reference [121] for more details). This only works if the data is has some mixture of bright and dark states (at least 10% of each is usually necessary).

For $^{138}\mathrm{Ba}^+$, we lock the 1762 nm laser to the 56 V cavity peak's red sideband, with the

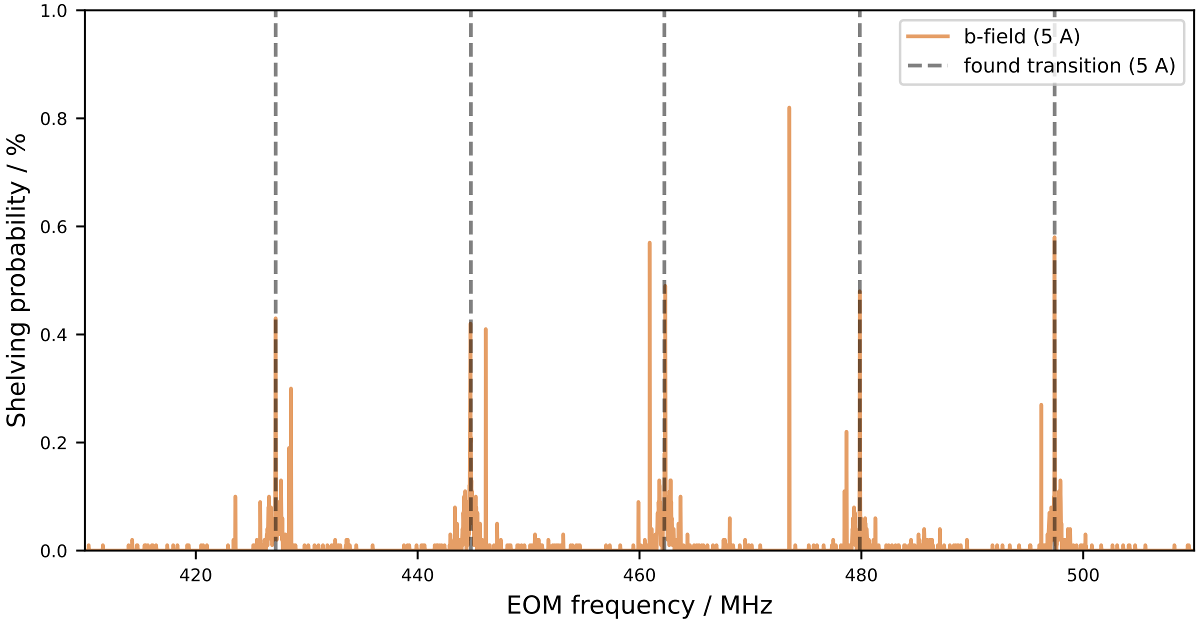

Figure 4.9: Spectrum of the quadrupole transition in $^{138}Ba^+$. The dotted vertical lines are the frequencies where we found the transitions (Rabi oscillations). A current of 5 A is used to drive both magnetic field coils. For this data, the 1762 nm was locked to the blue sideband.

frequency of this sideband at 140 MHz and the amplitude at 10%. We then use the blue sideband of the second EOM, with the source from the AWG, to drive coherent transitions. We pump the electron into the stretched state using the 493 nm optical pumping laser for 500 µs, deliver the 1762 nm laser to the ion for 3.000 µs, then send the fluorescence lasers 493 nm and 650 nm to see if the ion has been shelved or not. The 614 nm laser is used to reset the experiment in the ground state and the experiment is repeated for the next scan point. The EOM frequency is scanned from 410 MHz to 510 MHz, and the results are the spectrum shown in Figure 4.9. The orange peaks are all possible transition peaks, and the vertical dotted lines are the transitions which we confirmed as carrier transitions (by observing Rabi oscillations). Many of the smaller peaks surrounding the carrier peaks turn out to be motional modes, including the radial peaks at 1.2 MHz and 1.4 MHz and the axial peak at 10 kHz. In addition, some peaks are micromotion peaks at the trap RF frequency of 20.772 MHz. Many of the peaks are actually situations where the ion went dark for some reason other than shelving. This can happen if the ion heats up and de-crystallizes, which can occur when a stray atom or molecule collides with it.

In Figure 2.2, these found transitions are plotted as horizontal lines, and their positions correspond with an overall magnetic field of 1.048 mT. Table 4.2 shows the measured frequencies for all of these transitions at the different magnetic fields. Note that with lower magnetic field, we were locking to the opposite (blue) PDH sideband, and so the absolute frequencies differ by twice that frequency, or 280 MHz.

$m_{J'}$	B_h freq. (MHz)	B_l freq. (MHz)	π-time (μs)	π error
5/2	427.193	-725.296	34	0.063
3/2	444.751	-732.39	26.8	0.072
1/2	462.31	-739.482	29.9	0.056
-1/2	479.866	-746.576	42.3	0.049
-3/2	497.424	-753.673	40	0.093

Table 4.2: Measurements on the transitions in ^{138}Ba$^+$. B_h, and B_l stand for high (1.048 mT) and low (0.423 mT) magnetic fields respectively. Note that the two sets of frequencies were found while locking to opposite sidebands of the PDH cavity. The absolute values differ by twice the PDH frequency, 280 MHz.

To drive transitions in ^{137}Ba$^+$, we lock the 1762 nm laser to the 36 V cavity peak's red sideband, with the frequency of this sideband at 240 MHz and the amplitude at 20%. We then use the red sideband of the second EOM to drive coherent transitions. We use the same procedure described in the previous paragraph to collect a spectrum. The results of this scan are shown in Figure 4.10, with a scan range of 410 MHz to 510 MHz on the EOM frequency. This was performed using a current source of 4 A and 5 A on both of our coils, with the successfully found transitions shown as vertical dotted and dashed lines. This spectrum is a lot busier than the ^{138}Ba$^+$ spectrum, but you can see the transitions shift from the different magnetic fields experienced by the ion. In addition to being denser in terms of the number of transitions, there are also many more random peaks present where the ion goes 100% dark. As described for the ^{138}Ba$^+$ spectrum, these are situations where the ion de-crystallizes. In ^{137}Ba$^+$, these occurrences happen much more often than for ^{138}Ba$^+$, probably because the Doppler cooling is not as efficient. The overall brightness of ^{137}Ba$^+$ is on the order of $6,000$ counts/s, nearly one third the $15,000$ counts/s brightness of ^{138}Ba$^+$.

In Figure 2.3, these found transitions for 4 A current are shown as horizontal lines. At 0.835 mT, the found transition frequencies match the theoretical curves to within 10 kHz, indicating that our model of the energy structure is good. Transitions at the other configurations were also found and match up well with the theory curve, with the 4 A, single coil

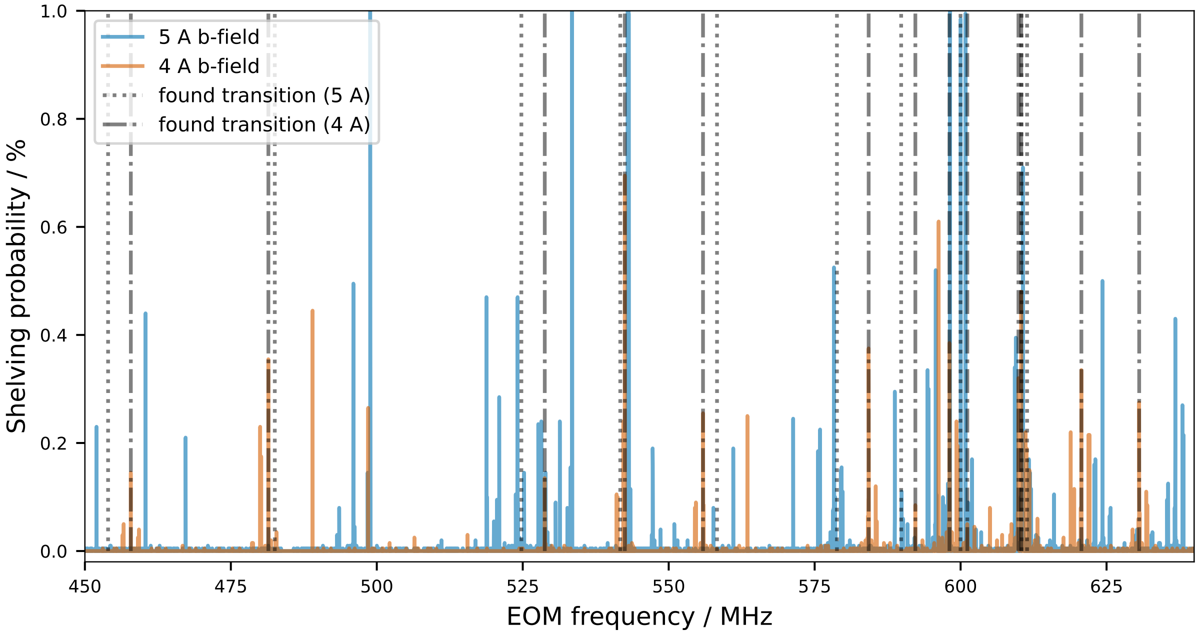

Figure 4.10: Spectrum of the quadrupole transition in $^{137}\mathrm{Ba}^{+}$. The dotted vertical lines are the frequencies where we found the transitions (Rabi oscillations) using a current source of 4 A and 5 A on both of our magnetic field coils. For this experiment, the 1762 nm laser was locked to the red sideband.

configuration resulting in a magnetic field of 0.423 mT and the two-coil 5 A configuration having a magnetic field of 1.048 mT, matching with the result for $^{138}\mathrm{Ba}^{+}$.

The procedure to find a transition goes as follows:

1. Perform a wider scan, about 100 kHz to 1.000 kHz wide (depending on how certain you are of where it should be) near where you expect the transition to be, with a step-size of 10 kHz. Use a high EOM RF power, ~ 3 dBm, to broaden the transition as much as possible. Set the pulse-time to be longer than the coherence time, ~ 3.000 µs, to make the transition incoherent so that coherent processes can't give a false peak. A dip should be seen in at least one of the data points indicating where the transition is.

2. To find the exact transition frequency, perform an even finer frequency scan (about 10 kHz to 20 kHz with a step size of 1 kHz around the peak found in the previous step) of the 1762 nm laser, as shown in Figure 4.11. For this scan, use a low EOM RF

F'	$m_{F'}$	B_m freq. (MHz)	B_h freq (MHz)	B_l freq. (MHz)	π-time (μs)	π error
1	1	-457.869	-453.542	-465.96	295.9	0.31
1	0	-481.43	-482.647	-478.112	95.1	0.054
2	2	-528.771	-524.323	-537.159	58.6	0.11
2	1	-542.483	-541.622	-543.906	123.8	0.03
2	0	-555.877	-558.549	-550.519	62.2	0.026
3	3	-583.95	-577.18	-595.891	>2000	-
4	4	-584.251	-578.223	-596.203	66.8	0.075
3	2	-592.25	-588.562	-599.889	129.7	0.23
4	3	-598.091	-595.577	-603.102	39.4	0.016
3	1	-601.151	-599.877	-604.244	298.1	0.05
4	2	-609.91	-610.512	-608.921	23.6	0.023
3	0	-610.385	-611.525	-608.856	181.1	0.049
4	1	-620.689	-624.288	-614.239	93.5	0.03
4	0	-630.59	-636.766	-619.16	69.3	0.07

Table 4.3: Measurements on the transitions in $^{137}\mathrm{Ba}^{+}$. B_h, B_m, and B_l stand for high (1.048 mT), medium (0.835 mT), and low (0.423 mT) magnetic fields respectively. The $F' = 3, m_{F'} = 3$ transition is extremely weak, so no π-pulse error is listed.

power, $\sim -20\,\mathrm{dBm}$, to narrow the transition as much as possible so that the exact frequency is easier to determine. Set the pulse-time a little longer than the previously measured π-time of the transition. This increases the contrast and makes sure that frequencies off resonance only give worse shelving probabilities. The transition lineshape should be clear from this scan.

3. Analyze the data using the threshold method described in Reference [121] to get the probability of shelving at each frequency. Fit this data to a Lorentzian,

$$y = \frac{Amp}{1 - \frac{x-f_0}{FWHM}^2} + BG, \tag{4.9}$$

to find the exact transition frequency.

Initially, finding all of the quadrupole transitions in $^{137}\mathrm{Ba}^{+}$ was very challenging. First, it's very important to be sure of which ground stretch state you are optically pumping to, otherwise the frequencies you're looking for based on the theory will be completely

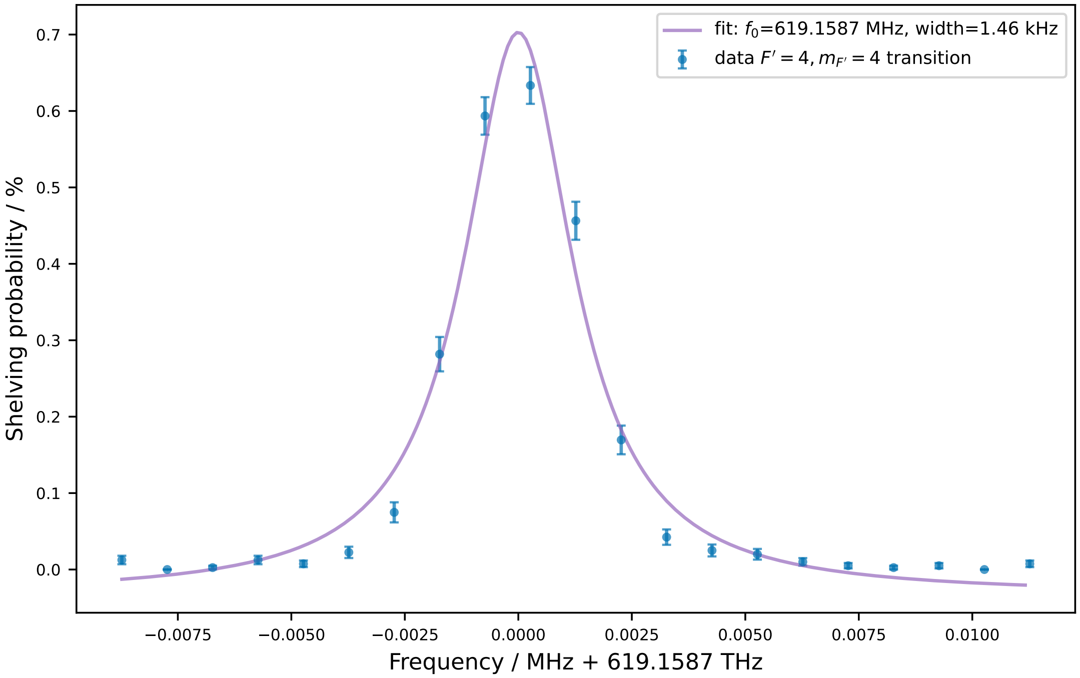

Figure 4.11: Quadrupole transition spectrum of the $|S_{1/2}, F = 2, m_F = 2\rangle \leftrightarrow |D_{5/2}, F' = 4, m_{F'} = 4\rangle$ transition. A low EOM RF power of −20 dBm with a long pulse time of 3000 µs is used to make the transition as narrow as possible to be able to find the exact transition frequency more easily. The fit gives a linewidth of 1.46 kHz. Each data point is 400 experiments.

different. Without a magnetic field estimation, it's very hard to know which transitions in the $F' \in \{3, 4\}$ are which. In addition, a few of these transitions turned out to be very weak, much weaker than expected based on the standard transition strengths. To find these weak transitions, a very fine scan over the entire range was needed. You can also use the expected linear magnetic field sensitivity to estimate which transitions are which based on how they shifted from moving to a different applied current, as shown in Figure 4.10. Once all of the transitions were found and the two magnetic field results were compared, we were finally able to assign all of the transitions their proper excited states. The frequencies of all of the transitions for different magnetic fields are shown in Table 4.3.

When we switched to using only one of the magnetic field coils, the voltage readout of the current source nearly exactly halved from 2.38 V to 1.234 V. This indicates that the coils are nearly identical, and that the new magnetic field should be very close to exactly

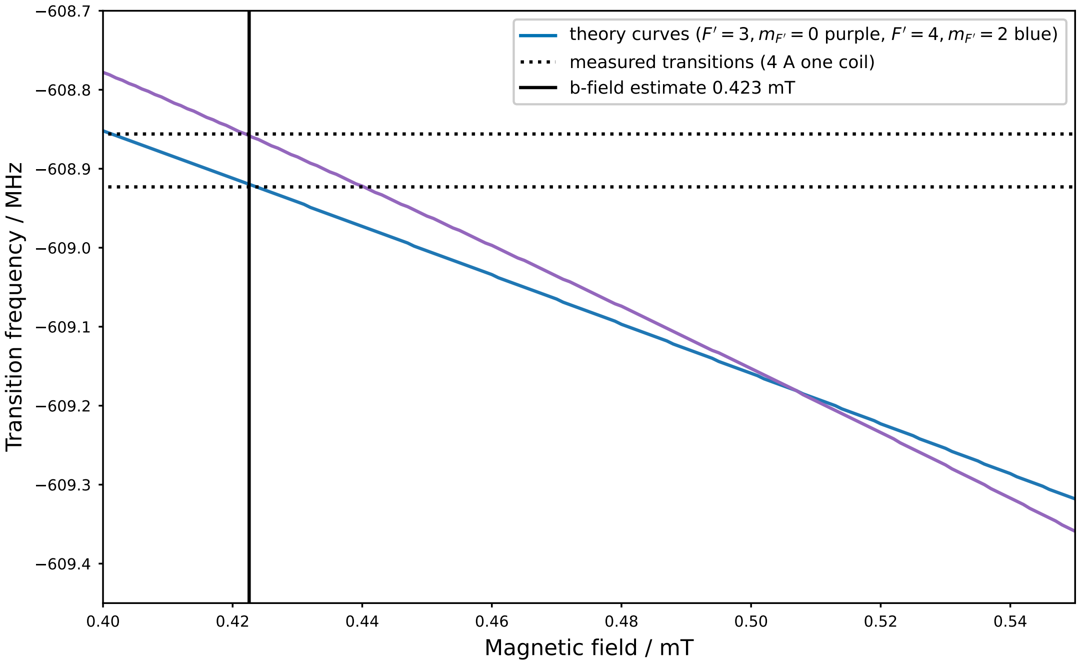

Figure 4.12: $^{137}\mathrm{Ba}^{+}$ quadrupole transition energies using a lower magnetic field of 0.423 mT. The $F' = 3, m_{F'} = 0$ and $F' = 4, m_{F'} = 2$ transitions have transition frequencies very near one another.

half the previous magnetic field. It also made looking for the new frequencies quite easy, as we could use the model in Equations 4.5, 4.6, and 4.7 to find the expected frequencies for half magnetic field. The frequencies were all within 30 kHz of this estimation for all transitions, and the magnetic field from the measured transitions is found to be 0.423 mT. Because of this agreement, we can also infer that the magnetic field coils are quite well aligned symmetrically on the trap.

Another consequence of reducing the magnetic field was that the two transitions $F' = 3, m_{F'} = 0$ and $F' = 4, m_{F'} = 2$ are much closer in frequency, around 100 kHz instead of the over 400 kHz measured for the higher magnetic fields. The two transitions even cross at around 0.51 mT as shown in Figure 4.12. While the 100 kHz difference is enough to perform coherent operations on the two transitions, care must be taken to not pick a quantization magnetic field where two levels cross such as these two. One must also take care when finding these two transitions using a fitting method; an erroneous result could occur for the calibrated frequency if they both end up being within the same frequency scan.

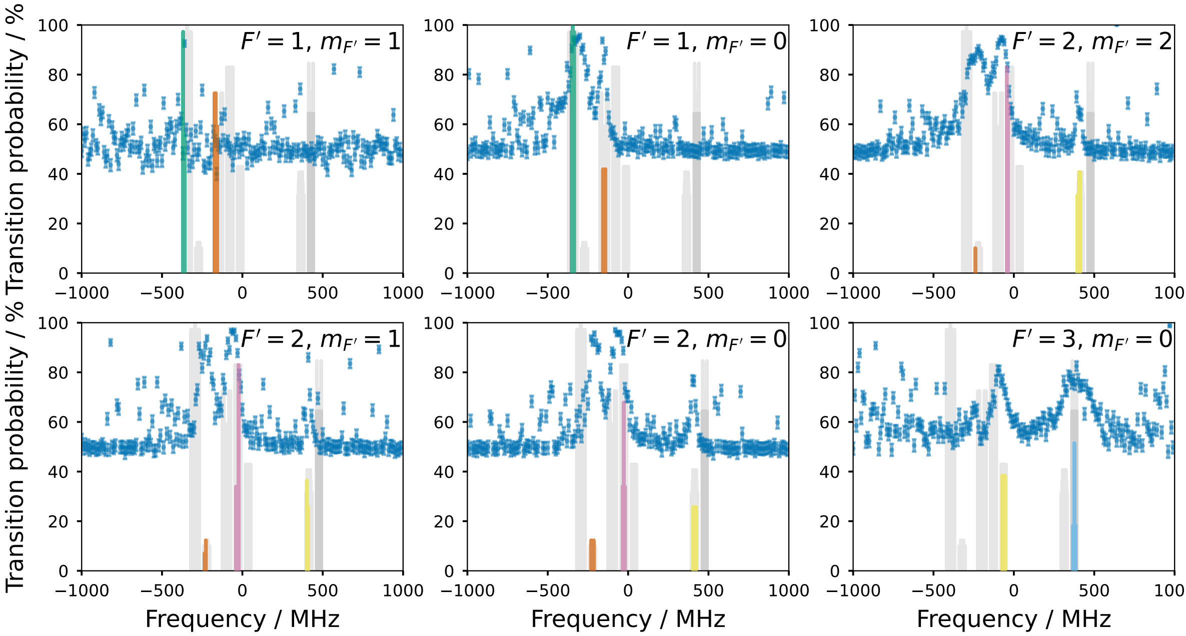

Figure 4.13: The 614 nm laser spectrum from different initial $D_{5/2}$ energy levels. A magnetic field of 0.835 mT is used. Vertical lines denote all of the transitions into the $P_{3/2}$ state, with colored lines being accessible transitions from the $D_{5/2}$ energy level initialized in, and grey lines being all the other transitions.

We also investigated the spectrum of the 614 nm transition from $D_{5/2} \leftrightarrow P_{3/2}$, which we use to flush the shelving state in between experiments. The transition probability is measured as a function of this laser's frequency, for different shelving states. To perform this experiment, the electron is driven into the $D_{5/2}$ shelving state incoherently, with a pulse time of 3.000 µs. Then the shelving repump laser is introduced for a very short amount of time. Driving out of the $D_{5/2}$ state using this dipole transition is very fast and easy, so a sufficiently short pulse time must be picked so that we aren't just perfectly repumping every time. A time is picked empirically such that the transition isn't completely repumped and we can see peaks in the spectrum, as shown in Figure 4.13. The peaks we found match up quite well with the theoretical transitions that should be possible from the initialized excited states, shown as colored vertical lines.

Not shown in this Figure are transitions from the $F' = 4, m_{F'} = 4$ state, which only has one transition by which it can be repumped into the $P_{3/2}$ state. Because of this, there are some sacrifices to be made when picking the frequency to set the 614 nm laser to. The rest of the transitions can easily be driven with a single laser frequency such that all of them are within 10 MHz and can be repumped in under 100 µs, but the $F' = 4, m_{F'} = 4$ state must be repumped with at least 400 MHz detuning, which takes 500 µs or longer. In the future, an EOM could be used to significantly improve this by splitting the power of the laser into multiple frequencies, hitting all of the transitions more evenly.

4.2.2 Coherent shelving operations

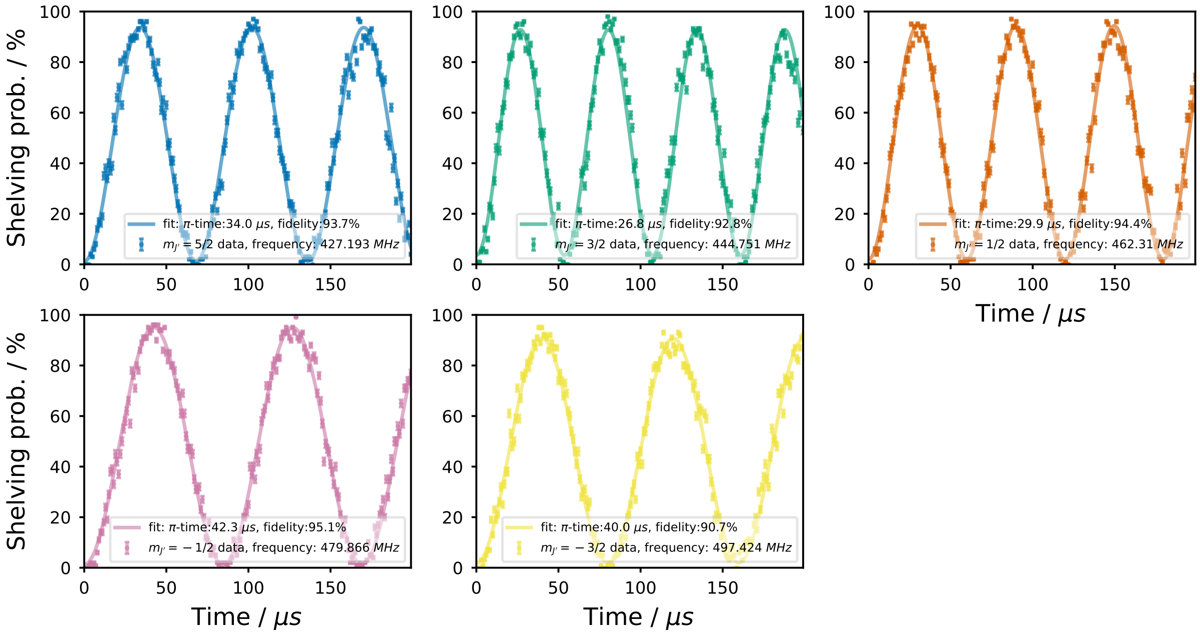

Figure 4.14: Rabi oscillations of all of the $^{138}\mathrm{Ba}^{+}$ quadrupole transitions driven from the ground state $|S_{1/2}, m_J = +1/2\rangle$. Magnetic field is 1.048 mT.

A transition can be coherently driven from one ground $S_{1/2}$ state to an excited $D_{5/2}$ state in a coherent process known as a Rabi oscillation. We first pump the electron into the stretched state using the 493 nm optical pumping laser for 500 µs. Next, we apply the 1762 nm laser to drive the quadrupole transition for a set amount of time. The electron will be transferred to the shelving $D_{5/2}$ state with a probability dependent on the amount of time the transition is driven for. The Hamiltonian of the ion with a laser interacting

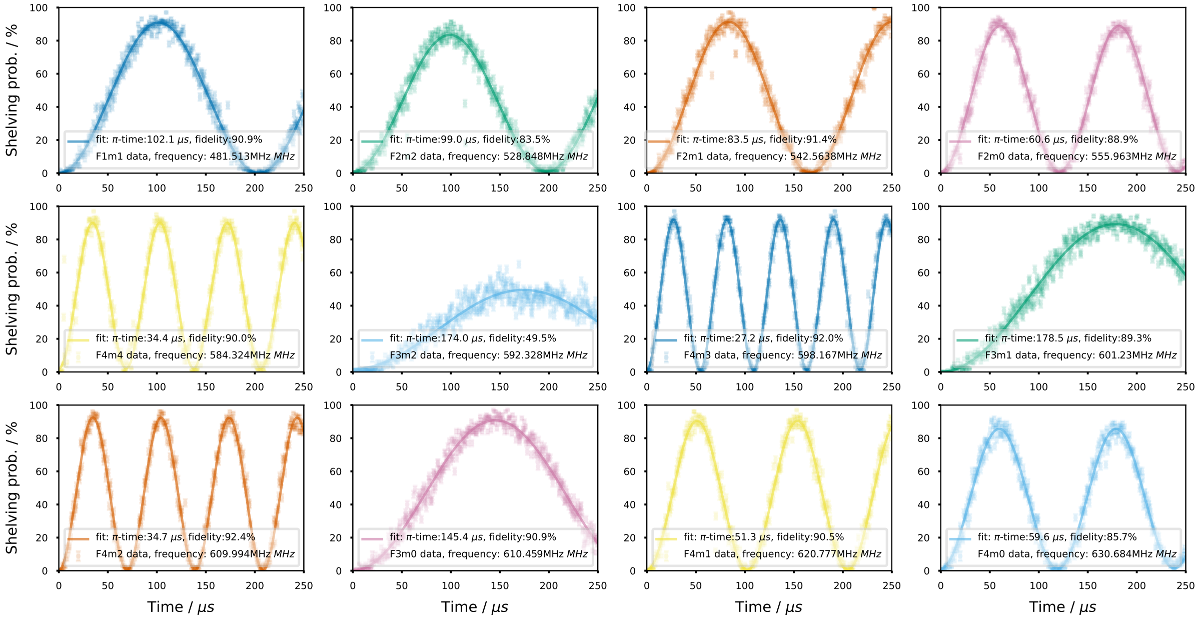

Figure 4.15: Rabi oscillations of all of the $^{137}\mathrm{Ba}^{+}$ quadrupole transitions driven from the ground state $|S_{1/2}, F=2, m_F=+2\rangle$. Magnetic field is 0.835 mT.

with it is given by

$$H = H_a + H_{af} = \hbar\omega_0 |e\rangle\langle e| + \frac{\hbar\Omega}{2}\left(|g\rangle\langle e|e^{i\omega t} + |e\rangle\langle g|e^{-i\omega t}\right), \tag{4.10}$$

where $H_a = \hbar\omega_0|e\rangle\langle e|$ is the Hamiltonian of the ion alone, H_{af} is the Hamiltonian of the interaction between the ion and the laser, ω_0 is the energy of the excited state (in frequency), $\Omega = -\frac{\langle g|\varepsilon \cdot d|e\rangle E_0}{\hbar}$ is a parameter called the Rabi frequency which characterizes the strength and speed of the interaction, ε is the polarization of the field, d is the dipole operator of the ion, E_0 is the magnitude of the electric field from the laser, and ω is the frequency of the laser. Using Schrødinger's equation and moving to a Rotating frame [197], the resulting behavior is that the electron oscillates sinusoidally between the ground state and the excited state. At zero detuning, the frequency of these oscillations is the Rabi frequency and the contrast is one. If the frequency of the laser is detuned, the frequency of the oscillations is increased from the Rabi frequency and the electron can never be fully excited. With zero detuning, assuming the electron starts in the ground state, the

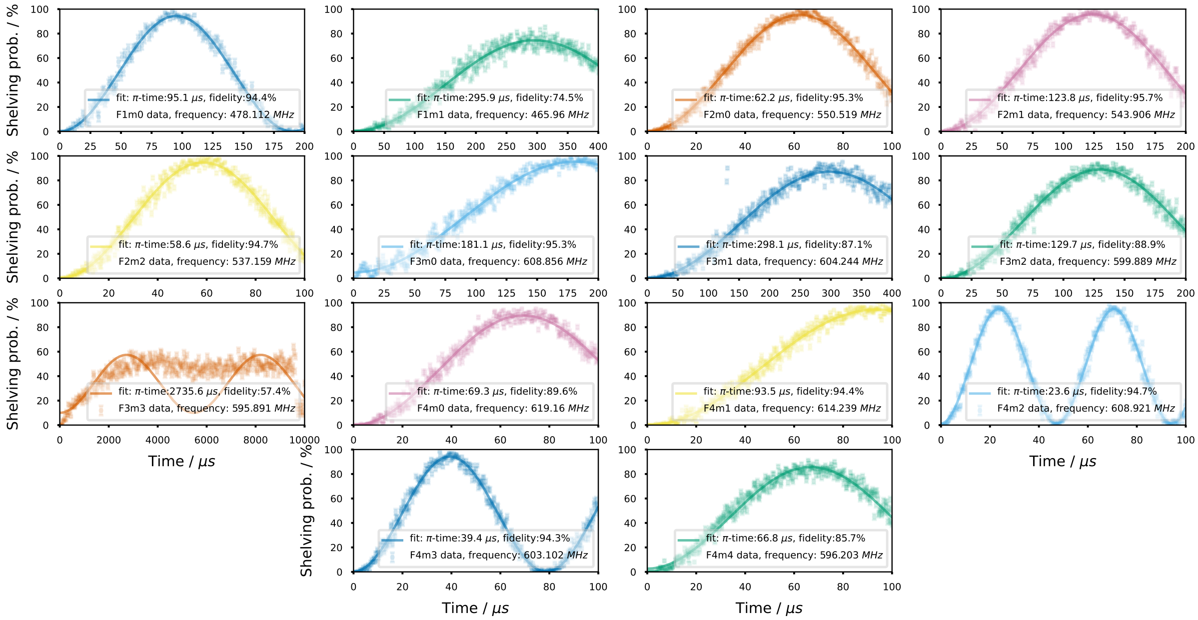

Figure 4.16: Rabi oscillations of all of the $^{137}\mathrm{Ba}^+$ quadrupole transitions driven from the ground state $|S_{1/2}, F = 2, m_F = +2\rangle$. Magnetic field is 0.423 mT.

probability of driving to the excited state looks like

$$P_e(t) = \frac{1}{2}\left(1 - \cos(\Omega t)\right). \tag{4.11}$$

The amount of time it takes for the electron to be fully excited into the excited state is called the π-time or τ_π.

Rabi oscillation experiments are performed by scanning the pulse time of applying the 1762 nm laser to the ion. The results are shown in Figures 4.14, 4.15, 4.16 for the $^{138}\mathrm{Ba}^+$ ion using 1.048 mT magnetic field and for $^{137}\mathrm{Ba}^+$ using 0.835 mT and 0.423 mT magnetic fields. The results are fitted using equation 4.11 with an amplitude factor and a background parameter added to account for our imperfect transitions. For each transition, the Rabi frequency depends on the strength of coupling of that transition with the laser. So the frequency of the Rabi oscillations varies in the range 10 kHz to 20 kHz. For $^{138}\mathrm{Ba}^+$, the π-pulse operation transferring the election into the excited state has a fidelity of around $90 - 95\%$.

In $^{137}\mathrm{Ba}^+$, the Rabi frequencies vary much more because of the more complex HF structure involved. At first, many transitions were extremely weak because of the polarization

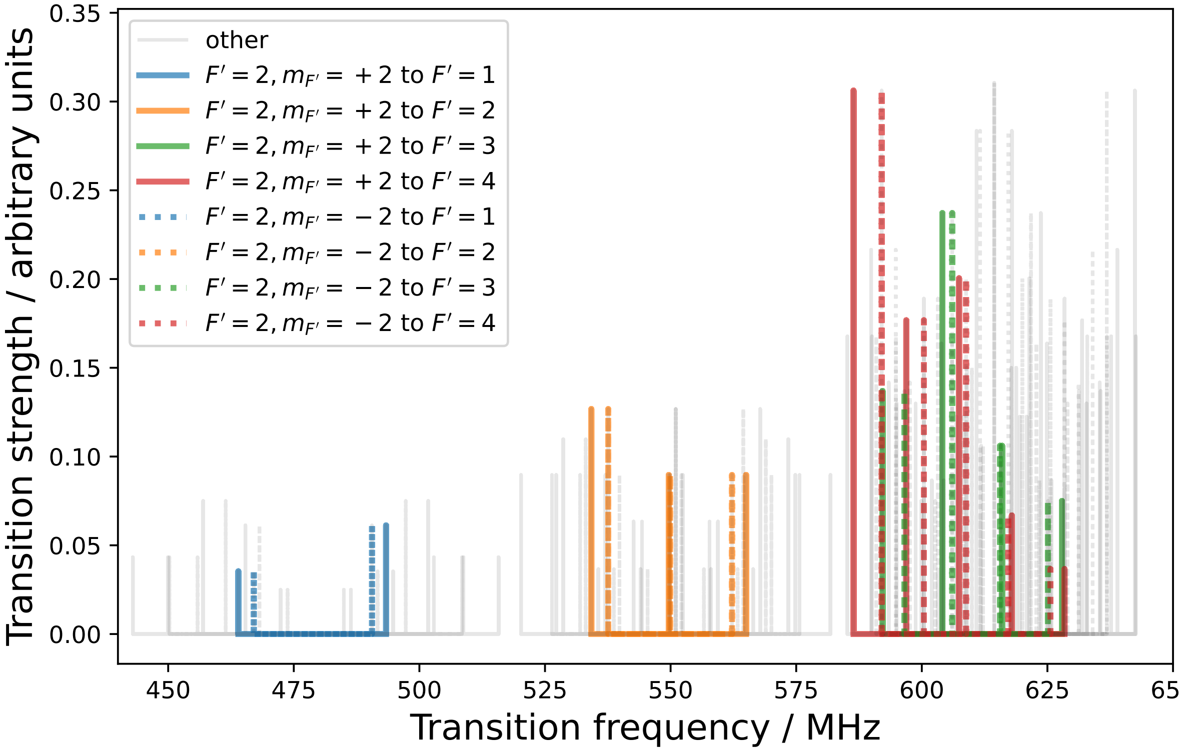

Figure 4.17: Theoretical quadrupole 1762 nm transition frequencies and basic transition strength calculations. Colored transitions are ones which can be driven from our initial state $|S_{1/2}, F = 2, m_F = +2\rangle$ and grey transitions cannot be driven from this state. The solid lines are using a magnetic field of 1.048 mT and the dashed lines are using a magnetic field of 0.835 mT.

being used to drive them (see Figure 4.5). In order to make as many transitions as possible useful, we empirically found a good polarization which keeps as many of these transitions as possible a decent strength. Some of the transitions have a Rabi frequency as low as 2 kHz, while others have frequencies as high as 20 kHz. One of the transitions in particular, the $F' = 3, m_{F'} = 3$ transition, has a Rabi frequency of just 250 Hz as shown in Figure 4.16. This was quite surprising; a basic transition strength calculation predicted it to have the lowest Rabi frequency, but not nearly this low. In fact, all of the $F' = 3$ transitions have weaker transition strengths than the expected strengths shown in Figure 4.17. The reason for the $F' = 3$ states' weak coupling with the laser is because they experience interference with the very close-by $F' = 4$ states. Performing a full analysis of the eigen-states from the Hamiltonian in Equations 4.5, 4.6, 4.7, this interference emerges and the results match well with the measured Rabi frequencies [37, 121].

The π-pulse for most of these transitions can be done with over 90% probability, however some transitions have particularly low fidelities. Transitions with a low Rabi frequency tend to have worse transition fidelities because they take longer to perform a π-pulse and start to fight with the coherence of the ion. It should be noted that in between using the higher magnetic field in Figure 4.15 and the lower magnetic field, we improved the alignment and polarization of the optical pumping, so the fidelities improved quite a lot.

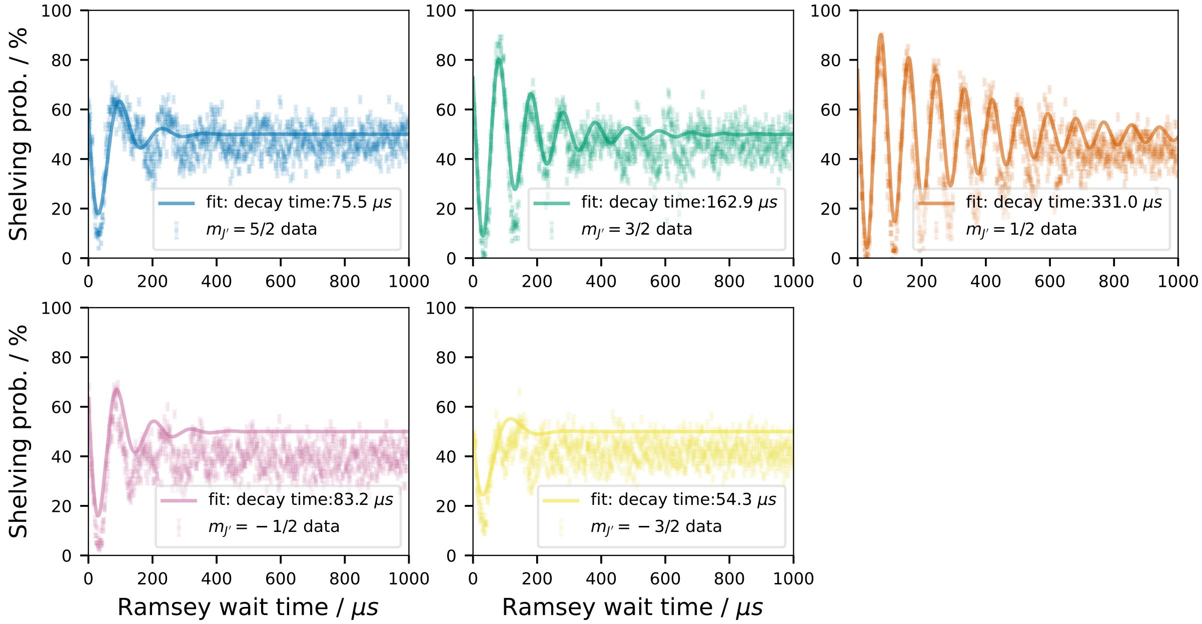

Figure 4.18: Ramsey sequences of all of the $^{138}\mathrm{Ba}^{+}$ quadrupole transitions driven from the ground state $|S_{1/2}, m_J = +1/2\rangle$, varying the wait time in between the two $\pi/2$ pulses. The frequency detuning is set to 3 kHz to 10 kHz red from the carrier frequency and the magnetic field is 1.048 mT.

In order to learn some information about the coherence time of the transitions, some kind of experiment sensitive to the decohering processes is necessary. One of the most common types of coherence experiments is called a Ramsey experiment, described as follows. First, pump the electron into the stretched state using the 493 nm optical pumping laser for 500 µs. Next, apply the 1762 nm laser for an amount of time such that the electron is halfway driven into the excited state, $t = \tau_\pi/2$. This time is determined beforehand by

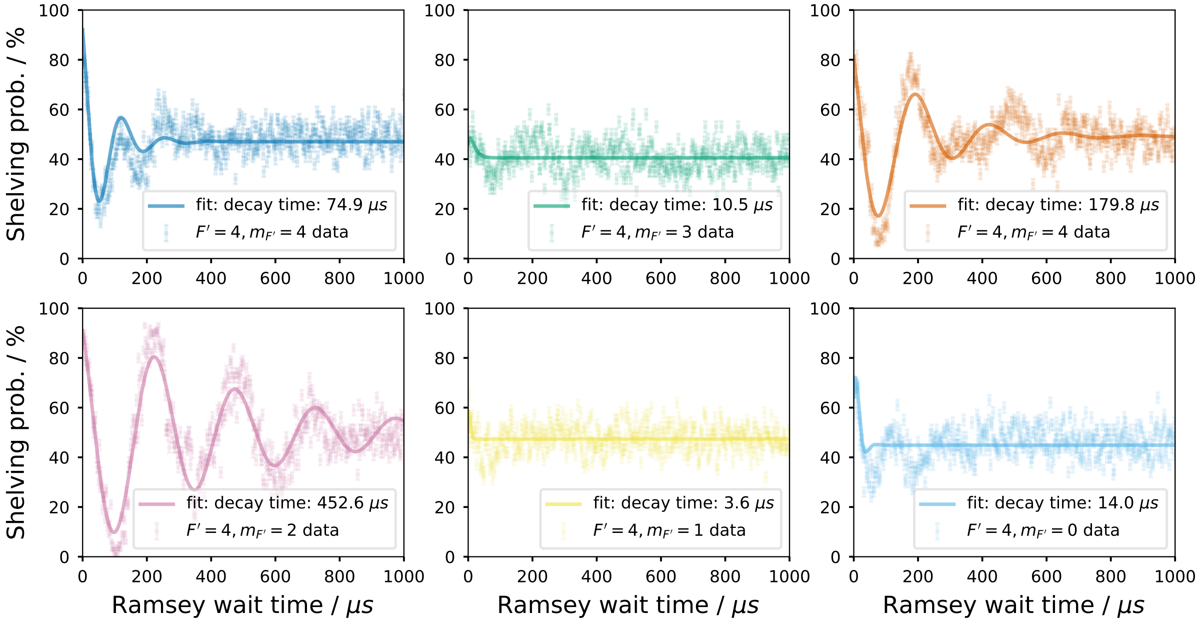

Figure 4.19: Ramsey sequences of the ^{137}Ba$^+$ quadrupole $F' = 4$ transitions driven from the ground state $|S_{1/2}, F = 2, m_J = +2\rangle$, varying the wait time in between the two $\pi/2$ pulses. The frequency detuning is set to 5 kHz red from the carrier frequency and the magnetic field is 0.835 mT.

performing a Rabi oscillation experiment; the τ_π time is then used to determine the correct pulse-time to drive the ion with the 1762 nm laser during the Ramsey experiment. After the electron has been half-way driven into the $D_{5/2}$ state, wait for some amount of time for the electron to decohere. Finally, another $\tau_\pi/2$-pulse is performed. The result of this experiment is that the electron oscillates as the Ramsey wait time is increased, at the same frequency as the laser detuning; These oscillations slowly decay until the overall probability has converged to around 50%. The shelving probability during a Ramsey experiment looks like

$$P_e(t) = 0.5 \sin\left(2\pi\delta t_{wait} + \phi\right) e^{t_{wait}/\tau_{decay}} + 1/2, \tag{4.12}$$

for laser detuning δ, Ramsey wait time t_{wait}, phase ϕ, and decoherence time τ_{decay}.

Ramsey experiments were performed for each transition by first performing a Rabi oscillation experiment to find the $\tau_\pi/2$ time. Ramsey sequences are performed while sweeping the Ramsey wait time, and the results are shown in Figures 4.18, 4.19, 4.20, and 4.21 for both isotopes ^{138}Ba$^+$ and ^{137}Ba$^+$ at 1.048 mT and 0.835 mT magnetic fields respectively,

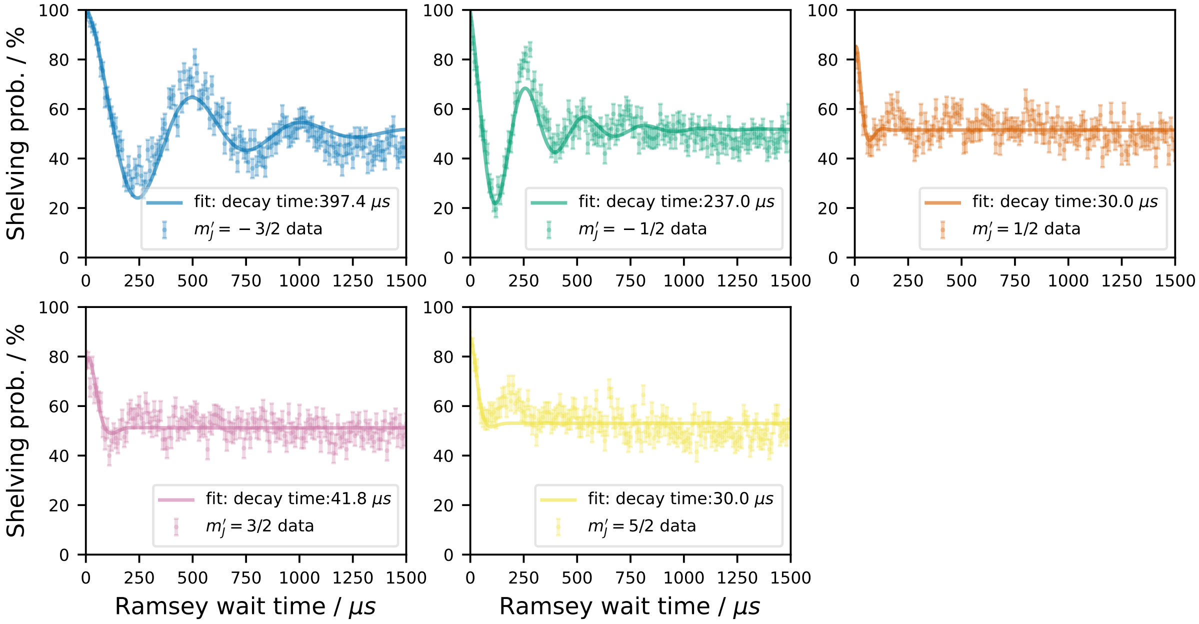

Figure 4.20: Ramsey sequences of all of the ^{138}Ba$^+$ quadrupole transitions driven from the ground state $|S_{1/2}, m_J = +1/2\rangle$, varying the wait time in between the two $\pi/2$ pulses. The frequency detuning is set to 3 kHz to 5 kHz red from the carrier frequency and the magnetic field is 0.423 mT.

and at 0.423 mT magnetic field. The detunings were all set in the range 3 kHz to 10 kHz from the carrier transition frequencies. Each experiment is fit to using Equation 4.12 with the fitting parameters the phase ϕ, the frequency detuning δ, and the decay time τ_{decay}. For transitions which decohere quite quickly, often the fitting was difficult because there are barely any oscillations to fit to. The transitions have coherence times ranging from under 100 µs to as much as 500 µs, depending on how sensitive they are to the magnetic field (see Figures 4.6 and 4.7).

4.2.3 Shelving frequency calibrations

In Section 4.1.2, I described the method we use for finding a single transition. This procedure has been automated, but it still takes on the order of a few minutes to find each transition. So to find all 13 transitions, it takes around half an hour. Since the transitions drift by around 2 kHz d^{-1}, this calibration must be done a lot, often a few times in one

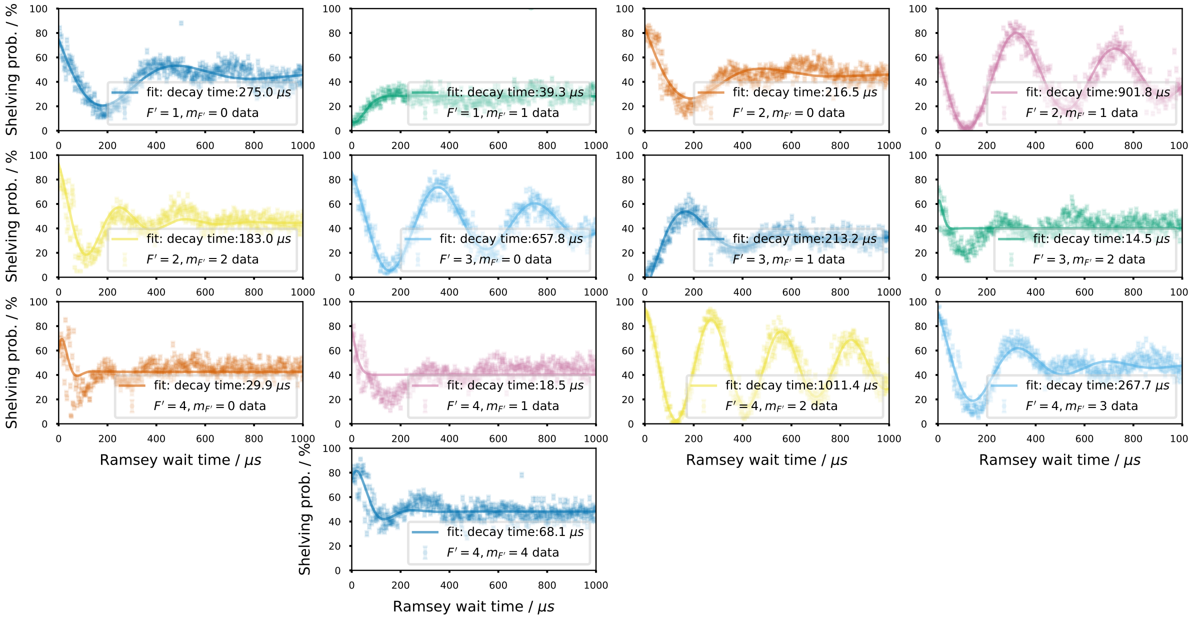

Figure 4.21: Ramsey sequences of all of the ${}^{137}\mathrm{Ba}^{+}$ quadrupole transitions driven from the ground state $|S_{1/2}, F=2, m_F=+2\rangle$, varying the wait time in between the two $\pi/2$ pulses. The frequency detuning is set to 3 kHz red from the carrier frequency and the magnetic field is 0.423 mT.

day. Not only that, but in the time it takes to calibrate, the first calibrated transitions will have drifted some amount.

To reduce the number of transitions we have to calibrate to, we use an interpolation method. The main things in the experiment that can drift are the cavity frequency and the magnetic field. The cavity frequency drift is very linear, as shown in Figure 4.2, and the least magnetic field sensitive transition, $F'=2, m_{F'}=1$, can be picked as the indicator of how much this has drifted. The magnetic field drift changes all of the transition frequencies by different amounts, but the magnitude of the magnetic field drift can be easily estimated by comparing the two most magnetic field sensitive states, $F'=4, m_{F'}=4$ and $F'=4, m_{F'}=0$. The difference of these two frequencies tells us how much the magnetic field has drifted.

So for interpolation, we take a lot of data sets from measuring all of these frequencies over several weeks or months to build the linear interpolation model shown in Figure 4.22. For all transitions other than the three mentioned, we subtract the drift frequency f_{21}, the

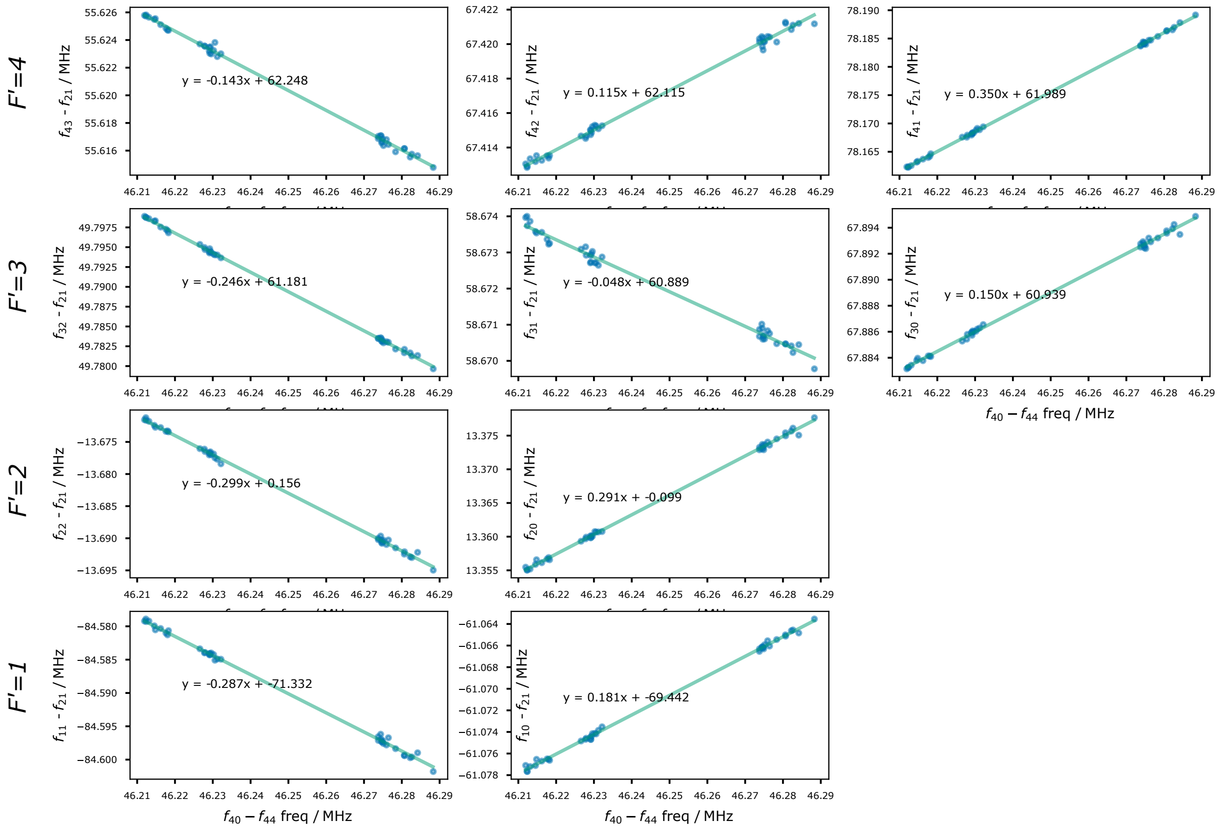

Figure 4.22: Interpolation of the ^{137}Ba^{+} transition frequencies using a set of representative transitions $F' = 2, m_{F'} = 1$, $F' = 4, m_{F'} = 0$, and $F' = 4, m_{F'} = 4$. f_{ij} is the frequency of the $F' = i, m_{F'} = j$ transition. Each row is a different set of F' transitions. The data points are measured frequencies of the different transitions and the lines are linear fits to the data points.

frequency of the least magnetic field sensitive transition, on the y-axis. We compare this to the frequency difference $(f_{40} - f_{44})$ between the two most magnetic field sensitive transitions on the x-axis. This gives a linear relationship which can be fit to in order to get a linear equation which can be used to interpolate the remaining frequencies. During frequency calibration, just measure the three representative transitions, then plug the results into each of the fits shown in Figure 4.22 to get the interpolated frequencies. Looking at the y-axis of the graphs, it's apparent that for all of the transitions, the data points almost never deviate by more than 100 Hz, so the interpolation method should always give frequencies within the kilohertz resolution we use for driving transitions.

4.2.4 Shelving π-time calibrations

To calibrate the π-time of a transition, we perform a Rabi oscillation experiment such as shown in Figure 4.14. A fit is performed using 4.11 to extract the Rabi frequency and the π-time. Typically, this experiment is only done with a time sweep in the vicinity of the previously measured π-time of the transition being measured. Even with this reduction in sweep points, each experiment still takes on the order of a few minutes, similar to the frequency calibrations described in section 4.1.2. An interpolation method similar to that used in Section 4.2.3 could also be employed to find the π-times and reduce this calibration time.

To interpolate the π-times of most transitions, we use the $F' = 4$ transitions as representative transitions for all of the others. Each transition with different $m_{F'}$ will have a different dependence on the intensity of the laser, shown in Figure 4.5. By measuring each level in $F' = 4$, we can see how each of these $m_{F'} \in \{1, 2, 3, 4\}$ is being affected by intensity changes of the driving laser. The interpolation is shown in Figure 4.23 for $^{137}\text{Ba}^+$, with all π-times measured explicitly using a variety of 1762 nm laser powers. Each row is a different set of $m_{F'}$ transitions, with different F', each calibrated with the corresponding $F' = 4, m_{F'}$ transition. The y-axis is the π-time of the interpolated transition and the x-axis is the π-time of its representative $F' = 4'$ transition. Fitting a line to each set of data gives a model which can be used to interpolate the transition π-times after measuring the representative transitions to the $F' = 4$ state.

Most of the interpolations are decent, however you'll notice that the $F' = 3, m_{F'} = 0$ transition is quite bad. The reason for this is because it is two different data sets collected one day apart. In fact, all of the data points in Figure 4.23 consist of data from two separate days. The reason that the two data sets for this transition have different line slopes is because of our frequency calibration. The resolution which we typically use to find transitions is 1 kHz. If the actual transition frequency falls in between the frequency resolution, it's normally not a problem because the main effect is the Rabi frequency might be slightly different. If you measure the Rabi oscillations explicitly, you can find the correct π-pulse time with no problems. However, this interpolation method assumes that the exact transition frequencies have been found. If the frequencies used for the π-pulse calibration are detuned by different amounts, then they will have a different slope in the interpolation curves.

This means that even if we collected the data on the same day, with the same frequency

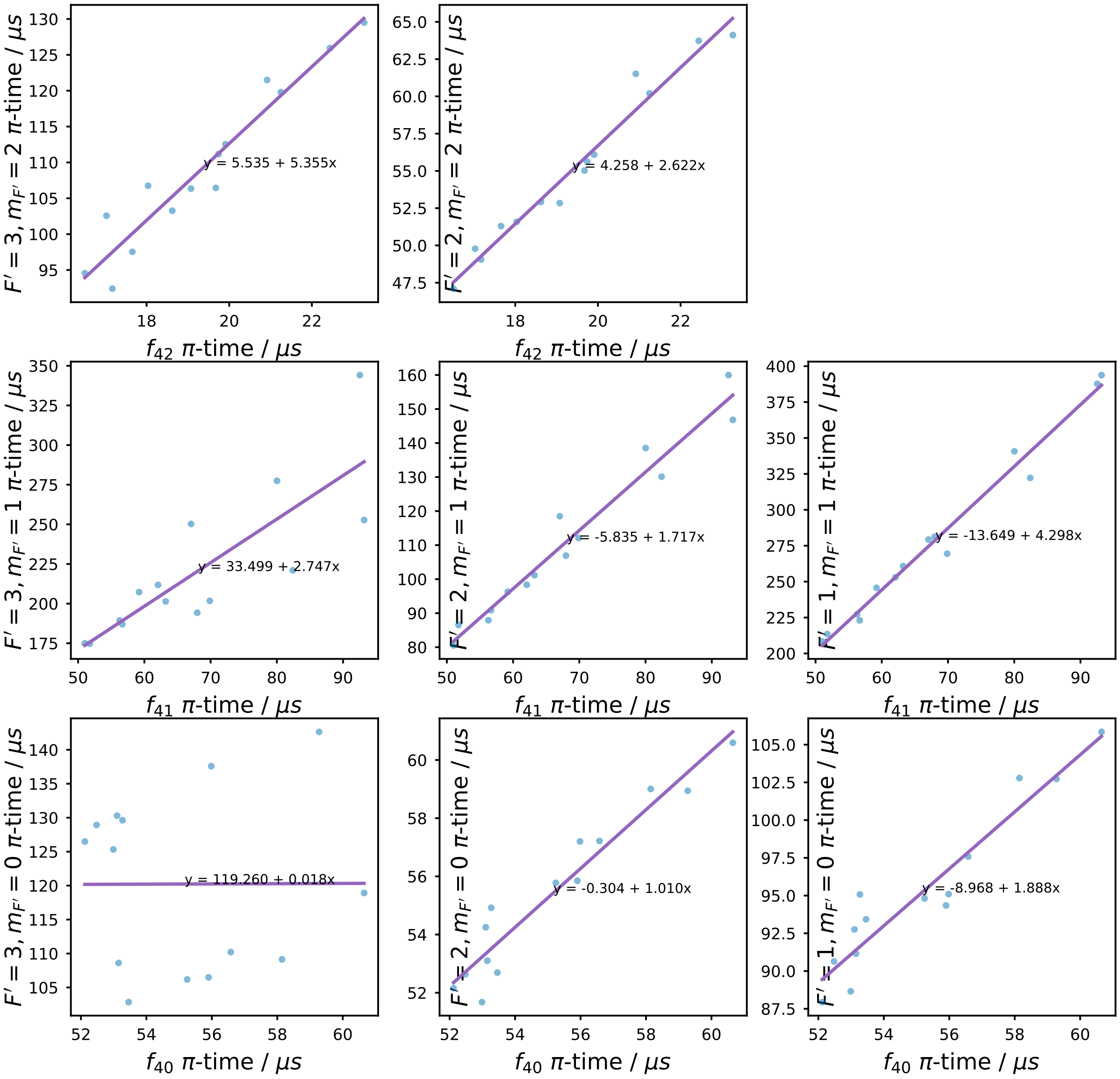

Figure 4.23: Interpolation of the $^{137}\mathrm{Ba}^{+}$ π-times using a set of representative transitions. Each row is a different set of $m_{F'}$ transitions, with different $F' \in \{1, 2, 3\}$, each calibrated with their corresponding $F' = 4, m_{F'}$ transition. The data points are measured π-times of the different transitions and the lines are linear fits to the data points.

detuning from the carrier, the interpolation still wouldn't work. The calibration frequencies measured day-to-day could also be detuned from the correct transition based on the resolution of our frequency calibration. Overall, this can lead to errors in the π-pulse interpolation which are up to a few percent in π-pulse fidelity. This interpolation method would work fine if we used a better resolution to find our transition frequencies.

4.3 Qudit measurements

4.3.1 Qudit SPAM experiment

With all of this characterization out of the way, now is the time to use this quadrupole transition for something useful! The shelving metastable $D_{5/2}$ state in barium is interesting mainly because it has such a long lifetime (35 s), even compared with the $D_{5/2}$ states of other ions typically used for quantum information. This long-lived state can be used to store, or shelve, quantum information. This has been used to perform qubit SPAM with the best fidelity to-date, using the $^{137}\mathrm{Ba}^+$ isotope to achieve (1×10^{-4}) error SPAM. This state has many more levels to utilize, and can be used to store qudit states in order to discriminate between them during measurement.

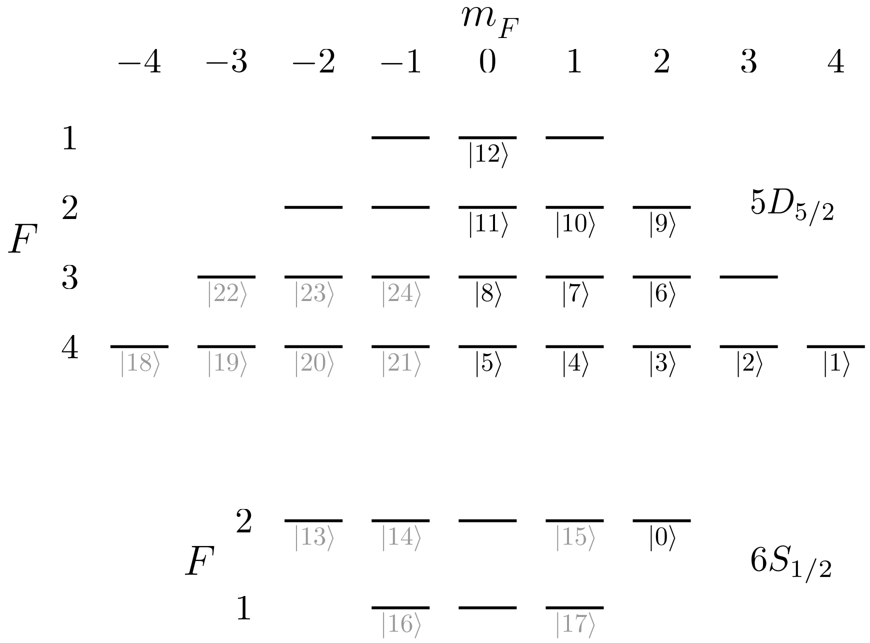

Figure 4.24: The energy levels used to encode our 13-level qudit. The upper states are metastable, and we use the 1762 nm laser to address them. Grey states could be used in the future as more qudit levels.

For constructing qudits, the obvious choice of states is to pick the ones which have the best π-pulse transition fidelities first. This is how we chose our qudit states, shown in Figure 4.24 for the 13-level qudit. For now, we have results for a 13-level qubit, but we are certainly not limited to using just 13 levels. With some method of moving the electron population to different ground HF states, using most of the other energy levels in the $D_{5/2}$ state (which are currently inaccessible from the current initialized $|F=2, m_F=2\rangle$ state by quadrupole selection rules, Equation 4.1) would be possible. The greyed out states are ones which could be used in the future to construct up to a 24-level qudit. The reason more of the 32 total states (24 in the $D_5/2$ and 8 in the $S_{1/2}$) can't be used is because for the measurement procedure, all but one of the states in the ground level must be shelved.

For the 3-level qutrit, we used the ^{138}Ba$^+$ isotope's $\{|m_{J'}=3/2\rangle, |m_{J'}=1/2\rangle\}$ excited states along with the stretch state we pump to, $|m_J=1/2\rangle$. The 6-level qudit also uses the ^{138}Ba$^+$ isotope, this time utilizing all of the metastable states along with the stretch ground state as its computational space.

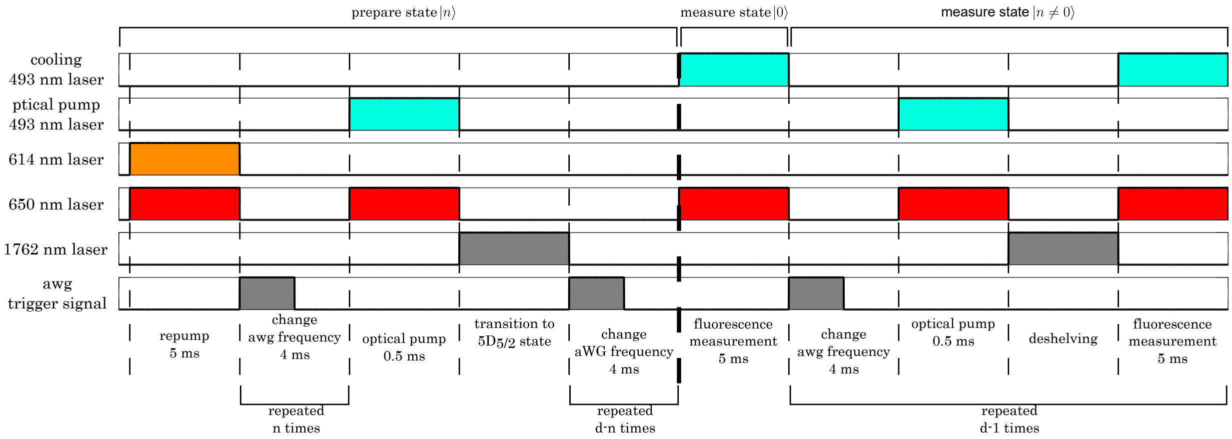

Figure 4.25: Pulse sequence for performing SPAM experiment. The left side is the preparation stage, where the ion is initialized in $|n\rangle$. The right side is the measurement stage, where states are shuttled back and forth from the $D_{5/2}$ state and measured.

The SPAM process is exactly like the qubit measurement which was illustrated earlier in Chapter 2, Figure 2.6. The only difference is that shelving and de-shelving is done to more states, measuring fluorescence between each step to find the computational state of the qudit. A pulse diagram of the procedure is shown in Figure 4.25.

1. First, the ion is initialized in the ground state by flushing all of the metastable states using the 650 nm and 614 nm lasers.

2. Next, the ion is prepared in the stretch $|F=2, m_F=2\rangle$ state of the ground state using the optical pumping beam.

3. Drive a π-pulse quadrupole transition into the prepared $|n\rangle$ state. With the ion in a desired prepared state $|n\rangle$, the state preparation stage is complete and we move on to the measurement.
4. To measure the qudit, start off by measuring the state that was initially left in the ground state, $|0\rangle$.
5. Next, repeatedly shuttle the qudit state $|n\rangle$ in the metastable state back into the ground state by a π-pulse and measure using fluorescence.
6. The SPAM procedure concludes when all of the computational states are read out.

In our experiment, we have some artificial limitations which are caused by the specific AWG we are using. The AWG is triggered to move on to the next waveform in the pipeline, however the AWG waits until the current waveform has finished before moving on to the next waveform. For this reason, we are forced to wait for several milliseconds every time we move to the next waveform. In addition, we are limited by memory space which allows for on the order of 10-20 waveforms to be programmed onto the AWG at a time. This is set by the fact that we need kilohertz resolution on the frequencies of our waveforms.

4.3.2 Qudit SPAM results

		Meas. $\vert n\rangle$		
		$\vert 0\rangle$	$\vert 1\rangle$	$\vert 2\rangle$
Prep. $\vert n\rangle$	$\vert 0\rangle$	***100.00***	2.20	0.20
	$\vert 1\rangle$	2.10	***96.70***	2.50
	$\vert 2\rangle$	2.10	0.00	***96.90***

		Meas. $\vert n\rangle$		
		$\vert 0\rangle$	$\vert 1\rangle$	$\vert 2\rangle$
Prep. $\vert n\rangle$	$\vert 0\rangle$	***100.00***	2.20	0.20
	$\vert 1\rangle$	2.18	***97.82***	0.00
	$\vert 2\rangle$	2.12	0.00	***97.88***

Table 4.4: 3-level qutrit SPAM results using $^{138}\mathrm{Ba}^{+}$. The left shows which qudit state $|n\rangle$ was prepared while top shows which qudit state $|n\rangle$ was measured. The diagonal entries are successes in the SPAM. The left table shows the raw results from the experiment. Experiments with no bright state detected, and fluorescence after the first bright state are included. The right table shows post-selected results: experiments with no bright state detected are thrown out because obviously something went wrong. Only the first bright state is considered to be the measured state.

Table 4.4 shows our results for a three-level qutrit SPAM experiment. The table on the left are the raw fidelities obtained from preparing and measuring each state. The diagonal values are the probabilities of successfully preparing and measuring that state, and our qutrit has fidelities all over 96%. The $|0\rangle$ state in these SPAM experiments almost always has near 100% fidelity because it is the optically pumped state which is measured first and never experiences any shelving or de-shelving procedures.

There are a few things wrong with this analysis though. First, there are many experiments in which the ion was never measured to be in the bright state. This can happen because we essentially failed to de-shelve the state which was prepared, leaving it in the excited state for the whole measurement. In post-processing, we can catch these errors, and so we can simply get rid of the runs where this occurred.

Second, the ion can be measured more than once. This happens because after the ion was measured to be in state $|n\rangle$, the subsequent de-shelving process for measuring the next state is supposed to essentially re-shelve the just measured state. If this fails, the ion stays in the ground state and we measure fluorescence again until it is successfully re-shelved. Again, this error is obvious when analyzing the data, and so we can correct for this by making the first measured state be the only measured state no matter what. This interpretation makes sense for overall qudit experiments as well, because when making an overall qudit measurement, we only really care about the first state we measure. After that point, all quantum information is lost, and the experiment is already over.

The right Table in 4.4 shows the results of this post-selection, and the fidelities have improved significantly to nearly 98% fidelity for the two shelved qudit states.

		Meas. $\|n\rangle$					
		$\|0\rangle$	$\|1\rangle$	$\|2\rangle$	$\|3\rangle$	$\|4\rangle$	$\|5\rangle$
Prep. $\|n\rangle$	$\|0\rangle$	***100.00***	0.00	0.00	0.00	0.00	0.00
	$\|1\rangle$	10.51	***89.37***	0.12	0.00	0.00	0.00
	$\|2\rangle$	6.39	0.00	***93.39***	0.00	0.11	0.11
	$\|3\rangle$	4.03	0.00	0.00	***95.97***	0.00	0.00
	$\|4\rangle$	6.47	0.00	0.00	0.11	***93.42***	0.00
	$\|5\rangle$	8.25	0.00	0.00	0.00	0.10	***91.65***

Table 4.5: 6-level qudit SPAM post-selected results using $^{138}\mathrm{Ba}^{+}$. The left shows which qudit state $|n\rangle$ was prepared while top shows which qudit state $|n\rangle$ was measured. The diagonal entries are successes in the SPAM.

The 6-level qudit SPAM experiment, also using $^{138}\mathrm{Ba}^{+}$, is presented in Table 4.5. This time, only the post-selected results are shown, and the results are a qudit with around

		Meas. $\lvert n\rangle$												
		$\lvert 0\rangle$	$\lvert 1\rangle$	$\lvert 2\rangle$	$\lvert 3\rangle$	$\lvert 4\rangle$	$\lvert 5\rangle$	$\lvert 6\rangle$	$\lvert 7\rangle$	$\lvert 8\rangle$	$\lvert 9\rangle$	$\lvert 10\rangle$	$\lvert 11\rangle$	$\lvert 12\rangle$
Prep. $\lvert n\rangle$	$\lvert 0\rangle$	***100***	0	0	0	0	0	0	0	0	0	0	0	0
	$\lvert 1\rangle$	6.78	***93.22***	0	0	0	0	0	0	0	0	0	0	0
	$\lvert 2\rangle$	3.81	0.11	***95.76***	0.11	0	0	0.21	0	0	0	0	0	0
	$\lvert 3\rangle$	2.98	0	0	***97.02***	0	0	0	0	0	0	0	0	0
	$\lvert 4\rangle$	4.8	0	0	0	***94.98***	0	0	0	0.22	0	0	0	0
	$\lvert 5\rangle$	11.11	0.14	0	0	0	***88.61***	0	0	0	0.14	0	0	0
	$\lvert 6\rangle$	31.95	0.13	0.27	0.13	0.27	0	***66.44***	0.27	0.13	0.13	0	0.13	0.13
	$\lvert 7\rangle$	6.37	0	0.23	0	0	0.11	0.46	***92.83***	0	0	0	0	0
	$\lvert 8\rangle$	8.17	0	0	0.12	0	0	0.24	0	***91.35***	0	0	0.12	0
	$\lvert 9\rangle$	13.9	0.24	0	0.35	0.12	0.35	0.35	0.24	0.12	***83.51***	0.71	0	0.12
	$\lvert 10\rangle$	2.91	0.11	0.22	0	0.11	0.34	0.34	0.11	0	0.22	***95.4***	0	0.22
	$\lvert 11\rangle$	3.77	0	0.33	0.11	0.11	0	0.11	0.33	0	0.44	0	***94.67***	0.11
	$\lvert 12\rangle$	4.12	0.1	0	0	0	0	0	0	0	0	0	0	***95.78***

Table 4.6: 13-level qudit SPAM post-selected results using $^{137}\mathrm{Ba}^+$. The left shows which qudit state $\lvert n\rangle$ was prepared while top shows which qudit state $\lvert n\rangle$ was measured. The diagonal entries are successes in the SPAM.

94% fidelity. The $\lvert 1\rangle$ and $\lvert 5\rangle$ states are particularly bad, bringing the overall fidelity down quite a lot. These are the two most magnetic field sensitive transitions in $^{138}\mathrm{Ba}^+$ from our initial state to $m_{J'} = -3/2$ and $m_{J'} = 5/2$ in the shelving state.

Finally, we present the results of our 13-level qudit SPAM experiment using $^{137}\mathrm{Ba}^+$ in Table 4.6. Most transitions actually have fidelities of better than 90%, with only three of them being worse. One of them in particular was really bad, with a fidelity of 66%. This qudit state, $\lvert F' = 3, m_{F'} = 2\rangle$, has a particularly weak transition strength and somewhat large magnetic field sensitivity, giving it a low fidelity. Overall, our average 13-level qudit fidelity is 91.7%.

It should be noted that for all of the coherent quadrupole operations and overall SPAM results presented here, NO measures have been taken to mitigate magnetic field noise, one of the largest sources for error in quantum experiments [47–49] (see Chapter 5). The fact that our transitions are as coherent as they are without any of these precautions is quite a surprising result, and indicates that using these transitions for qudits will not be as difficult as imagined.

Figure 4.26 shows what our qudit SPAM fidelities would look like if we limited our computational space instead of using 13-levels. It shows what the overall fidelity of a d-level qudit is, where we use the fidelities of the 13-level SPAM experiment already presented in Table 4.6. The levels are added for each d-level qudit based on which ones have the best fidelities. In doing this, we end up with an overall decrease in qudit fidelity as

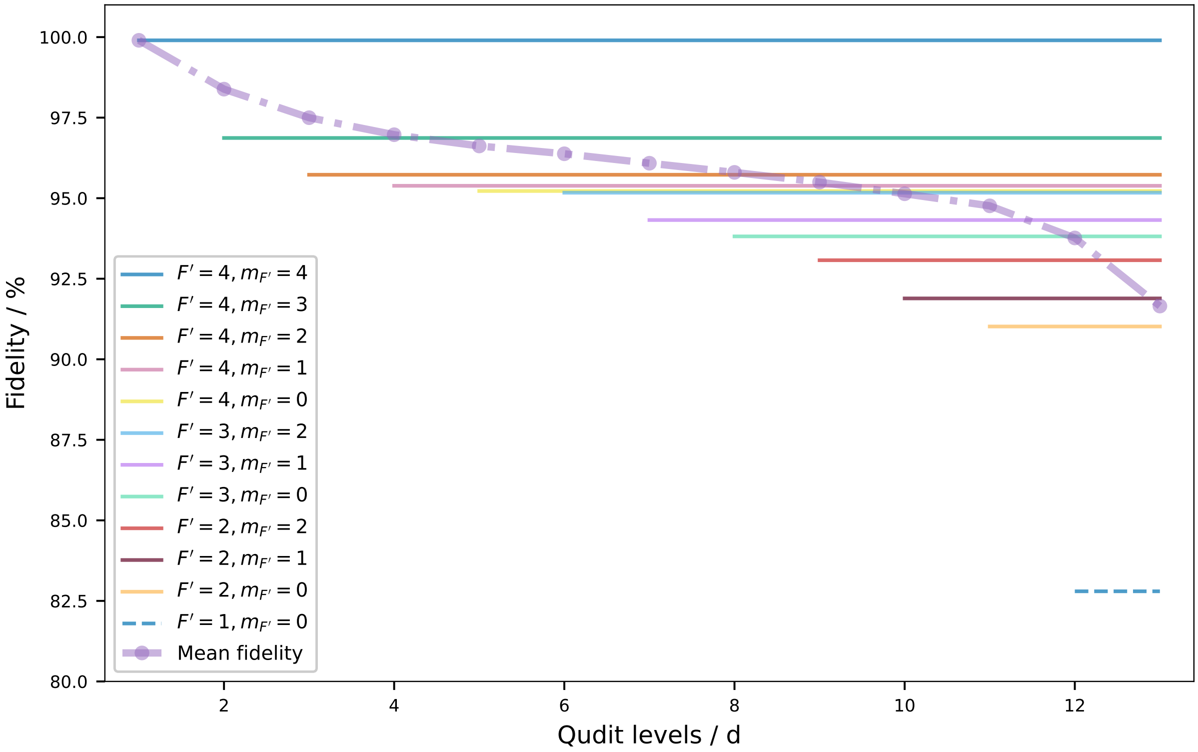

Figure 4.26: Averaged overall SPAM fidelities for different d-level qudits, where the results from Table 4.6 are used, picking the best transitions first. The horizontal lines show the SPAM fidelities for each individual transition (their respective diagonal value from Table 4.6).

we increase d. However, this choice could have been made differently to manufacture a completely opposite scaling, so that qudit SPAM fidelity actually increases with dimension (see References [37,121]). This fact just illustrates that at the level of errors we're currently at, the fidelity of qudit SPAM doesn't depend on the qudit level, but the fidelities of the particular transitions we choose to use.

Chapter 5

Magnetic Field Noise

In this Chapter, I discuss using both an AC-line noise compensation method, and permanent magnets, to mitigate magnetic field noise. First, I talk about general magnetic field noise in trapped ions and how it can cause decoherence. I discuss why we believe this to be the main source of error in our system as well, using the shelving results presented in the previous chapter. An AC-line noise compensation method is presented, with initial results indicating that this may not be the main magnetic field noise error source in our system. The other possible source is noise from the current source used to drive our magnetic field coils, and a method to mitigate this by switching to permanent magnets is shown. We have designed a permanent magnet setup which we will install in the trap to hopefully increase the coherence times in our ions.

5.1 Magnetic field noise - background

Many groups have found magnetic field noise to be one of the most significant sources of noise in coherent operations [47–49, 198]. For some experiments, this can be mitigated by choosing to use a specific set of states which are to first-order insensitive to the magnetic field magnitude. In qubits, using ions with simpler energy structure such as nuclear spin $I = 1/2$ ions, this can be very simple, with the two clock states ($m = 0$) of the HF $F \in \{0, 1\}$ being naturally magnetic field insensitive. For more complicated ions, with $I > 1/2$, these states exist as well, however magnetic field sensitive operations such as the quadrupole transition must be used to achieve certain operations such as measurement (see Chapter 4). For Zeeman qubits [48] and in our specific case, qudits, there is no option to pick states and operations which are completely magnetic field insensitive. In fact in qudits, each state and operation can have completely different sensitivity to the magnetic field, as shown in the previous chapter.

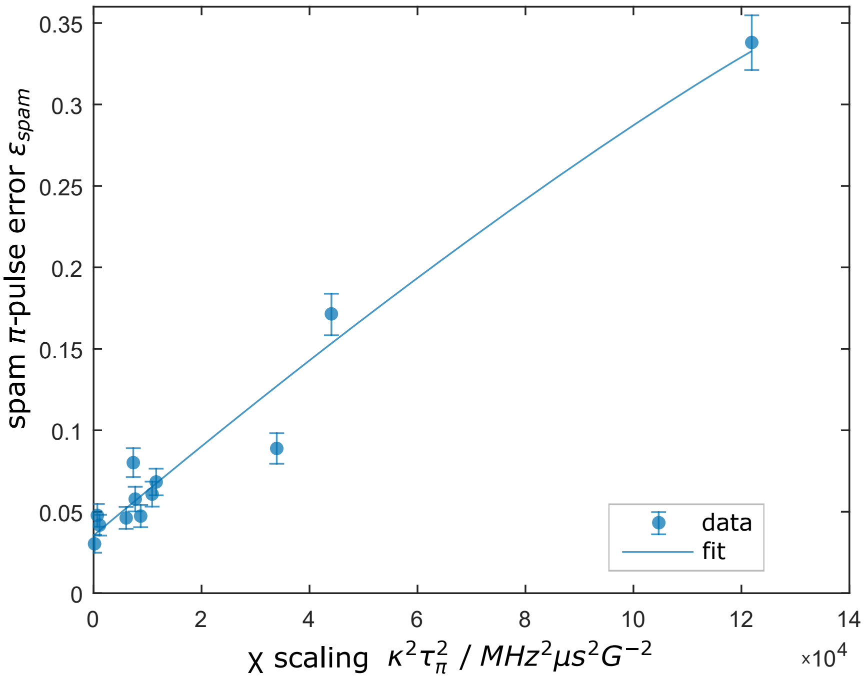

Figure 5.1: SPAM fidelity vs magnetic field noise and π-time parameter. The data points are from the 13-level SPAM experiment presented in Section 4.3. The data is fit to the relationship of Equations 5.1 and 5.2, with the y-intercept and the amplitude of χ used as fitting parameters.

When a magnetic field sensitive transition experiences magnetic field noise, the energy levels jitter around the nominal energy. In practice, this energy jittering manifests as a broader transition linewidth and a lower coherence. In our measurement experiments, we found that the transitions most sensitive to the magnetic field noise were the ones which performed worst in terms of π-pulse fidelity. This shows that magnetic field noise, as expected, is probably the main source of error in our shelving experiments. We used this hint to investigate further and find a theoretical correlation. Using filter-function theory [37, 121, 199, 200], we were able to find how these are correlated. The error in performing a π pulse can be written as

$$\epsilon_\pi = \frac{1}{2}\left(1 - e^{-\chi}\right), \tag{5.1}$$

where χ is some error parameter; in filter-function theory, this is the overlap of the transition spectrum to the frequency noise power spectral density. Assuming that the magnetic field noise is a $1/f$ noise source with a peak present at the AC frequency, we can show that χ scales with both κ, the magnetic field sensitivity of the transition, and τ_π, the π-time of the transition, in second order [37, 121]:

$$\chi \propto \kappa^2 \tau_\pi^2. \tag{5.2}$$

This scaling is shown in Figure 5.1, fit to the actual fidelities found for all of the quadrupole transitions measured in Chapter 4. The fit shows agreement with our transitions, and is indication that this noise from magnetic field noise, specifically AC-line noise, is one of the major sources of error for driving our quadrupole transitions. The fit y-intercept parameter of 4% suggests the amount of error from sources other than magnetic field noise modeled here. We estimate that parameter drifts (of π-time or frequency) and imperfect state-preparation polarization are the next biggest error sources.

So magnetic field noise is, unsurprisingly, our biggest source of error in using the 1762 nm laser to perform coherent operations and SPAM measurement. While the fidelities we were able to achieve with no mitigation of magnetic field noise were surprisingly high, we want to improve them further for future qudit experiments. A common way of dealing with magnetic field noise is to surround the vacuum chamber with μ-metal to shield it from stray magnetic fields [47, 48, 201]. The problem with this method is that it is difficult to retroactively install it around a chamber; it should be planned for in the chamber design phase. You can also use permanent magnets to generate the quantization magnetic field. Permanent magnets reduces error compared to magnetic field coils because they require no current source, which can produce a noisy magnetic field. Typically, AC-line noise is a major part of the magnetic field noise. A common way of getting around AC-line noise is to simply trigger your experiments off of the wall [202], so that a short experiment always happens within the same small part of the AC-line time period. This can be quite slow, since you have to wait in between experiments for the next cycle of the wall AC signal, limiting an experiment's duty cycle to be on the order of milliseconds. Alternatively, the AC-line noise can be compensated for either actively or passively by essentially canceling it out [203–206].

5.2 AC-Line noise compensation

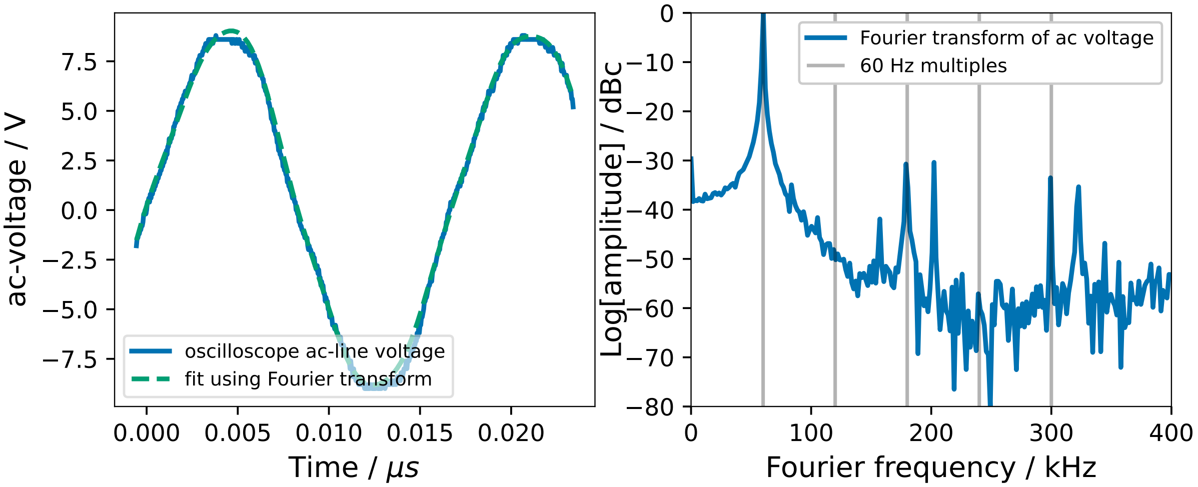

Figure 5.2: Measurement of the AC voltage directly from the wall. (a) A time-series of the voltage, regulated down from 120 V to ~ 8 V. (b) A Fourier transform of the time series on a log scale relative to the 60 Hz component. Vertical lines correspond to multiples of this main 60 Hz frequency.

The major component of the noise model presented earlier is AC-line noise. This noise comes from the AC power from the wall being used to power most devices in the lab. The AC running around the room is a bunch of moving charges, and thus they generate magnetic fields which permeate in the room. A parasitic magnetic field shows up at the trap center and can add constructively and destructively to the quantization magnetic field being applied to the ion. The changing magnetic field causes the electronic transitions to change frequency and reduces the coherence of these transitions. Magnetic field fluctuations of this sort are correlated almost exactly with the AC line noise.

Figure 5.2(a) shows the AC voltage measured from the wall as a function of time. This data was collected by using a transformer to reduce it from 120 V to around 8 V and measuring the voltage using an oscilloscope. In Canada, where our lab is located, the AC power is delivered at 60 Hz and power grid is designed so that it absolutely never deviates by more than 0.5 Hz, and typically operates within 0.2 Hz of the base frequency. The true AC-power signal has many other frequency components which should mostly include harmonics of the base 60 Hz frequency. The overall signal of the AC-line voltage can be

Frequency (Hz)	Amplitude	Phase (rad)
60	1.00000	-0.03
180	0.02912	-2.98
202	0.03028	1.37
300	0.02110	2.10
323	0.01710	2.50

Table 5.1: The Fourier components of AC-line voltage. Amplitudes were obtained from taking the Fourier transform of Figure 5.2(a), and phases were obtained by fitting the Fourier components to this data (fit shown in Figure 5.2(a).)

estimated as a superposition of many these frequency components:

$$V = \sum_{n=1}^{N} A_n \sin\left(2\pi f_n t + \phi_n\right), \tag{5.3}$$

where f_n are the frequencies of the different components, t is time, and ϕ_n is the phase of the different components. Figure 5.2(b) shows the frequency components of the AC voltage on a log scale relative to the highest amplitude at 60 Hz. Here, the units are $dBc = 20\log\left(\frac{A}{A_{60}}\right)$. These Fourier components were then used to fit to the AC voltage, with the results shown in Table 5.1. Other measurements of AC voltage showed that the odd harmonics of the mains frequency have a large amplitude component [205, 206]. We also see that the odd multiples are strongest, however we found that our components are weaker than the other measurements [205,206], and we have additional peaks at the strange frequencies 202 Hz and 323 Hz. The other experiments are in other countries, with entirely different electrical grids, so it's not surprising that our AC line voltages have different characteristics. The differences could be coming from their different AC characteristics (different frequency, higher voltage, etc.), power stations, the features of the transmission lines, or even from the power supply line in the buildings we are using. The fact that our main 60 Hz component is nearly two orders of magnitude stronger than other components should make it much easier for us to compensate for it.

To compensate for any AC-line noise that could be coming from the wall and devices near the chamber, all that needs to be done is to create an equal and opposite magnetic field which can destructively interfere with it. This compensation field need only cancel out the magnetic field in the direction of the main magnetic field, since perpendicular components will only perturb the direction of the overall field slightly. Magnetic field noise in directions other than the quantization field direction only influence the overall magnetic field to second order, whereas the magnetic field noise in the direction of the quantization axis influences it to first order. Several groups have been able to perform this compensation, and the results can be quite dramatic, with at least an order of magnitude improvement in coherence being reported [203,205,206], and coherence times being on the order of 10 µs for magnetic field sensitive transitions. However, these groups had higher original transition linewidths of around 4 kHz compared to our linewidths of 1.46 kHz (see Figure 4.11). Thus, we don't expect to see as dramatic an improvement in coherence, but it should still lead to improved fidelities and perhaps result in more of the 1762 nm transitions being useful.

5.2.1 Compensation experiment

The linewidths of most of the 1762 nm quadrupole transitions are on the order of 1 kHz to 2 kHz, as shown in Figure 4.11. This $F' = 4, m_{F'} = 4$ transition in $^{137}\mathrm{Ba}^+$ has a magnetic field sensitivity of $-1.55\,\mathrm{MHz/G} = -15.5\,\mathrm{MHz\,mT^{-1}}$, which is fairly average compared to the other transition sensitivities, and it is broadened to around 1.46 kHz. Comparing the sensitivity to the linewidth of the transition, we get an estimated magnetic field noise of

$$B_{noise} = \frac{1.46\,\mathrm{kHz}}{15.5\,\mathrm{MHz\,mT^{-1}}} \approx 100\,\mathrm{nT}. \tag{5.4}$$

This is the amount of magnetic field noise required to broaden the transition by the amount we see in this transition, 1.46 kHz, and the amount of magnetic field we will need to produce in our compensating coil to cancel this noise out (assuming AC-line noise is the major source for this broadening).

We can use the empirical values from our quantization magnetic field to come up with a current required to generate this compensating magnetic field using our existing magnetic field coils. In our normal experiments, we often use a magnetic field current of 4 A on just one of the coils, which generates an estimated magnetic field of 0.423 mT. To make a magnetic field of 100 nT using an equivalent coil requires

$$I = \frac{4\,\mathrm{A}}{0.423\,\mathrm{mT}} \cdot 100\,\mathrm{nT} = 1\,\mathrm{mA} \tag{5.5}$$

of current. The resistance in our magnetic field coil is $R = 0.8\,\Omega$, so this corresponds to a voltage of $V_{comp} = IR = 0.8\,\Omega \cdot 1\,\mathrm{mA} = 0.8\,\mathrm{mV}$.

To generate the compensating magnetic field, we use a DS345 [207] function generator. This device has the ability to produce arbitrary waveforms, but because the 60 Hz signal is

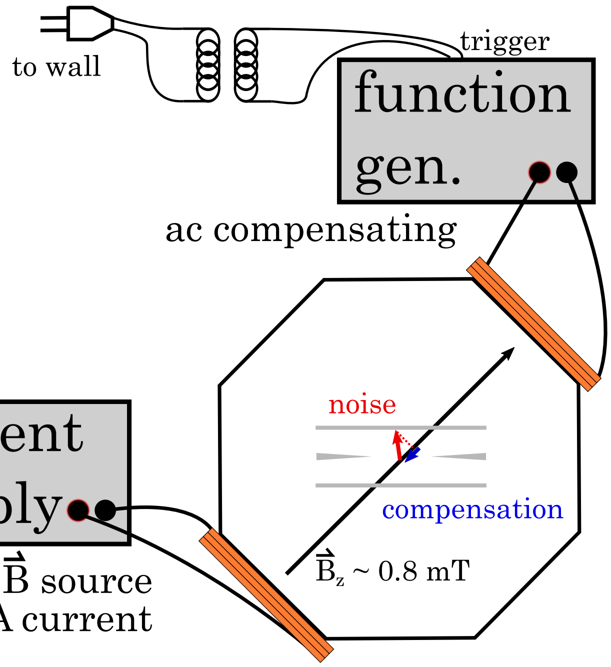

Figure 5.3: Setup for compensating for AC-line noise. One magnetic field coil is used to generate the main magnetic field, while the opposite coil is used to provide the compensation magnetic field. A transformer is used to bring the AC voltage down to ∼ 8 V to trigger the frequency generator to send a single pulse of the compensation signal with a specific phase and amplitude.

so much stronger than the rest, we use the simpler pulsed sine wave function. This allows us to output a single 60 Hz frequency of set amplitude and phase on a trigger.

To trigger the signal generator, we first regulate the voltage from the wall down to 8 V using a simple power supply. To isolate the trigger voltage from the wall, we use an transformer stage with no voltage change, just to prevent an electrical short of any kind and to avoid ground loops which could effect the triggering. This is the signal shown in Figure 5.2, and AC-line harmonics shown in Table 5.1. One problem we encountered with this particular function generator is that once a sine wave pulse has been triggered, it must complete before the device can accept another trigger. The result was that the pulsing would very often skip pulses because it was still in the middle of a previous pulse when the next line trigger came in. This happens when the frequency of the AC power is higher than the set 60 Hz pulse. To solve this, we use a slightly larger frequency of 60.3 Hz as our compensating signal. The compensating magnetic field will not perfectly match up with the noise, but it is certainly close enough to compensate most of the noise.

The minimum output of our function generator is 10 mV, which is higher than the estimated 0.8 mV needed to compensate for the AC-line noise. To reduce the voltage further and also to ensure that the device can never apply too much voltage directly to the coil, we attenuate the output by 30 dB using an RF attenuator, reducing the power by a factor of around 1000 and the voltage by a factor of around $\sqrt{1000}$, so the output needed to compensate should be 25 mV.

To quantify the magnetic field compensation, we use the decay time of the transition as the metric. This is measured by performing a Ramsey scan, where we perform a half π-pulse to put the ion in a superposition, wait some time, then perform another half π-pulse. This experiment reveals information about how long it takes superpositions to decohere, and is a good measure of how well our compensation is performing. To measure the decay time from compensation using a specific set of parameters, a full Ramsey sequence is performed and the data is fit to using Equation 4.12 to get the estimated decay time of the experiment. We choose to use the $|m_J = 1/2\rangle \leftrightarrow |m_{J'} = 1/2\rangle$ transition of $^{138}\mathrm{Ba}^+$ because this isotope is faster to load and this transition has a high transition strength, and a relatively high magnetic field sensitivity. The magnetic field noise will be stronger, but the transition will still be fast enough to be coherent for many oscillations. Before each set of experiments, the frequency and the π-time are calibrated. The frequency is set to 3 kHz higher than the calibrated transition and the pulse time is set to $\tau_\pi/2 \approx 11\,\mu\mathrm{s}$ to $13\,\mu\mathrm{s}$.

We expect that if the compensation voltage is significantly too small, the coherence time will be barely improved for only around half of the phase range. This means that the compensation is working, but the amplitude is not nearly enough to cancel out the noise. If the voltage is too high, we should still see some amount of improvement in the coherence. However, if we increase to more than double the correct voltage, all phases should only make the coherence worse than with no compensation. With such a high amplitude, even if the signal is at the correct phase, the compensation field will completely cancel the magnetic field noise with two times the magnitude needed, essentially just reversing the phase and increasing the magnetic field noise.

5.2.2 Compensation experiment results

Initially, we were unable to see any effect of the compensation using the amplitude we estimated previously of 25 mV, for different phases. We had to increase the voltage all the way up to 600 mV and higher to see any appreciable difference compared to no compensation. Figure 5.4 shows how the Ramsey decay time depends on the phase of the compensating

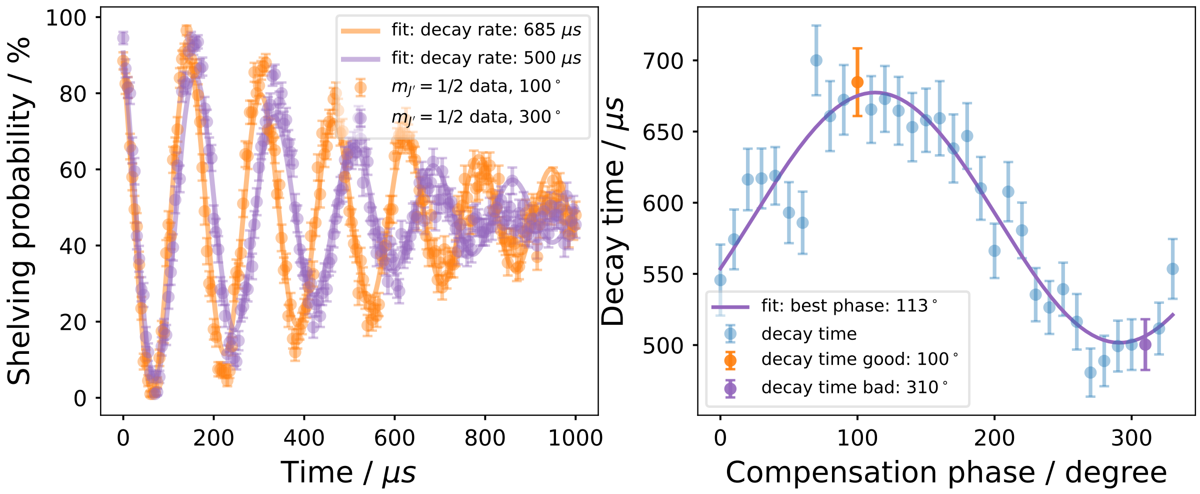

Figure 5.4: Compensation of AC-line noise using 600 mV for different phases. Ramsey sequences are performed on the $|m_J = 1/2\rangle \leftrightarrow |m_{J'} = 1/2\rangle$ transition in $^{138}\mathrm{Ba}^+$. (a) Ramsey sequences of two of the data points in (b). (b) The Ramsey decay time for different phases of the compensation signal.

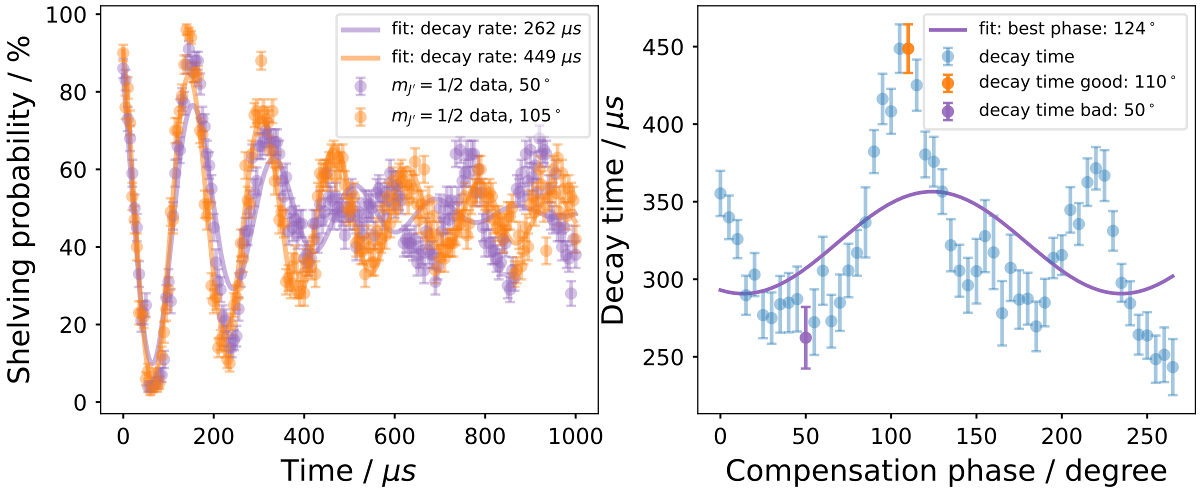

Figure 5.5: Compensation of the AC-line noise using 2 V for different phases. Ramsey sequences are performed on the $|m_J = 1/2\rangle \leftrightarrow |m_{J'} = 1/2\rangle$ transition in $^{138}\mathrm{Ba}^+$. (a) Ramsey sequences of two of the data points in (b). (b) The Ramsey decay time for different phases of the compensation signal.

signal triggered by the AC line. A clear sinusoidal relationship can be seen, with the best phase for the compensating field found to be at around 108° phase. Comparing the best to the worst, compensation in phase improves the decay time compared to out of phase from 500 µs to 700 µs. It should be noted, however, that this is not an appreciable improvement when compared to the Ramsey decay time with no compensation at all.

Figure 5.5 shows the same experiment using a much higher compensation voltage of 2 V. In this case, the relationship is much less clear. For all phases, the decay time is worse than having no compensation, an indication that we are using more than double the correct compensation amplitude, as discussed at the end of the previous section. We do still see a small range of phases at 110°, near the same optimal phase determined from Figure 5.4. This gives further evidence that 110° is the right offset for the compensating signal to be completely out of phase with the magnetic field noise from the AC line.

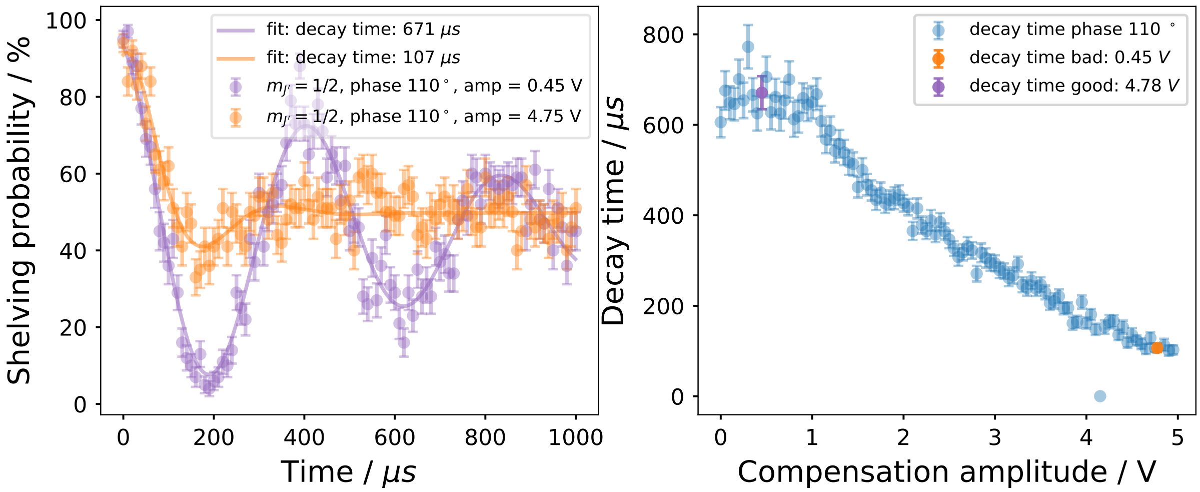

Figure 5.6: Compensation of the AC-line magnetic field noise using 110° for different amplitudes (voltage) of the compensating signal. Ramsey sequences are performed on the $|m_J = 1/2\rangle \leftrightarrow |m_{J'} = 1/2\rangle$ transition in $^{138}\text{Ba}^+$. (a) Ramsey sequences for examples of two of the data points in (b). (b) The Ramsey decay time for different voltages of the compensation signal.

In Figure 5.6, we fix the phase at 110° and vary the amplitude of the compensation signal from 0 V to 5 V. From this figure, it is clear that beyond 700 mV, the compensation only makes the coherence of the transition worse. In a small range from 200 mV to 500 mV, the coherence seems to improve very slightly, indicating that this is near the amplitude needed to cancel the magnetic field noise at the ion. The improvement is very small though, with a less than 10% increase in coherence time.

Overall, this improvement in coherence time does not seem to be very dramatic, in fact it's barely discernible. Compared to other groups who saw an improvement of an order of magnitude or more [203, 205, 206], our compensation seems to be not helping very much. These groups did use multiple frequencies in their compensation method, but they also had much higher amplitudes of these frequency components than we did (see Table 5.1). Alternatively, the main error could be coming from some other source. Even if this is the case, after we mitigate these other error sources, the AC-line noise could take over as the main contributing noise source and our compensation method could improve our coherence further from there. More recent experiments have indicated that at the actual ion position there may be a much stronger 180 Hz component than measured from the wall in Figure 5.2. This may come from a three-phase engine water pump running from under the optics table.

It should be noted that our vacuum chamber is surrounded by lead on all sides because we installed an ablation target of enriched, radioactive $^{133}\mathrm{Ba}^{+}$ [40]. We had to install lead shielding to keep exposure to the radiation low. All of this shielding could be coincidentally acting as magnetic-field shielding, reducing the AC-line noise experienced by the trap, and causing our compensation to not improve coherence by as much.

5.3 Permanent magnets

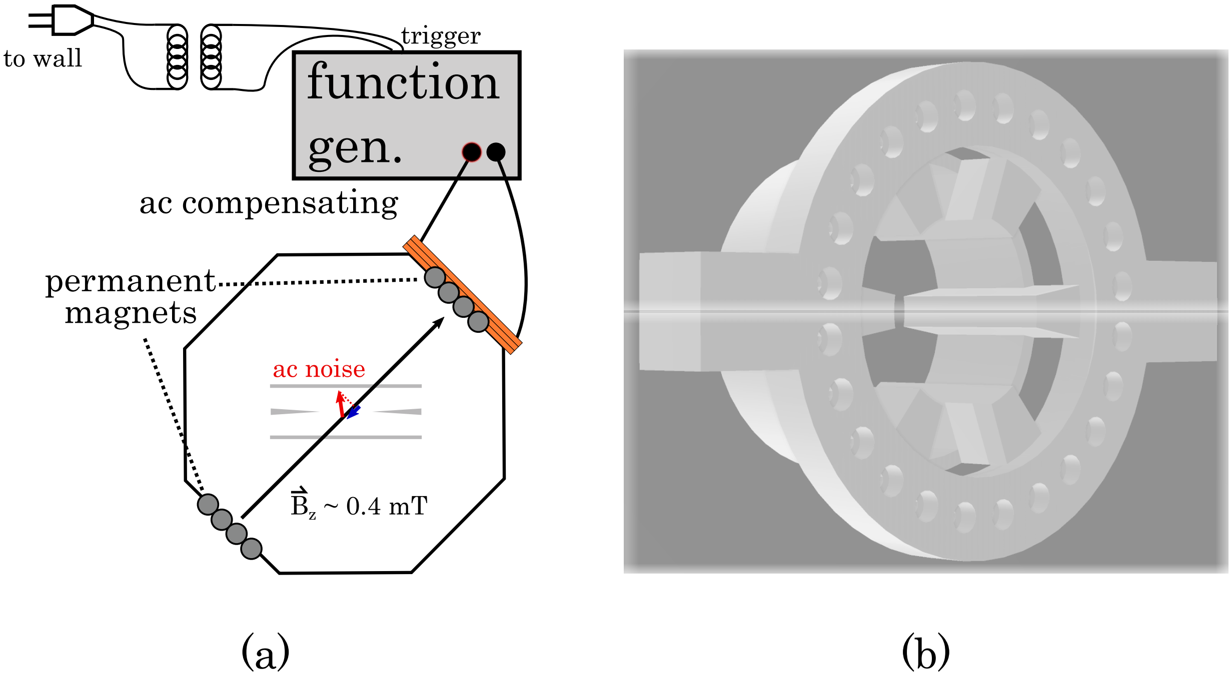

Figure 5.7: Our planned permanent magnets setup. (a) The AC-line compensation method will still be employed because these two methods correct for different noise. (b) The magnet mount. The cylindrical magnets fit inside each of the holes in the mount. Two mounts will be fixed onto opposite viewports with the magnets in opposite orientations so that their magnetic fields will be in the same direction.

Compensating for the AC magnetic field can reduce magnetic field noise from the AC magnetic field permeating throughout the lab and at the trap center. However, the lackluster result in Section 5.2.2 indicates that some other magnetic field noise is reducing the coherence of our ion much more than the AC-line noise is. Another main source of magnetic field noise is the current source used to generate the main quantization magnetic field from the magnetic field coils. Our current current source is a Keysight E3631 [208] DC power supply, which can produce a current up to 5 A, with a current noise of $< 2\,\mathrm{mA}$. The current generates a magnetic field of $0.423\,\mathrm{mT}/4\,\mathrm{A} = 0.106\,\mathrm{mT/A}$, which would give a magnetic field noise of 200 nT, which is actually larger than the noise estimated from AC-line noise, Equation 5.4. In addition, magnetic field coils can also experience thermal Johnson-Nyquist noise, especially at the temperatures they are running at, $\sim 60\,^{\circ}\mathrm{C}$.

Therefore, we can expect to gain further improvement in coherence by mitigating errors from the magnetic field coil as well. This can be done by either using an even better current source, or by completely moving away from using magnetic field coils to define the quantization axis. An alternative to driving current through magnetic field coils is to use static permanent magnets to generate the quantization field. Then one isn't reliant at all on the current source generating a clean current and magnetic field. The new error limit from magnetic field source would be the temperature fluctuations in the magnets causing the overall field to change, and this is a lot lower error than current source noise.

Our group has designed a set of permanent magnets using individual cylindrical polarized neodymium magnets of radius 0.125 In. and a remnant magnetic field of $1.48\,\mathrm{T}$. These are to be set into 3D printed parts and mounted to the viewports on either side. The mount and scheme are shown in Figure 5.7, with a total of 24 magnets in each holder. These are designed to be mounted in addition to the already mounted magnetic field coils. This will allow us to still use the coils for AC-line compensation, and for performing slight changes in the magnetic field for things like micromotion compensation, changing the direction slightly for coherent operations, or canceling the earth's magnetic field. The design has been tested and a magnetic field of $0.358\,\mathrm{mT}$ at the trap position has been achieved in a test setup.

Chapter 6

Conclusion

Using laser ablation of a $BaCl_2$ target with a 532 nm pulsed laser, and two-step photoionization with a coherent 554 nm first-step and an incoherent 405 nm second-step, we were able to successfully generate neutral barium atoms, ionize them, and trap them in our RF Paul trap, with the ability to selectively load different isotopes.

Many different aspects about laser ablation were discovered and explored. We found that spots on the $BaCl_2$ target must be conditioned before they can be used to generate sufficient atomic flux for trapping. This process consists of blasting the spot with a higher fluence in order to activate a spot for use with lower fluence. After a spot is conditioned, a new regime in fluence is available in which mostly neutral atoms are generated by ablation and not ions. This is quite useful because ions can cause charge build-up in the vacuum chamber, shifting the ion position away from the RF-null and introducing excess micromotion. I present a method for finding and activating a fresh spot on the ablation target and characterize this process. We have found that around half of the time, a spot is never able to be activated for generating sufficient atomic flux. The other half of the time, the neutral atomic flux ranges from moderate to high yield.

A TOF spectrum was performed to characterize the atomic plume produced from ablation. From this, we find that there is a significant Doppler shift of the fast atoms, but looking at only the slower atoms we were able to see the peaks for the different isotopes in the spectrum. Using the middle ^{137}Ba peak, we are able to load $^{137}Ba^+$ reliably. We were able to extract a velocity distribution for our atomic plume, and find that the temperature is on the order of $35,000$ K. This result is higher than we expected, but we believe the explanation has to do with the more complete method we used to look at the atomic velocities.

Loading of barium ions was demonstrated, with the loading rate of $^{138}\mathrm{Ba}^+$ being around 1 ions/pulse and the loading rate of $^{137}\mathrm{Ba}^+$ being around 0.1 ions/pulse, exactly what we expect from the natural abundances of these two isotopes. The loading rate of barium was shown to correlate well with the neutral fluorescence signal we measured from the ablation plume. This allows us to dynamically monitor the loading rate without having to perform more statistical experiments.

Finally, our methods were shown to be isotope selective for the two isotopes we care about $^{138}\mathrm{Ba}^+$ and $^{137}\mathrm{Ba}^+$. The selectivity of $^{138}\mathrm{Ba}^+$ was improved from its natural abundance of 72% to 85%, while the selectivity of $^{137}\mathrm{Ba}^+$ was improved from its natural abundance of 12% to 37%. The selectivity was also shown to depend on the power of the 554 nm laser, with higher power broadening the transition, reducing the linewidth, and thus reducing selectivity.

With that, we now have a reliable method for generating atomic flux, ionizing neutral atoms, and trapping the ions in our ion trap. One option for improving the loading technique which we have already begun to demonstrate is to use a different second step of the REMPI process. Instead of using an incoherent 405 nm laser to drive electrons directly into the continuum, a resonant transition can be used via an auto-ionizing interaction [163]. This uses a 389 nm transition, and has already been demonstrated in our lab [177] to have an improvement in loading rate by an order of magnitude. With this higher loading rate, we can trap $^{137}\mathrm{Ba}^+$ in single pulses rather than up to 10. We could also decrease power of the first step photoionization laser 554 nm to below saturation to greatly increase our selectivity.

To measure out the state of a high-dimensional qudit in barium, a quadrupole transition to the metastable $D_{5/2}$ level must be used. We characterized this transition in $^{138}\mathrm{Ba}^+$ and $^{137}\mathrm{Ba}^+$ and achieved a 13-level qudit SPAM result.

We were able to find the vicinity of the 1762 nm transition using a method where we had all fluorescence lasers on while we scanned the shelving laser's frequency. This effectively broadened the narrow transition so that we could roughly find it. From there, we performed spectrum measurements to find all of the transitions in $^{138}\mathrm{Ba}^+$ and $^{137}\mathrm{Ba}^+$. It was a challenge to figure out which of these transitions was which, but with the help of our theoretical models of the transition frequencies, we were able to assign all of the transitions found in the spectra to their respective $F', m_{F'}$ energy levels being driven to.

Next, we performed coherent quantum operations on each of these found transitions. Rabi scans were done for both isotopes, which revealed that we could coherently drive population from the ground state into the metastable state with high fidelity. One might think that the complexity of the energy structure in $^{137}\mathrm{Ba}^+$, especially in the metastable

$D_{5/2}$ level, might make most of the energy-levels unusable, however we found that nearly all of them could be transferred with over 90% fidelity. We also performed Ramsey sequences on all of the transitions in both isotopes, which revealed that the coherence times were on the order of 400 µs. The frequencies change from day-to-day due to cavity drift and magnetic field drift, so we must calibrate to the transitions at least daily. That's up to 14 transitions we must calibrate to, which takes an appreciable amount of time. To decrease this time, we came up with an interpolation method which can find all of the transition frequencies from measuring just three of them. We tried to do a similar thing for the π-time calibrations, and it does work, however due to device limitations in our setup, it cannot be done without introducing some additional error.

Finally, we were able to use these transitions to perform SPAM on different qudits in $^{138}\text{Ba}^+$ and $^{137}\text{Ba}^+$. A three-level qutrit in $^{138}\text{Ba}^+$ yielded a SPAM fidelity of around 98%, while a six-level qudit in the same isotope gave an overall fidelity of around 94%. In $^{137}\text{Ba}^+$, we were able to demonstrate a SPAM measurement of a 13-level qudit with a fidelity of 92%.

One of the major stumbling points we ran into for with this quadrupole transition was limitations with our current AWG used to generate the frequencies driving the transitions. Toggling through different waveforms tends to be slow because it has to complete each waveform before moving on to the next, which makes the overall SPAM measurement for a 13-level qudit on the order of 100 ms when it could be much faster around 10 ms (see Reference [37, 121]). In addition, the resolution we can use for arbitrary waveforms is limited by device memory, a fact that was elucidated by our results with π-time interpolation which resulted in slightly reduced fidelities.

With our demonstration of a 13-level qudit, the path is clear to start doing more coherent operations between the qudit levels to try and build up a fully functioning quantum computing platform with it. This includes proving out the single- and two-qudit gates proposed in our 2020 paper [33]. In addition, we could attempt to go even higher, with an up a 24-level qudit possible with our ion by just adding in coherent operations to other ground states. Qudits are just starting to become a prominent field of experimental quantum computation, and so the possibilities for future experiments are quite extensive.

Most of the error in our coherent operations on the quadrupole transition is predicted to be from magnetic field noise, and so we explored methods to mitigate this noise. First, we hypothesized from previous work that much of the noise is coming from magnetic field fluctuations at the mains AC-line voltage. So we used a compensation method which uses the AC voltage as a trigger for our compensation magnetic field signal, which is a sine wave which should destructively interfere with the AC-line magnetic field. We measured the actual voltage of the wall power, and were able to see how strong the various spectral components were, and surprisingly, the main 60 Hz component was the only appreciable frequency in the signal. Therefore, we decided to do the compensation with a simple sinusoidal wavefunction with just this frequency.

We demonstrated this compensation method using one of the quadrupole transitions of ${}^{138}\mathrm{Ba}^{+}$, and were able to find the correct phase that the compensation signal needs to cancel the AC-line magnetic field. However, when we found the correct amplitude of the compensation signal, the results were lackluster, with only a very small improvement in the coherence time of less than 10%. The other common magnetic field noise source is the current source used to drive magnetic field coils. To try and mitigate this noise, we designed a permanent magnet setup which will replace the coils and hopefully improve our coherence times in the future.

Even with the AC-line noise not really helping improve our coherence times very much, it will certainly be useful in the future once we can mitigate whatever IS our largest magnetic field noise error source. Perhaps after we install permanent magnets, the fidelity will improve significantly, and using the AC-line noise compensation will push it even further. Some other avenues of decreasing this magnetic field noise error include using more of the harmonics from the AC-line voltage, or adding μ-metal shielding around the ion trap to reduce environmental magnetic field noise from reaching the ion. Further experiments towards mitigating the magnetic field noise will be explored in future theses, with a sneak-peak being that there may be more 180 Hz noise being introduced by a water pump near the chamber.

References

[1] D. Nolting, R. Malek, and A. Makarov. Ion traps in modern mass spectrometry. *Mass Spect. Rev.*, 38(2):150–168, Oct 2019.

[2] C. D. Bruzewicz, J. Chiaverini, R. McConnell, and J. M. Sage. Trapped-ion quantum computing: Progress and challenges. *App. Phys. Rev.*, 6(2):021314, 2019.

[3] H. S. Margolis. Trapped ion optical clocks. *Eur. Phys. J. Spec. Top.*, 172:97–107, 2009.

[4] A. D. Ludlow, M. M. Boyd, J. Ye, E. Peik, and P. O. Schmidt. Optical atomic clocks. *Rev. Mod. Phys.*, 87:637–701, Jun 2015.

[5] N. Huntemann, C. Sanner, B. Lipphardt, Chr. Tamm, and E. Peik. Single-ion atomic clock with 3×10^{-18} systematic uncertainty. *Phys. Rev. Lett.*, 116:063001, Feb 2016.

[6] T. P. Harty, D. T. C. Allcock, C. J. Ballance, L. Guidoni, H. A. Janacek, N. M. Linke, D. N. Stacey, and D. M. Lucas. High-fidelity preparation, gates, memory, and readout of a trapped-ion quantum bit. *Phys. Rev. Lett.*, 113:220501, Nov 2014.

[7] C. J. Ballance, T. P. Harty, N. M. Linke, M. A. Sepiol, and D. M. Lucas. High-fidelity quantum logic gates using trapped-ion hyperfine qubits. *Phys. Rev. Lett.*, 117:060504, Aug 2016.

[8] F. A. An, A. Ransford, A. Schaffer, L. R. Sletten, J. Gaebler, J. Hostetter, and G. Vittorini. High fidelity state preparation and measurement of ion hyperfine qubits with $I > \frac{1}{2}$. *Phys. Rev. Lett.*, 129:130501, Sep 2022.

[9] D. Coppersmith. An approximate Fourier transform useful in quantum factoring. , Jan 2002.

[10] A. Peres. Reversible logic and quantum computers. *Phys. Rev. A*, 32:3266–3276, Dec 1985.

[11] S. Devitt, W. Munro, and K. Nemoto. Quantum error correction for beginners. *Rep. Prog. Phys.*, 76:076001, 06 2013.

[12] J. P. Gaebler, T. R. Tan, Y. Lin, Y. Wan, R. Bowler, A. C. Keith, S. Glancy, K. Coakley, E. Knill, D. Leibfried, and D. J. Wineland. High-fidelity universal gate set for $^9\mathrm{Be}^+$ ion qubits. *Phys. Rev. Lett.*, 117:060505, Aug 2016.

[13] D. Kielpinski, Monroe C., and D. J. Wineland. Architecture for a large-scale ion-trap quantum computer. *Nature*, 417:709–711, Jun 2002.

[14] T. C. Ralph, K. J. Resch, and A. Gilchrist. Efficient Toffoli gates using qudits. *Phys. Rev. A*, 75:022313, Feb 2007.

[15] P. Gokhale, J. M. Baker, C. Duckering, N. C. Brown, K. R. Brown, and F. T. Chong. Asymptotic improvements to quantum circuits via qutrits. In *Proc. 46th Int. Symp. on Comp. Arch.*, page 554–566, New York, NY, USA, 2019. ACM.

[16] B. P. Lanyon, M. Barbieri, M. P. Almeida, T. Jennewein, T. C. Ralph, K. J. Resch, G. J. Pryde, J. L. O'Brien, A. Gilchrist, and A. G. White. Simplifying quantum logic using higher-dimensional Hilbert spaces. *Nature Phys.*, 5:134–140, 2008.

[17] V. Parasa and M. Perkowski. Quantum phase estimation using multivalued logic. In *41st IEEE Int. Symp. on Mult.-Valued Logic*, pages 224–229, Tuusula, Finland, 2011. IEEE.

[18] S. S. Bullock, D. P. O'Leary, and G. K. Brennen. Asymptotically optimal quantum circuits for d-level systems. *Phys. Rev. Lett.*, 94:230502, Jun 2005.

[19] I. Cohen, P. Richerme, Z. X. Gong, C. Monroe, and A. Retzker. Simulating the Haldane phase in trapped-ion spins using optical fields. *Phys. Rev. A*, 92(1):1–10, 2015.

[20] E. T. Campbell. Enhanced fault-tolerant quantum computing in d-Level systems. *Phys. Rev. Lett.*, 113:230501, Dec 2014.

[21] E. T. Campbell, H. Anwar, and D. E. Browne. Magic-state distillation in all prime dimensions using quantum Reed-Muller codes. *Phys. Rev. X*, 2:041021, Dec 2012.

[22] F. H. E. Watson, H. Anwar, and D. E. Browne. Fast fault-tolerant decoder for qubit and qudit surface codes. *Phys. Rev. A*, 92:032309, Sep 2015.

[23] R. S. Andrist, J. R. Wootton, and H. G. Katzgraber. Error thresholds for Abelian quantum double models: Increasing the bit-flip stability of topological quantum memory. *Phys. Rev. A*, 91:042331, Apr 2015.

[24] M. Reiher, N. Wiebe, K. M. Svore, D. Wecker, and M. Troyer. Elucidating reaction mechanisms on quantum computers. *Proc. Natl. Acad. Sci. U.S.A.*, 114(29):7555–7560, 2017.

[25] M. R. Dietrich, A. Avril, R. Bowler, N. Kurz, J. S. Salacka, G. Shu, and B. B. Blinov. Barium ions for quantum computation. *AIP Conf. Proc.*, 1114(1):25–30, 2009.

[26] M. R. Dietrich, N. Kurz, T. Noel, G. Shu, and B. B. Blinov. Hyperfine and optical barium ion qubits. *Phys. Rev. A*, 81(5):5–8, 2010.

[27] R. D. Graham, S.-P. Chen, T. Sakrejda, J. Wright, Z. Zhou, and B. B. Blinov. A system for trapping barium ions in a microfabricated surface trap. *AIP Advances*, 4(5):057124, 2014.

[28] D. Hucul, J. E. Christensen, E. R. Hudson, and W. C. Campbell. Spectroscopy of a synthetic trapped ion qubit. *Phys. Rev. Lett.*, 119:100501, Sep 2017.

[29] S. Olmschenk and P. Becker. Laser ablation production of Ba, Ca, Dy, Er, La, Lu, and Yb ions. *Appl. Phys. B Lasers Opt.*, 123(4):1–6, 2017.

[30] G. Leschhorn, T. Hasegawa, and T. Schaetz. Efficient photo-ionization for barium ion trapping using a dipole-allowed resonant two-photon transition. *Appl. Phys. B Lasers Opt.*, 108(1):159–165, 2012.

[31] A. A. Madej and J. D. Sankey. Quantum jumps and the single trapped barium ion: Determination of collisional quenching rates for the $5d^2D_{5/2}$ level. *Phys. Rev. A*, 41:2621–2630, Mar 1990.

[32] S. G. Schirmer, A. D. Greentree, V. Ramakrishna, and H. Rabitz. Constructive control of quantum systems using factorization of unitary operators. *J. Phys. A*, 35(39):8315–8339, Sep 2002.

[33] P. J. Low, B. M. White, A. A. Cox, M. L. Day, and C. Senko. Practical trapped-ion protocols for universal qudit-based quantum computing. *Phys. Rev. Res.*, 2:033128, Jul 2020.

[34] M. Ringbauer, M. Meth, L. Postler, R. Stricker, R. Blatt, P. Schindler, and T. Monz. A universal qudit quantum processor with trapped ions. *Nature Phys.*, 18(9):1053–1057, Sep 2022.

[35] M. A. Aksenov, I. V. Zalivako, I. A. Semerikov, A. S. Borisenko, N. V. Semenin, P. L. Sidorov, A. K. Fedorov, K. Yu. Khabarova, and N. N. Kolachevsky. Realizing quantum gates with optically addressable $^{171}\mathrm{Yb}^{+}$ ion qudits. *Phys. Rev. A*, 107:052612, May 2023.

[36] P. Hrmo, B. Wilhelm, L. Gerster, M. W. van Mourik, M. Huber, R. Blatt, P. Schindler, T. Monz, and M. Ringbauer. Native qudit entanglement in a trapped ion quantum processor. *Nature Comm.*, 14(1), 2023.

[37] P. J. Low, B. M. White, and C. Senko. Control and readout of a 13-level trapped ion qudit. working paper, Jun 2023.

[38] K. DeBry, J. Sinanan-Singh, C. D. Bruzewicz, D. Reens, M. E. Kim, M. P. Roychowdhury, R. McConnell, , I. L. Chuang, and J. Chiaverini. Experimental quantum channel discrimination using metastable states of a trapped ion. working paper, May 2023.

[39] B. M. Bramman. Measuring trapped ion qudits. Master's thesis, University of Waterloo, 2019.

[40] B. M. White, P. J. Low, Y. de Sereville, M. L. Day, Noah G., R. Rademacher, and C. Senko. Isotope-selective laser ablation ion-trap loading of $^{137}\mathrm{Ba}^{+}$ using a BaCl_2 target. *Phys. Rev. A*, 105:033102, Mar 2022.

[41] P. J. Low. Tolerable experimental imperfections for a quadrupole blade ion trap and practical qudit gates with trapped ions. Master's thesis, University of Waterloo, 2023.

[42] F. G. Major, V. N. Gheorghe, and G. Werth. *Charged particle traps.* Springer, 2005. Chapter 2: The Paul Trap.

[43] P. K. Ghosh. *Ion traps.* Oxford Press, 1995. Chapter 2: Paul trap Confinement.

[44] D.J. Wineland, C. Monroe, W.M. Itano, D. Leibfried, B.E. King, D.M. Meekhof, and C. Myatt. Experimental issues in coherent quantum-state manipulation of trapped atomic ions. *J. of Research of NIST*, 103(3):259–238, 1998.

[45] H. J. Metcalf and P. van der Straten. *Laser cooling and trapping*. Springer, 1999. Chapter 2: The Density Matrix.

[46] D. T. C. Allcock, W. C. Campbell, J. Chiaverini, I. L. Chuang, E. R. Hudson, I. D. Moore, A. Ransford, C. Roman, J. M. Sage, and D. J. Wineland. omg blueprint for trapped ion quantum computing with metastable states. *Applied Physics Letters*, 119(21), 11 2021. 214002.

[47] P. Wang, C. Luan, M. Qiao, M. Um, J. Zhang, Y. Wang, X. Yuan, M. Gu, J. Zhang, and K. Kim. Single ion qubit with estimated coherence time exceeding one hour. *Nature Comm.*, 12(233), 2021.

[48] T. Ruster, C. T. Schmiegelow, H. Kaufmann, C. Warschburger, F. Schmidt-Kaler, and U. G. Poschinger. A long-lived Zeeman trapped-ion qubit. *Appl. Phys. B*, 122(10):1–7, 2016.

[49] F. Hakelberg, P. Kiefer, M. Wittemer, T. Schaetz, and U. Warring. Hybrid setup for stable magnetic fields enabling robust quantum control. *Sci. Rep.*, 8(1):1–8, 2018.

[50] C. Piltz, T. Sriarunothai, A.F. Varón, and C. Wunderlich. A trapped-ion-based quantum byte with 10e-5 next-neighbour cross-talk. *Nature Comm.*, 5(1), 2014.

[51] A. Bermudez, X. Xu, R. Nigmatullin, J. O'Gorman, V. Negnevitsky, P. Schindler, T. Monz, U. G. Poschinger, C. Hempel, J. Home, F. Schmidt-Kaler, M. Biercuk, R. Blatt, S. Benjamin, and M. Müller. Assessing the progress of trapped-ion processors towards fault-tolerant quantum computation. *Phys. Rev. X*, 7:041061, Dec 2017.

[52] C. Ospelkaus, U. Warring, Y. Colombe, K. R. Brown, J. M. Amini, D. Leibfried, and D. J. Wineland. Microwave quantum logic gates for trapped ions. *Nature*, 476:181–184, 2011.

[53] J. M. Pino, J. M. Dreiling, C. Figgatt, J. P. Gaebler, S. A. Moses, M. S. Allman, C. H. Baldwin, M. Foss-Feig, D. Hayes, K. Mayer, C. Ryan-Anderson, and B. Neyenhuis. Demonstration of the trapped-ion quantum CCD computer architecture. *Nature*, 592:209–213, 2021.

[54] C. Monroe, R. Raussendorf, A. Ruthven, K. R. Brown, P. Maunz, L.-M. Duan, and J. Kim. Large-scale modular quantum-computer architecture with atomic memory and photonic interconnects. *Phys. Rev. A*, 89:022317, Feb 2014.

[55] D. Hucul, I. V. Inlek, G. Vittorini, C. Crocker, S. Debnath, S. M. Clark, and C. Monroe. Modular entanglement of atomic qubits using photons and phonons. *Nature Phys.*, 11:37–42, 2015.

[56] D. Gottesman. Fault-tolerant quantum computation with higher-dimensional systems. *Chaos, Solitons, Fractals*, 10(10):1749–1758, 1999.

[57] M. Luo and X. Wang. Universal quantum computation with qudits. *Sci. China-Phys. Mech. Astron.*, 57(9):1712–1717, Sep 2014.

[58] N. J. Cerf, M. Bourennane, A. Karlsson, and N. Gisin. Security of quantum key distribution using d-level systems. *Phys. Rev. Lett.*, 88:127902, Mar 2002.

[59] R. T. Thew, K. Nemoto, A. G. White, and W. J. Munro. Qudit quantum-state tomography. *Phys. Rev. A*, 66:012303, Jul 2002.

[60] D. Kaszlikowski, D. K. L. Oi, M. Christandl, K. Chang, A. Ekert, L. C. Kwek, and C. H. Oh. Quantum cryptography based on qutrit Bell inequalities. *Phys. Rev. A*, 67:012310, Jan 2003.

[61] G. K. Brennen, D. P. O'Leary, and S. S. Bullock. Criteria for exact qudit universality. *Phys. Rev. A*, 71:052318, May 2005.

[62] D. P. O'Leary, G. K. Brennen, and S. S. Bullock. Parallelism for quantum computation with qudits. *Phys. Rev. A*, 74:032334, Sep 2006.

[63] G. K. Brennen, S. S. Bullock, and D. P. O'Leary. Efficient circuits for exact-universal computation with qudits. *Q. Inf. Comput.*, 6:436–454, May 2006.

[64] A. B. Klimov, R. Guzmán, J. C. Retamal, and C. Saavedra. Qutrit quantum computer with trapped ions. *Phys. Rev. A*, 67:062313, Jun 2003.

[65] A. Muthukrishnan and C. R. Stroud. Multidevice logic gates for quantum computing. *Phys. Rev. A*, 62:052309, Oct 2000.

[66] S. D. Bartlett, H. de Guise, and B. C. Sanders. Quantum encodings in spin systems and harmonic oscillators. *Phys. Rev. A*, 65:052316, May 2002.

[67] B. Andrade, Z. Davoudi, T. Graß, G. Hafezi, M. Pagano, and Seif A. Engineering an effective three-spin Hamiltonian in trapped-ion systems for applications in quantum simulation. *Q. Sci. and Tech.*, 7:034001, Apr 2022.

[68] W. C. Campbell and E. R. Hudson. Polyqubit quantum processing. working paper, Oct 2022.

[69] B. Mischuck and K. Mølmer. Qudit quantum computation in the Jaynes-Cummings model. *Phys. Rev. A*, 87:022341, Feb 2013.

[70] S. Omanakuttan, A. Mitra, M. J. Martin, and I. H. Deutsch. Quantum optimal control of ten-level nuclear spin qudits in ^{87}Sr. *Phys. Rev. A*, 104:L060401, Dec 2021.

[71] M. Chizzini, L. Crippa, A. Chiesa, F. Tacchino, F. Petiziol, I. Tavernelli, P. Santini, and S. Carretta. Molecular nanomagnets with competing interactions as optimal units for qudit-based quantum computation. *Phys. Rev. Res.*, 4:043135, Nov 2022.

[72] J. Lindon, A. Tashchilina, L. W. Cooke, and L. J. LeBlanc. Complete unitary qutrit control in ultracold atoms. *Phys. Rev. Appl.*, 19:034089, Mar 2023.

[73] G. Braiman, O. Reinhardt, C. Mechel, O. Levi, and I. Kaminer. The synthetic hilbert space of laser-driven free-electrons. *Quantum*, 7:888, January 2023.

[74] J. Randall, S. Weidt, E. D. Standing, K. Lake, S. C. Webster, D. F. Murgia, T. Navickas, K. Roth, and W. K. Hensinger. Efficient preparation and detection of microwave dressed-state qubits and qutrits with trapped ions. *Phys. Rev. A*, 91:012322, Jan 2015.

[75] C. Senko, P. Richerme, J. Smith, A. Lee, I. Cohen, A. Retzker, and C. Monroe. Realization of a quantum integer-spin chain with controllable interactions. *Phys. Rev. X*, 5:021026, Jun 2015.

[76] F. M. Leupold, M. Malinowski, C. Zhang, V. Negnevitsky, A. Cabello, J. Alonso, and J. P. Home. Sustained state-independent quantum contextual correlations from a single ion. *Phys. Rev. Lett.*, 120:180401, May 2018.

[77] I. V. Zalivako, A. S. Borisenko, A. I. Semerikov, A. Korolkov, P. L. Sidorov, K. Galstyan, N. V. Semenin, V. Smirnov, M. A. Aksenov, A. K. Fedorov, K. Y. Khabarova, and N. N. Kolachevsky. Continuous dynamical decoupling of optical ^{171}Yb^{+} qudits with radiofrequency fields. working paper, May 2023.

[78] K. Ke Sun, C. Fang, M. Kang, Z. D. Zhang, P. Zhang, D. N. Beratan, K. R. Brown, and Kim J. Quantum simulation of polarized light-induced electron transfer with a trapped-ion qutrit system. working paper, Apr 2023.

[79] P. Liu, R. X. Wang, J. N. Zhang, Y. S. Zhang, X. X. Cai, H. K. Xu, Z. Y. Li, J. X. Han, X. G. Li, G. M. Xue, W. Y. Liu, L. You, Y. R. Jin, and H. F. Yu. Performing SU(d) operations and rudimentary algorithms in a superconducting transmon qudit for $d = 3$ and $d = 4$. *Phys. Rev. X*, 13:021028, May 2023.

[80] Y. Chi, J. S Huang, Z. C. Zhang, J. Mao, Z. N. Zhou, X. J. Chen, C. H. Zhai, J. M. Bao, T. X. Dai, H. H. Yuan, M. Zhang, D. X. Dai, B. Tang, Y. Yang, Z. H. Li, Y. H. Ding, L. K. Oxenløwe, M. G. Thompson, J. L. O'Brien, Y. Li, Q. H. Gong, and J. W. Wang. A programmable qudit-based quantum processor. *Nature Comm.*, 13(1166), 2022.

[81] Z. Gedik, I. Silva, B. Çakmak, G. Karpat, E. L. G. Vidoto, D. O. Soares-Pinto, deAzevedo E. R., and Fanchini F. F. Computational speed-up with a single qudit. *Sci. Rep.*, 5(14671), 2015.

[82] N. Neeley, M. Ansmann, R. C. Bialczak, M. Hofheinz, E. Lucero, A. D. O'Connell, D. Sank, H. H. Wang, J. Wenner, A. N. Cleland, M. R. Geller, and J. M. Martinis. Emulation of a quantum spin with a superconducting phase qudit. *Science*, 325(5941):722–725, 2009.

[83] G. Lima, A. Vargas, L. Neves, R. Guzmán, and C. Saavedra. Manipulating spatial qudit states with programmable optical devices. *Opt. Express*, 17(13):10688–10696, Jun 2009.

[84] K. Mato, M. Ringbauer, S. Hillmich, and R. Wille. Adaptive Compilation of Multi-Level Quantum Operations. In *2022 IEEE Int. Conf. on Q. Comp. and Eng. (QCE)*, pages 484–491, 2022.

[85] J. Denis and J. Martin. Extreme depolarization for any spin. *Phys. Rev. Res.*, 4:013178, Mar 2022.

[86] B. M. Mihalcea. Quasienergy operators and generalized squeezed states for systems of trapped ions. *A. of Phys.*, 442:168926, 2022.

[87] J. M. Baker, C. Duckering, and F. T. Chong. Efficient Quantum Circuit Decompositions via Intermediate Qudits. In *2020 IEEE 50th Int. Symp. on Mult.-Valued Logic (ISMVL)*, pages 303–308, 2020.

[88] B. I. Bantysh and Y. I. Bogdanov. Quantum tomography of noisy ion-based qudits. *Laser Phys. Lett.*, 18(1):015203, Dec 2020.

[89] N. Wyderka, G. Chesi, H. Kampermann, C. Macchiavello, and D. Bruß. Construction of efficient Schmidt-number witnesses for high-dimensional quantum states. *Phys. Rev. A*, 107:022431, Feb 2023.

[90] T. André and E. Sjöqvist. Dark path holonomic qudit computation. *Phys. Rev. A*, 106:062402, Dec 2022.

[91] A. J. Moorthy and L. G. Gunderman. Local-dimension-invariant Calderbank-Shor-Steane codes with an improved distance promise. *Q. Inf. Proc.*, 22(1):1573–1332, 2023.

[92] L. G. Gunderman. Degenerate local-dimension-invariant stabilizer codes and an alternative bound for the distance preservation condition. *Phys. Rev. A*, 105:042424, Apr 2022.

[93] L. G. Gunderman. Local-dimension-invariant qudit stabilizer codes. *Phys. Rev. A*, 101:052343, May 2020.

[94] Y. Ma, M. Hanks, and M. S. Kim. Non-Pauli errors can be efficiently sampled in qudit surface codes. working paper, Mar 2023.

[95] L. Gunderman. *Collective spin-cavity ensembles and the protection of higher-dimensional quantum information* . PhD thesis, University of Waterloo, 2022.

[96] E. Durso-Sabina. Flag fault-tolerant error correction with qudits. Master's thesis, University of Waterloo, 2021.

[97] L. E. Fischer, D. Miller, F. Tacchino, P. K. Barkoutsos, D. J. Egger, and I. Tavernelli. Ancilla-free implementation of generalized measurements for qubits embedded in a qudit space. *Phys. Rev. Res.*, 4:033027, Jul 2022.

[98] M. Rambach, M. Qaryan, M. Kewming, C. Ferrie, A. G. White, and J. Romero. Robust and efficient high-dimensional quantum state tomography. *Phys. Rev. Lett.*, 126:100402, Mar 2021.

[99] E. O. Kiktenko, A. S. Nikolaeva, Peng Xu, G. V. Shlyapnikov, and A. K. Fedorov. Scalable quantum computing with qudits on a graph. *Phys. Rev. A*, 101:022304, Feb 2020.

[100] M. D. Zhu, L. Yan, X. Qin, W. Z. Zhang, Y. H. Lin, and J. F. Du. FPGA based hardware platform for trapped-ion-based multi-level quantum systems. *Chinese Phys. B*, 2023.

[101] A. Giraldo-Carvajal and J. A. Jaramillo-Villegas. QuantumSkynet: A high dimensional quantum computing simulator. In *Frontiers in Optics / Laser Science*, page JW6A.25. Optica Publishing Group, 2020.

[102] M. Grassl, M. Rötteler, and T. BETH. Efficient quantum circuits for non-qubit quantum error-correcting codes. *Int. J. Found. Comput. Sci.*, 14(05):757–775, 2003.

[103] G. F. Xu, P. Z. Zhao, Erik Sjöqvist, and D. M. Tong. Realizing nonadiabatic holonomic quantum computation beyond the three-level setting. *Phys. Rev. A*, 103:052605, May 2021.

[104] M. Mohammadi, A. Niknafs, and M. Eshghi. Controlled gates for multi-level quantum computation. *Q. Inf. Proc.*, 10(2):241–256, Apr 2011.

[105] D. Bruß and C. Macchiavello. Optimal eavesdropping in cryptography with three-dimensional quantum states. *Phys. Rev. Lett.*, 88:127901, Mar 2002.

[106] A. S. Nikolaeva, E. O. Kiktenko, and A. K. Fedorov. Decomposing the generalized Toffoli gate with qutrits. *Phys. Rev. A*, 105:032621, Mar 2022.

[107] A. S. Nikolaeva, E. O. Kiktenko, and A. K. Fedorov. Generalized Toffoli gate decomposition using ququints: towards realizing Grover's algorithm with qudits. *Entropy*, 25(2), 2023.

[108] A. S. Nikolaeva, E. O. Kiktenko, and A. K. Fedorov. Efficient realization of quantum algorithms with qudits. working paper, Nov 2021.

[109] A. S. Nikolaeva, E. O. Kiktenko, and A. K. Fedorov. Compiling quantum circuits with qubits embedded in trapped-ion quidts. working paper, Feb 2023.

[110] J. Mackeprang, D. Bhatti, M. Hoban, and S. Barz. The power of qutrits for non-adaptive measurement-based quantum computing. *New J. Phys.*, 2023.

[111] X. Q. Gao, P. Appel, N. Friis, M. Ringbauer, and M. Huber. On the role of entanglement in qudit-based circuit compression . working paper, Sep 2022.

[112] C. W. Bauer, Z. Davoudi, A. B. Balantekin, T. Bhattacharya, M. Carena, W. A. de Jong, P. Draper, A. El-Khadra, N. Gemelke, M. Hanada, D. Kharzeev, H. Lamm, Y. Y. Li, J. Liu, M. Lukin, Y. Meurice, C. Monroe, B. Nachman, G. Pagano, J. Preskill, E. Rinaldi, A. Roggero, D. I. Santiago, M. J. Savage, I. Siddiqi, G. Siopsis, D. Van Zanten, N. Wiebe, Y. Yamauchi, K. Yeter-Aydeniz, and S. Zorzetti. Quantum simulation for high-energy physics. *PRX Q.*, 4:027001, May 2023.

[113] A. Ciavarella, N. Klco, and M. J. Savage. Trailhead for quantum simulation of SU(3) Yang-Mills lattice gauge theory in the local multiplet basis. *Phys. Rev. D*, 103:094501, May 2021.

[114] W. D. Kalfus, G. J. Ribeill, G. E. Rowlands, H. K. Krovi, T. A. Ohki, and L. C. G. Govia. Hilbert space as a computational resource in reservoir computing. *Phys. Rev. Res.*, 4:033007, Jul 2022.

[115] S. Ghosh and A. Sen(De). Dimensional enhancements in a quantum battery with imperfections. *Phys. Rev. A*, 105:022628, Feb 2022.

[116] E. Gustafson. Noise improvements in quantum simulations of sQED using qutrit. working paper, Jan 2022.

[117] M. X. Zhang, X. X. Yuan, Y. Li, X. W. Luo, C. Liu, M. D. Zhu, X. Qin, C. W. Zhang, Y. H. Lin, and J. F. Du. Observation of spin-tensor induced topological phase transitions of triply degenerate points with a trapped ion. *Phys. Rev. Lett.*, 129:250501, Dec 2022.

[118] I. M. Zalivako, C. E. P. Robin, and M. J. Savage. Quantum simulations of SO(5) many-fermion systems using qudits. working paper, May 2023.

[119] Time Base ECQDL. `http://www.time-base.de/`, 2023.

[120] Toptica DLPro ECDL. `https://www.toptica.com/`, 2023.

[121] P. J. Low. *Control and readout of high-dimensional trapped ion qudits*. PhD thesis, University of Waterloo, 2023.

[122] SLS 1762 nm stabilized laser. `https://stablelasers.com/`, 2023.

[123] moglabs CEL ECDL. `https://www.moglabs.com/`, 2023.

[124] HighFinesse WS-8-30 Wavelength Meter. `https://www.highfinesse.com/`, 2023.

[125] Toptica DLCPro laser controller. `https://www.toptica.com/`, 2023.

[126] Thorlabs Pro8000 laser controller. `https://www.thorlabs.com/`, 2023.

[127] DLC202 laser controller. `https://www.moglabs.com/`, 2023.

[128] Sandia IonControl system. `https://www.osti.gov/biblio/1326630`, 2023.

[129] N. Kjærgaard, L. Hornekær, A. M. Thommesen, Z. Videsen, and M. Drewsen. Isotope selective loading of an ion trap using resonance-enhanced two-photon ionization. *Appl. Phys. B Lasers Opt.*, 71(2):207–210, 2000.

[130] S. Gulde, D. Rotter, P. Barton, F. Schmidt-Kaler, R. Blatt, and W. Hogervorst. Simple and efficient photo-ionization loading of ions for precision ion-trapping experiments. *Appl. Phys. B Lasers Opt.*, 73(8):861–863, 2001.

[131] A. V. Steele, L. R. Churchill, P. F. Griffin, and M. S. Chapman. Photoionization and photoelectric loading of barium ion traps. *Phys. Rev. A*, 75(5), 2007.

[132] B. Wang, J. W. Zhang, C. Gao, and L. J. Wang. Highly efficient and isotope selective photo-ionization of barium atoms using diode laser and LED light. *Opt. Express*, 19(17):16438, 2011.

[133] T. G. Ballance, J. F. Goodwin, B. Nichol, L. J. Stephenson, C. J. Ballance, and D. M. Lucas. A short response time atomic source for trapped ion experiments. *Rev. Sci. Instrum.*, 89(5), 2018.

[134] C. G. Gill, A. W. Garrett, P. H. Hemberger, and N. S. Nogar. Selective laser ablation/ionization for ion trap mass spectrometry: Resonant laser ablation. *Spectrochim. Acta - Part B At. Spectrosc.*, 51(8):851–862, 1996.

[135] R. J. Hendricks, D. M. Grant, P. F. Herskind, A. Dantan, and M. Drewsen. An all-optical ion-loading technique for scalable microtrap architectures. *Appl. Phys. B Lasers Opt.*, 88(4):507–513, 2007.

[136] H. Shao, M. Wang, M. Zeng, H. Guan, and K. Gao. Laser ablation and two-step photo-ionization for the generation of $^{40}\text{Ca}^{+}$. *J. Phys. Commun.*, 2(9), 2018.

[137] G. Vrijsen, Y. Aikyo, R. F. Spivey, I. V. Inlek, and J. Kim. Efficient isotope-selective pulsed laser ablation loading of $^{174}\text{Yb}^{+}$ ions in a surface electrode trap. *Opt. Express*, 27(23):33907, 2019.

[138] D. R. Leibrandt, R. J. Clark, J. Labaziewicz, P. Antohi, K. R. Bakr, W.and Brown, and I. L. Chuang. Laser ablation loading of a surface-electrode ion trap. *Phys. Rev. A*, 76(5):1–4, 2007.

[139] K. Sheridan, W. Lange, and M. Keller. All-optical ion generation for ion trap loading. *Appl. Phys. B Lasers Opt.*, 104(4):755–761, 2011.

[140] S. J. Schowalter, K. Chen, W. G. Rellergert, S. T. Sullivan, and E. R. Hudson. An integrated ion trap and time-of-flight mass spectrometer for chemical and photo-reaction dynamics studies. *Rev. Sci. Instrum.*, 83(4), 2012.

[141] N. Greenberg. Vacuum and optical designs for an open-access trapped ion quantum processor . Master's thesis, University of Waterloo, 2020.

[142] Y. Hashimoto, L. Matsuoka, H. Osaki, Y. Fukushima, and S. Hasegawa. Trapping laser ablated Ca^+ ions in linear paul trap. *Japanese J. Appl. Physics, Part 1 Regul. Pap. Short Notes Rev. Pap.*, 45(9 A):7108–7113, 2006.

[143] M. Sameed, D. Maxwell, and N. Madsen. Ion generation and loading of a Penning trap using pulsed laser ablation. *New J. Phys.*, 22(1), 2020.

[144] K. Zimmermann, M. V. Okhapkin, O. A. Herrera-Sancho, and E. Peik. Laser ablation loading of a radiofrequency ion trap. *Appl. Phys. B Lasers Opt.*, 107(4):883–889, 2012.

[145] A. Poschl. *Laser ablation loading and single ion addressing of strontium in a linear paul trap*. PhD thesis, Royal Institute of Technology in Stockholm, 2018.

[146] X. Shi, S. L. Todaro, G. L. Mintzer, C. D. Bruzewicz, J. Chiaverini, and I. L. Chuang. Ablation loading of barium ions into a surface electrode trap. working paper, Mar 2023.

[147] L. Láska, J. Krása, M. Pfeifer, K. Rohlena, S. Gammino, L. Torrisi, L. Andò, and G. Ciavola. Angular distribution of ions emitted from Nd:YAG laser-produced plasma. *Rev. Sci. Instrum.*, 73(2):654, 2002.

[148] B. Thestrup, B. Toftmann, J. Schou, B. Doggett, and J. G. Lunney. Ion dynamics in laser ablation plumes from selected metals at 355 nm. *Appl. Surf. Sci.*, 197-198:175–180, 2002.

[149] L. Láska, K. Jungwirth, J. Krása, E. Krouský, M. Pfeifer, K. Rohlena, A. Velyhan, J. Ullschmied, S. Gammino, L. Torrisi, J. Badziak, P. Parys, M. Rosinski, L. Ryć, and J. Wolowski. Angular distributions of ions emitted from laser plasma produced at various irradiation angles and laser intensities. *Laser Part. Beams*, 26(4):555–565, 2008.

[150] minilite I Nd:YAG. `https://amplitude-laser.com/`, 2023.

[151] Thorlabs ES111C pyro-electric sensor. `https://www.thorlabs.com/`, 2023.

[152] R. D. Knight. Storage of ions from laser-produced plasmas. *Appl. Phys. Lett.*, 38(4):221–223, 1981.

[153] D. A. Davies, D. J. Morrissey, G. Bollen, P. A. Lofy, J. Ottarson, and S. C. Schwarz. A high-power laser ablation ion source for Penning trap studies of nuclear reaction products. *J. Phys. Conf. Ser.*, 59(1):136–139, 2007.

[154] M. Niemann, T. Meiners, J. Mielke, M. J. Borchert, and J. M. Cornejo. Cryogenic Be Penning trap for precision cryogenic ^{9}Be$^+$ Penning trap for precision measurements with (anti-)protons. *Meas. Sci. and Tech.*, 31(3):035003, Dec 2019.

[155] V.H.S. Kwong. Production and storage of low-energy highly charged ions by laser ablation and an ion trap. *Phys. Rev. A*, 39(9):4451–4454, 1989.

[156] L. Láska, K. Jungwirth, B. Králiková, J. Krása, M. Pfeifer, K. Rohlena, J. Skála, J. Ullschmied, J. Badziak, P. Parys, J. Wolowski, E. Woryna, S. Gammino, L. Torrisi, F. P. Boody, and H. Hora. Generation of multiply charged ions at low and high laser-power densities. *Plasma Phys. and Contr. Fusion*, 45(5):585–599, Mar 2003.

[157] T. Kwapień, U. Eichmann, and W. Sandner. Sympathetic cooling of laser-produced doubly charged ions in a few-ion crystal. *Phys. Rev. A*, 75(6):1–6, 2007.

[158] C. J. Campbell, A. V. Steele, L. R. Churchill, M. V. Depalatis, D. E. Naylor, D. N. Matsukevich, A. Kuzmich, and M. S. Chapman. Multiply charged thorium crystals for nuclear laser spectroscopy. *Phys. Rev. Lett.*, 102(23):3–6, 2009.

[159] O. Kornienko, P. T. A. Reilly, W. B. Whitten, and J. M. Ramsey. Electron impact ionization in a microion trap mass spectrometer. *Rev. Sci. Instrum.*, 70(10):3907–3909, 1999.

[160] O. J. Orient and A. Chutjian. A compact, high-resolution Paul ion trap mass spectrometer with electron-impact ionization. *Rev. Sci. Instrum.*, 73(5):2157, 2002.

[161] K. R. Brown, R. J. Clark, J. Labaziewicz, P. Richerme, D. R. Leibrandt, and I. L. Chuang. Loading and characterization of a printed-circuit-board atomic ion trap. *Phys. Rev. A*, 75(1):1–4, 2007.

[162] M. Cetina, A. Grier, J. Campbell, I. Chuang, and V. Vuletić. Bright source of cold ions for surface-electrode traps. *Phys. Rev. A*, 76(4):1–4, 2007.

[163] B. Willke and M. Kock. Measurement of photoionization cross sections from the laser-excited Ba I (6s6p) $^1P_1^0$ state. *J. of Phys. B*, 26(6):1129, Mar 1993.

[164] K. Yamada, N. Ozaki, M. Yamamoto, and K. I. Ueyanagi. Separation of barium isotopes by selective two-step photoionization process. *J. Nucl. Sci. Technol.*, 25(8):641–648, 1988.

[165] D. M. Lucas, A. Ramos, J. P. Home, M. J. McDonnell, S. Nakayama, J. P. Stacey, S. C. Webster, D. N. Stacey, and A. M. Steane. Isotope-selective photoionization for calcium ion trapping. *Phys. Rev. A*, 69(1):13, 2004.

[166] U. Tanaka, H. Matsunishi, I. Morita, and S. Urabe. Isotope-selective trapping of rare calcium ions using high-power incoherent light sources for the second step of photo-ionization. *Appl. Phys. B Lasers Opt.*, 81(6):795–799, 2005.

[167] U. Tanaka, I. Morita, and S. Urabe. Selective loading and laser cooling of rare calcium isotope $^{43}Ca^+$. *Appl. Phys. B Lasers Opt.*, 89(2-3):195–200, 2007.

[168] C. Schuck, M. Almendros, F. Rohde, M. Hennrich, and J. Eschner. Two-color photoionization of calcium using SHG and LED light. *Appl. Phys. B Lasers Opt.*, 100(4):765–771, 2010.

[169] M. Johanning, A. Braun, D. Eiteneuer, C. Paape, C. Balzer, W. Neuhauser, and C. Wunderlich. Resonance-enhanced isotope-selective photoionization of YbI for ion trap loading. *Appl. Phys. B Lasers Opt.*, 103(2):327–338, 2011.

[170] Chr Balzer, A. Braun, T. Hannemann, Chr Paape, M. Ettler, W. Neuhauser, and Chr Wunderlich. Electrodynamically trapped Yb^+ ions for quantum information processing. *Phys. Rev. A*, 73(4):1–4, 2006.

[171] M. Brownnutt, V. Letchumanan, G. Wilpers, R. C. Thompson, P. Gill, and A. G. Sinclair. Controlled photoionization loading of $^{88}Sr^+$ for precision ion-trap experiments. *Appl. Phys. B Lasers Opt.*, 87(3):411–415, 2007.

[172] P. E. G. Baird, R. J. Brambley, K. Burnett, D. N. Stacey, D. M. Warrington, G. K. Woodgate, and H. G. Kuhn. Optical isotope shifts and hyperfine structure in λ553.5nm of barium. *Proc. R. Soc. London, Ser. A*, 365(1723), 1979.

[173] K. Bekk, A. Andl, S. Göring, A. Hanser, G. Nowicki, H. Rebel, and G. Schatz. Laserspectroscopic studies of collective properties of neutron deficient Ba Nuclei. *Z. Phys. A*, 291(3):219–230, Sep 1979.

[174] W. A. van Wijngaarden and J. Li. Hyperfine splittings and isotope shifts of $(6s)^{2 1}S_0 \rightarrow (6s6p)^1P_1$ transition in barium. *Can. J. Phys.*, 73(7-8):484–488, 1995.

[175] C. Nazé, J. G. Li, and M. Godefroid. Theoretical isotope shifts in neutral barium. *Phys. Rev. A*, 91:032511, Mar 2015.

[176] M. D. Rotter. *Quantum feedback and quantum correlation measurements with a single Barium ion*. PhD thesis, University of Innsbruck, 2008.

[177] N. Greenberg, B. M. White, P. J. Low, and C. Senko. Trapping Ba$^+$ with Seven-fold Enhanced Efficiency Utilizing an Autoionizing Resonance. working paper, Jul 2023.

[178] Thorlabs NF533-17 filter. `https://www.thorlabs.com/`, 2023.

[179] Thorlabs FESH0500 filter. `https://www.thorlabs.com/`, 2023.

[180] IDEX FF01-484/561-25 filter. `https://www.idex-hs.com/`, 2023.

[181] Y. De Sereville. Towards dual-isotope entangling gates for trapped-ion quantum computing. Master's thesis, University of Waterloo, 2022.

[182] D. B. Chrisey. *Pulsed laser deposition of thin films*, volume 1. Wiley, 1994. Chapter 4.

[183] M. Guggemos, D. Heinrich, O. A. Herrera-Sancho, R. Blatt, and C. F. Roos. Sympathetic cooling and detection of a hot trapped ion by a cold one. *New J. Phys.*, 17(10), 2015.

[184] J. B. Matos, M. G. Destro, C. A. B. Silveira, and N. A. S. Rodrigues. Neutral atomic jet generation by laser ablation of copper targets. *Rev. Sci. Instrum.*, 85(1), 2014.

[185] A. Mortensen, J. J. T. Lindballe, I. S. Jensen, P. Staanum, D. Voigt, and M. Drewsen. Isotope shifts of the $4s^2\ ^1S_0 \rightarrow 4s5p\ ^1P_1$ transition and hyperfine splitting of the $4s5p\ ^1P_1$ state in calcium. *Phys. Rev. A*, 69:042502, Apr 2004.

[186] K. Toyoda, H. Kataoka, Y. Kai, A. Miura, M. Watanabe, and S. Urabe. Separation of laser-cooled ^{42}Ca$^+$ and ^{44}Ca$^+$ in a linear Paul trap. *Appl. Phys. B Lasers Opt.*, 72(3):327–330, 2001.

[187] M. Kitaoka and S. Hasegawa. Isotope-selective manipulation of Ca$^+$ using laser heating and cooling in a linear Paul trap. *J. Phys. B At. Mol. Opt. Phys.*, 45(16), 2012.

[188] P. V. Borisyuk, S. P. Derevyashkin, K. Y. Khabarova, N. N. Kolachevsky, Y. Y. Lebedinsky, S. S. Poteshin, A. A. Sysoev, A. V. Tkalya, D. O. Tregubov, V. I. Troyan, O. S. Vasiliev, V. P. Yakovlev, and V. I. Yudin. Mass selective laser cooling of $^{229}\mathrm{Th}^{3+}$ in a multisectional linear Paul trap loaded with a mixture of thorium isotopes. *E. J. of Mass Spect.*, 23(4):136–139, 2017. PMID: 29028395.

[189] R. Alheit, K. Enders, and G. Werth. Isotope separation by nonlinear resonances in a Paul trap. *Appl. Phys. B Lasers Opt.*, 62(5):511–513, 1996.

[190] T. Hasegawa and T. Shimizu. Removal of irrelevant isotope ions in the presence of laser cooling in a rf trap. *Appl. Phys. B Lasers Opt.*, 70(6):867–871, 2000.

[191] D. F. V. James. Quantum dynamics of cold trapped ions with application to quantum computation. *Appl. Phys. B*, 66(2):181–190, 1998.

[192] C. Roos. *Controlling the quantum state of trapped ions*. PhD thesis, University of Innsbruck, 2000.

[193] D. J. Berkeland and M. G. Boshier. Destabilization of dark states and optical spectroscopy in Zeeman-degenerate atomic systems. *Phys. Rev. A*, 65:033413, Feb 2002.

[194] R. Blatt and G. Werth. Precision determination of the ground-state hyperfine splitting in $^{137}\mathrm{Ba}^{+}$ using the ion-storage technique. *Phys. Rev. A*, 25:1476–1482, Mar 1982.

[195] R. E. Silverans, G. Borghs, P. De Bisschop, and M. Van Hove. Hyperfine structure of the 5d $^{2}\mathrm{D}_{\mathrm{J}}$ states in the alkaline-earth Ba ion by fast-ion-beam laser-rf spectroscopy. *Phys. Rev. A*, 33:2117–2120, Mar 1986.

[196] P. Villemoes, A. Arnesen, F. Heijkenskjold, and A. Wannstrom. Isotope shifts and hyperfine structure of 134-138 Ba II by fast ion beam-laser spectroscopy. *J. of Phys. B*, 26(22):4289–4299, Nov 1993.

[197] D. A. Steck. *Quantum and Atom Optics*. None, 2007. Chapter 7: Atomic Angular-Momentum Structure.

[198] T. Monz. *Quantum information processing beyond ten ion-qubits*. PhD thesis, University of Innsbruck, 2011.

[199] Harrison Ball and Michael J. Biercuk. Walsh-synthesized noise filters for quantum logic. *EPJ Q. Tech.*, 2(1):11, May 2015.

[200] Matthew L. Day, Pei Jiang Low, Brendan White, Rajibul Islam, and Crystal Senko. Limits on atomic qubit control from laser noise. *npj Q. Inf.*, 8(1):72, Jun 2022.

[201] M. F. Brandl, M. W. van Mourik, L. Postler, A. Nolf, K. Lakhmanskiy, R. R. Paiva, S. Möller, N. Daniilidis, H. Häffner, V. Kaushal, T. Ruster, C. Warschburger, H. Kaufmann, U. G. Poschinger, F. Schmidt-Kaler, P. Schindler, T. Monz, and R. Blatt. Cryogenic setup for trapped ion quantum computing. *Rev. of Sci. Inst.*, 87(11), 11 2016. 113103.

[202] M. Ramm. *Quantum correlations and energy transport in trapped ions*. PhD thesis, UCLA Berkeley, 2014.

[203] B. Merkel, K. Thirumalai, J. E. Tarlton, V. M. Schäfer, C. J. Ballance, T. P. Harty, and D. M. Lucas. Magnetic field stabilization system for atomic physics experiments. *Rev. of Sci. Instr.*, 90(4), 04 2019. 044702.

[204] R. Zhang, Y. D. Ding, Y. C. Yang, Z. Y. Zheng, J. B. Chen, X. Peng, T. Wu, and H. Guo. Active magnetic-field stabilization with atomic magnetometer. *Sensors*, 20(15), 2020.

[205] J. Franke. *Magnetic field noise cancellation for quantum simulation experiment with trapped ions*. PhD thesis, University of Innsbruck, 2021.

[206] H. Hu, Y. Xie, M. C. Zhang, Q. Q. Qin, J. Zhang, W. B Su, T. X Zhan, C. W Wu, P. X Chen, and W. Wu. Compensation of low-frequency noise induced by power line in trapped-ion system. working paper, May 2022.

[207] SRS function generator DS345. `https://www.thinksrs.com/`, 2023.

[208] Keysight e3631 Power supply. `https://keysight.com/`, 2023.

APPENDICES

Appendix A

Ablation Laser Sweeping

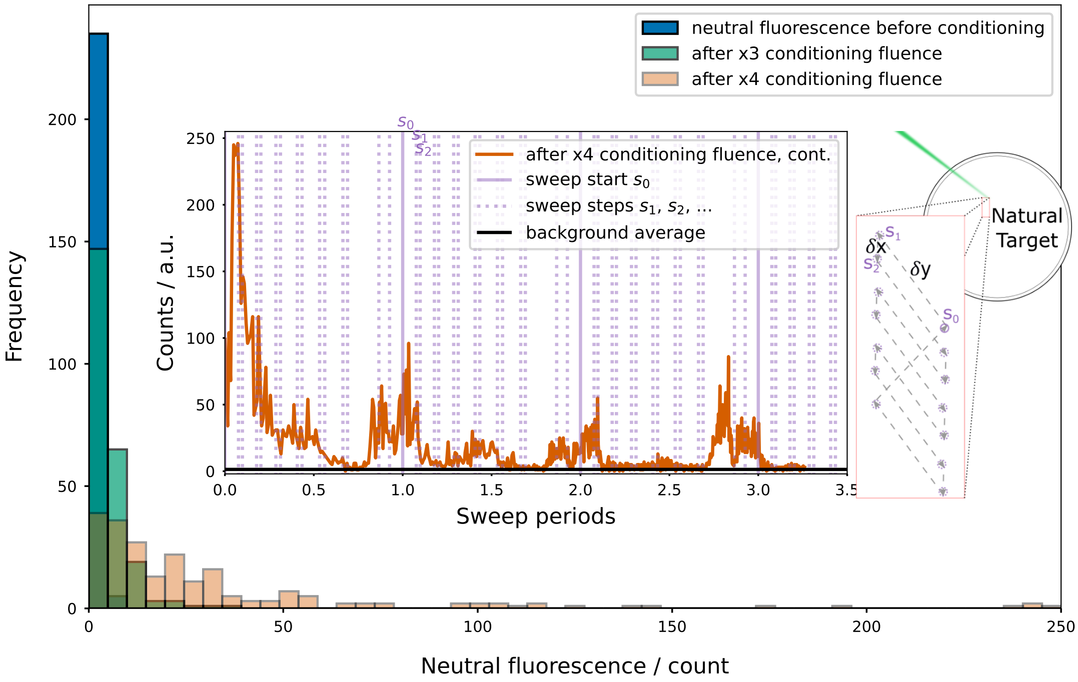

Figure A.1: Distribution of neutral fluorescence counts over a sweep area. As the area is conditioned, parts of the area generate more measured neutral fluorescence. The inset shows raw sweep data after the area is conditioned. The signal varies significantly from sweep to sweep.

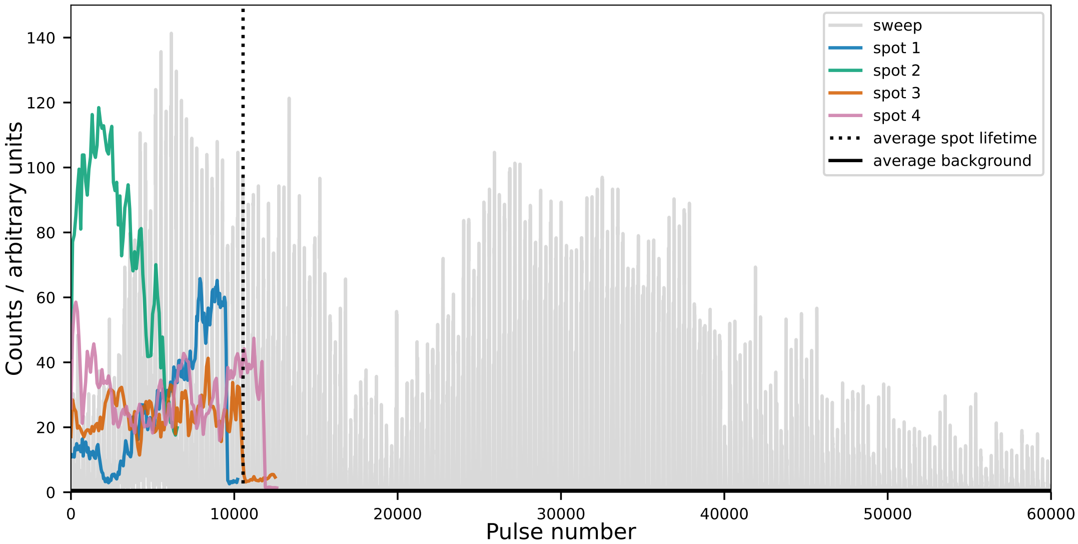

Figure A.2: Lifetimes of a sweep area as more ablation is done, with an average overall lifetime of a spot being $10,500$ pulses. Sweeping the laser across the target increases the amount of pulses before needing to move to $\sim 60,000$ pulses.

Using our servomotor-controlled mirror mount, the ablation laser can be swept across the target in predefined paths. Other groups [135, 139] have used this method to reduce the frequency of needing to find new spots. We initially planned on doing this as well, but in the end opted for using single spots. In the initial stages, we swept across the surface of the target to help characterize the spatial variation of neutral fluorescence signal. We swept the ablation laser across a trapezoidal region as shown in the insets of figure A.1, with a fluence of $0.17\,\mathrm{J/cm^2}$ and a repetition rate of $5\,\mathrm{Hz}$. The beam started at position s_0, and swept over an area of $200 \times 400\,\mu m$, returning to s_0 after $\sim 60\,\mathrm{s}$. We attempted to condition the whole area using conditioning fluences of $3 \times 0.17\,\mathrm{J/cm^2}$ and $4 \times 0.17\,\mathrm{J/cm^2}$.

Figure A.1's inset graph shows the neutral fluorescence of the conditioned area as we sweep through it four times. Within one period, the neutral fluorescence has a huge variation. This could be due to surface geometry - the surface profile could be directed away from the trap center in one part of the sweep, and well- directed in another. Temporal variation is also apparent, with the counts changing as much as 100% between periods. This is because as we sweep, each ablation pulse is not likely to hit the exact same spot as the previous period.

As shown in Figure A.2, the overall lifetime of such a sweep is on the order of $\sim 60,000$

pulses, compared to $\sim 10,000$ for single spots. While this means we might be able to use sweeps to reduce the amount of time needed for finding new spots, we found that the trade-off in loading rate is not worth it. Using single spots is more consistent for collecting ablation data, and for trapping ions.

Appendix B

Trap Depth Estimation

A rough estimate for the trap depth of our four-rod Paul trap is made using observations from loading experiments. In our experiment, the first type of ablation loading we did was direct-ion trapping (see Reference [121]). We observed that ions begin to be trapped after the trap RF is switched on at 27 µs after the ablation pulse hits the target. But the trap RF doesn't turn on immediately. We have measured our trap and resonator's Q-factor to be $Q = 350$, with an rf frequency of $\sim 20\,\mathrm{MHz}$. Therefore, the frequency width of the signal is $\sim 60\,\mathrm{kHz}$, which we can use to to estimate the turn-on time to be $\sim 17\,\mu\mathrm{s}$.

So overall, the ablation laser hits the target and ablates, and the generated ions are trapped $\sim 44\,\mu\mathrm{s}$ later. Given the $d = 14.6\,\mathrm{mm}$ distance from the ablation target to the trap center, the first ions to be trapped in direct-ion loading have a velocity of $v < 330\,\mathrm{m\,s^{-1}}$. Because these are the first ions to be trapped, they have the highest energy of any ions trapped using this method. Therefore, we can assume that the energy of these ions, 0.08 eV, is the depth of our potential-well. Next, we can use this trap depth and other parameters to estimate what our loading rate should be and compare it to what we measure.

Appendix C

Ablation Loading Rate

C.1 Loading rate estimation

We use the MB distribution, Equation 3.4, with the fitting parameters from our measured velocity distribution ($T = 37,000$ K and amplitude constant $A = 1.47 \times 10^{-8}$, see Figure 3.13(d)). The estimated percentage of ablated neutral atoms with energy below this trap depth is

$$\frac{\int_0^{330} f(v')dv'}{\int_0^{\infty} f(v')dv'} \approx 1\%, \tag{C.1}$$

From the TOF spectrum data, the peak of ^{138}Ba neutral fluorescence counts occurs at a 554 nm frequency of 541.433 055 THz, with velocity $v \approx 2,600 \mathrm{m\,s^{-1}}$ (see Figure 3.13), with around $C = 7$ counts total. Neutral atoms can only scatter while passing through the first-step photoionization beam, which has a waist of $w \approx 30\,\mu\mathrm{m}$. Our imaging system collects around $p = 2\%$ of scattered light, and the scattering rate of the transition is $f \approx 50\,\mathrm{MHz}$ (assuming around 40% excited-state population).

Using these figures, we can estimate the number of photons collected per neutral atom that can be imaged as

$$p \times w \times f \div v = 0.02 \times 30\,\mu\mathrm{m} \times 50\,\mathrm{MHz} \times \frac{1}{2.6\,\mathrm{km\,s^{-1}}} \approx \frac{0.012\,\text{photons}}{\text{atom}}. \tag{C.2}$$

We estimate the percentage of neutral atoms in the MB distribution which have a velocity near the peak velocity to be

$$\frac{\int_{2,250}^{2,650} f(v')dv'}{\int_0^{\infty} f(v')dv'} \approx 12\%. \tag{C.3}$$

Using the observed PMT counts $C = 7$ for the peak-velocity $v \approx 2,600 \mathrm{m\,s^{-1}}$ atoms, we can estimate the total number of these atoms being observed as

$$N = \frac{\text{atoms}}{0.012\,\text{photon}} \times C \div 0.12 \approx 5,000\,\frac{\text{atoms}}{pulse}. \tag{C.4}$$

The last step is to take into account how many of these observed atoms are actually trappable. First, only those passing through the 554 nm laser which also pass through the 405 nm beam will be ionized and trapped (see Figure 3.8); we estimate that within the field of view of the imaging system, 10% of the 554 nm beam path overlaps with the 405 nm beam. From Equation C.1, around 1% of atoms have low enough energy to be trapped. Ultimately, the number of trappable atoms per ablation pulse is estimated to be

$$N \times 0.1 \times 0.01 \approx 5. \tag{C.5}$$

This estimation is quite close to the near unity loading rate we observed in Section 3.2.2.

C.2 Loading rate correlation with neutral fluorescence

Date	**Fluence** (J/cm^2)	**Power** (μW)	**Time** (μs)	**Fluor.**	**Est. Fluor.**	**Load. Rate**
11/26/2020	75	9	145	40	20	0.25
	75	90	145	40	40	0.31
12/09/2020	49	80	145	100	50	0.09
	60	80	145	100	50	0.31
	60	80	145	500	25	0.07*
12/14/2020	60	8	145	100	25	0.25
02/17/2021	65	10	145	25	7.5	0.07[†]
02/18/2021	65	10	145	25	7.5	0.05
03/03/2021	140	80	160	100	100	1.0°
03/04/2021	100	8	160	5-20	12	0.08
	140	80	160	120-240	170	1.0
	140	8	160	60-100	80	0.6

Table C.1: Neutral fluorescence measurements and loading rates at different times and using different spots on the target. The time column refers to the start of the fluorescence integration window (ablation pulse is at 142.5 µs). Fluorescence is measured in counts per 55 µs time window. Loading rate is the number of ions trapped per pulse. Estimated fluorescence is an estimation of what each of the neutral fluorescence measurements would be if taken with ~ 10 µW, and with a window time of 160 µs. *This experiment was a sweep over an area, with counts of around 500 for only 10% of the sweep. [†]Newly calibrated wavemeter. °Dual pass filter added, giving us the ability to measure neutral fluorescence while trapping.

We used neutral fluorescence of ablated atoms as our measure to investigate the ablation process and to characterize the atomic plume. This measure can also be used as an estimate for the loading rate, as shown in Figure 3.17 of the main text. This data is elaborated on in Table C.1, which shows the fluorescence counts and loading rate results from many different days and different spots on the target. After some time, we decided to move the neutral fluorescence PMT time-window start time to 160 µs to reduce the effect of Doppler shift. This also is more relevant to the loading rate, since only slower atoms can be trapped. For all of these data points, the total integration time is 55 µs. In order to compare the different experiments with different parameters, the neutral fluorescence must be scaled based on how the parameters typically change them. We found that reducing the ionization laser (554 nm) power from ~ 85 µW to ~ 8 µW decreased the neutral fluorescence signal by around half. In addition, we found that moving the PMT integration start time from 145 µs to 160 µs roughly reduced the signal by half as well. With these observations, we are able to scale all of the data points appropriately so that we can compare them on the same footing.

Figure 3.17 shows the loading rate vs estimated neutral fluorescence for all of the different experiments listed in Table C.1. With $R^2 = 0.83$, we see that the two variables are very well correlated. This allows us to use neutral fluorescence as an estimate for loading rate, without having to collect trapping statistics. We were initially using two interchangeable single band-pass filters, limiting us to measure either neutral fluorescence or ion fluorescence, not both at the same time. In light of this discovered correlation, we installed a dual-band pass filter, which allows us to measure neutral fluorescence from the ablation pulse and also to see the ion fluorescence after we've trapped an ion. With this setup, it is possible to dynamically monitor the expected loading rate by measuring the neutral fluorescence every time the ablation laser is pulsed.

C.3 Ablation loading rate vs 493 nm frequency

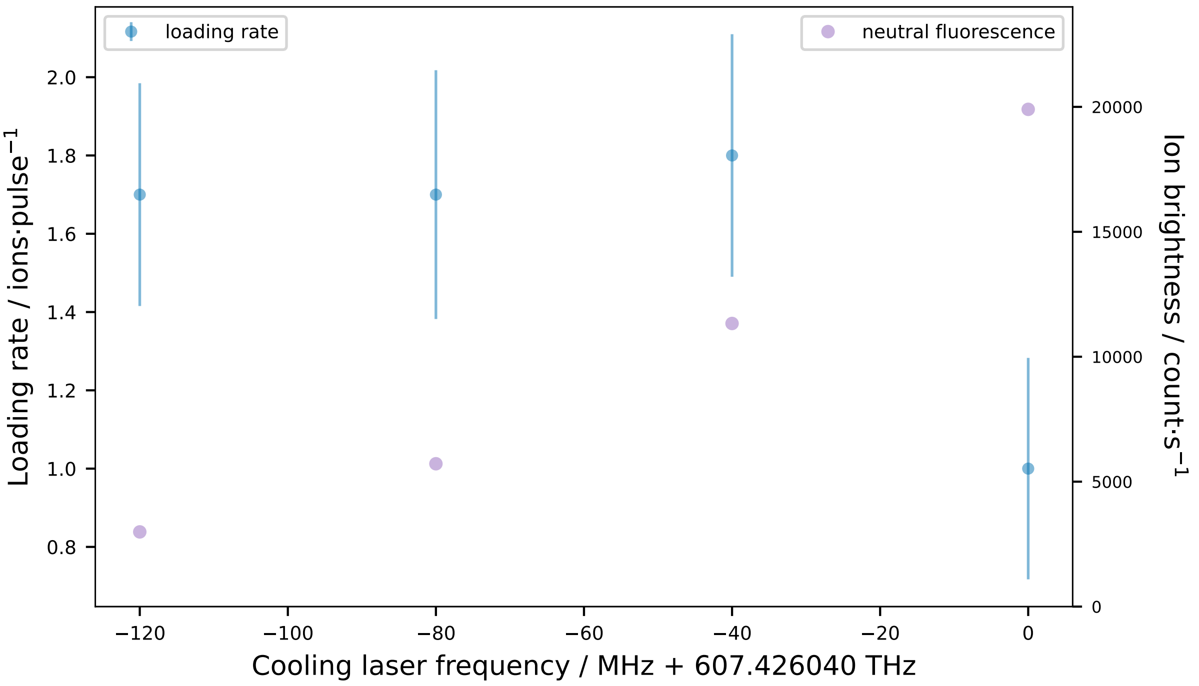

Figure C.1: Loading rate for different cooling laser frequencies detuned from resonance. The ion brightness for each frequency is also shown.

As shown in Figure C.1, loading ions is easier with a detuned cooling (493 nm) laser. However, with the laser on resonance, an already trapped ion fluoresces with near double counts than with 40 MHz detuning. This confirms that an already crystallized ion has a better cooling rate. The advantage of cooling-laser detuning in the loading rate can be seen when considering a completely unconfined ion passing through the trap center: these hot ions will experience a large Doppler shift, and will thus absorb red detuned light more than near-resonant light. Therefore, using a cooling laser which is red detuned can confine and cool ions that otherwise might have escaped the trap. In practice, we set our cooling laser to be 40 MHz red detuned from the optimal frequency.